Low Temperature Laboratory

Low dissipation thermometry using superconducting tunnel junctions

Timothé Faivre

Aalto University

DOCTORAL DISSERTATIONS

Aalto University publication series
DOCTORAL DISSERTATIONS 169/2015

Low dissipation thermometry using superconducting tunnel junctions

Timothé Faivre

Doctoral dissertation for the degree of Doctor of Science in Technology to be presented with due permission of the School of Science for public examination and debate in the lecture hall T2 C105 of Computer Science building (Konemiehentie 2, Espoo, Finland), on the 20th of November 2015 at 12 noon.

Aalto University
School of Science
Low Temperature Laboratory
PICO group

Supervising professor
Prof. Jukka P. Pekola

Thesis advisor
Prof. Jukka P. Pekola

Preliminary examiners
Prof. Floriana Lombardi, Chalmers University, Sweden
Dr. Detlef Beckmann, Karlsruhe Institute of Technology, Germany

Opponent
Dr. Valery. V. Ryazanov, Institute of Solid State Physics, Russian Academy of Sciences, Russia

Aalto University publication series
DOCTORAL DISSERTATIONS 169/2015

ISBN 978-952-60-6452-9 (printed)
ISBN 978-952-60-6453-6 (pdf)
ISSN-L 1799-4934
ISSN 1799-4934 (printed)
ISSN 1799-4942 (pdf)
http://urn.fi/URN:ISBN:978-952-60-6453-6

Images: Lexicographic analysis of the thesis content.

Unigrafia Oy
Helsinki 2015

Finland

Publication orders (printed book):
timothe.faivre@aalto.fi

NORDIC ECOLABEL
441 697
Printed matter

Aalto University

Abstract

Aalto University, P.O. Box 11000, FI-00076 Aalto www.aalto.fi

Author
Timothé Faivre

Name of the doctoral dissertation
Low dissipation thermometry using superconducting tunnel junctions

Publisher School of Science

Unit Department of Applied physics, Low Temperature Laboratory

Series Aalto University publication series DOCTORAL DISSERTATIONS 169/2015

Field of research Engineering Physics, Physics

Manuscript submitted 16 June 2015 **Date of the defence** 20 November 2015

Permission to publish granted (date) 18 August 2015 **Language** English

☐ **Monograph** ☒ **Article dissertation (summary + original articles)**

Abstract

Thermometers are a cornerstone of experimental physics, since the early days of thermodynamics in the seventeenth century. Nowadays, the state of the art thermometers are employed as sensors for instance in bolometers and calorimeters, probing the light originating from the Big Bang. The limitation of these devices in terms of the minimum detectable power or temperature changes is intrinsic: at millikelvin temperatures, their own temperature fluctuates as predicted by the Fluctuation-Dissipation Theorem.

In this thesis we investigate thermometers able to measure the temperature of an electron gas at sub-kelvin temperatures. We based our approach on tunnel junctions (I) between a superconductor (S) and either a normal metal (N) or a weaker superconductor (S'). In order to create a non-invasive thermometer, we mainly investigate how the low-bias impedance of SINIS and SIS'IS devices responds to temperature.

For SINIS structures, we observed a saturation of the temperature response due to the presence of leakage through the junction. Ballistic Andreev reflection is one of the sources of this leakage, and sets a minimum working temperature for these devices. In the special case where diffusive Andreev reflection determines the subgap conductance, we demonstrated that the low bias impedance is a sensitive probe down to the lowest temperatures measured.

In SIS'IS structures, we monitor the superconducting transition of the weaker of the two superconductors by measuring the current through the whole device. This kind of a device is similar to a Transition-Edge Sensor (TES), but the presence of tunnel junctions increases the responsivity and reduces the heat leak through the contacts.

For all these devices, we developed a model reproducing quantitatively the zero bias impedance response to temperature. This model allows one to compare and optimize the sensitivity of the thermometers, given as a Noise Equivalent Temperature (NET). NET as low as a few $\mu\mathrm{K}/\sqrt{\mathrm{Hz}}$ has been observed for SIS'IS devices, and SINIS devices demonstrated a NET which is within a factor of ten the same as its theoretical limit set by the temperature fluctuations.

Keywords thermometry, superconductivity, tunnel junctions

ISBN (printed) 978-952-60-6452-9 **ISBN (pdf)** 978-952-60-6453-6

ISSN-L 1799-4934 **ISSN (printed)** 1799-4934 **ISSN (pdf)** 1799-4942

Location of publisher Helsinki **Location of printing** Helsinki **Year** 2015

Pages 132 **urn** http://urn.fi/URN:ISBN:978-952-60-6453-6

Acknowledgments

We always find, therefore, in trying to make ever more precise measurements of temperature that in the end, the quantity itself becomes elusive. T.J. Quinn [1]

I wish to thanks my supervisor Pr. Jukka Pekola for his help and his support along these few years. More than an advisor, he was a source of inspiration and a great solver of experimental problems. I particularly esteem his global view, in between theoretical and experimental physics, allowing him to patiently answer all the questions a graduate student can have. His commitment to the PICO group and to his students was the leading force for me to go forward.

If the PICO group would be a boat and Jukka a captain, noting could be possible without his second, Dr. Matthias Meschke who take an active part of keeping the laboratory alive. Along the years Matthias become more than a colleague and I could not thank him enough for that. Spending time with *Haalea Kala* was always a pleasure, even in the cold and rainy Finnish summer between Helsinki and Hanko.

I think my comprehension of the physical phenomena I was studying increases tremendously when Dr. Dmitry Golubev enters the group. His uncountable answers help me greatly to write this thesis. I am still impressed how everything sounds easy when they are explained by Dima; *The art of simplicity is a puzzle of complexity.*– Douglas Horton.

I am in debt of Jukka, Matthias and Dima for commenting the manuscript of the thesis, correcting it and forcing me to continue to improve it versions after versions.

I am thankful for the support provided by the Low Temperature Lab-

oratory during all these years. I used quite a lot of parts which were fabricated in the mechanical workshop there. I also enjoyed being able to work within a state-of-the-art cleanroom and I would like to thanks all the men and women behind this huge white box. I found in Micronova a collection of scientist able to create, invent and imagine. I want to thank especially the people trying to merge knowledge and scientist from different fields of research around conferences, boardgames and sauna.

I will miss many moments spent with people from the PICO group. Some of the crew members already left, like Thomas Aref, Simone Gasparinetti, Massimo Borrelli, Vera Gramich, Tommy Holmqvist, Sergey Kafanov, Helena Knowles, Ville Maisi, Mikko Möttönen, Juha Muhonen, Hung Nguyen, Ilmo Räisänen, Paolo Solinas, Andrey Timofeev, Youngsoo Yoon. Some others just arrived: Shilpi Singh, Jorden Senior, Antti Jokiluoma, Jesse Muhojoki, Nicolas Paillet, Libin Wang; bringing new working forces to the regular crew member: Anna Feshchenko, Robab Najafi Jabdaraghi, Ivan Khaymovich, Jonne Koski, Elsa Mannila, Antti Moisio, Joonas Peltonen, Olli-Pentti Saira, Mathieu Taupin, Klaara Viisanen. Thank you, keep the boat steady and the sails full !

I owe a special thanks to my family and friends who support me during this stay in a foreign country so far in the North, and especially to Noémie for being at my side.

The work described in this thesis was carried out under the direction of Prof. J. P. Pekola, in the PICO group of the Low Temperature Laboratory, within the Department of Applied Physics of the Aalto University, from January 2011 to May 2015. I acknowledge the support the European Commission under Project No. 264034 (Q-NET Marie Curie Initial Training Network).

Paris, October 21, 2015,

Timothé Faivre

Contents

List of Publications

This thesis consists of an overview and of the following publications which are referred to in the text by their Roman numerals.

I D. Golubev, T. Faivre and J.P. Pekola. Heat transport through a Josephson junction. *Physical Review B* **87**, 094522, (2013).

II T. Faivre, D. Golubev and J.P. Pekola. Josephson junction based thermometer and its application in bolometry. *Journal of Applied Physics* **116**, 094302, (2014).

III T. Faivre, D. Golubev and J.P. Pekola. Andreev Current for low temperature thermometry. *Applied Physics Letters* **106**, 182602, (2015).

Author's Contribution

Publication I: "Heat transport through a Josephson junction"

The author suggested the topic of this work, then participated in the preparation of the manuscript by providing parameters for the model, which correspond to the realization of experiments. He also interpreted the obtained theoretical results from the practical point of view.

Publication II: "Josephson junction based thermometer and its application in bolometry"

The author fabricated the samples, performed the measurements, analysed the data and wrote the manuscript.

Publication III: "Andreev Current for low temperature thermometry"

The author fabricated the samples, performed the measurements, analysed the data and wrote the manuscript.

1. Introduction

Many fields of physics are already benefiting from low temperature detectors. As an example, they make possible the search for WIMPs (Weakly Interacting Massive Particles), which could possibly econtribute in the composition of dark matter [2]. The CRESST experiment, in Gran Sasso, aims to detect these particles using a scintillating crystal and two low temperature calorimeters attached to it. Another candidate in dark matter could be the massive neutrino. Here again, low temperature calorimeters are used in laboratory experiments like CUORE [3] or HOLMES [4] where such neutrinos are investigated trough the neutrinoless double beta decay ($0\nu\beta\beta$), of ^{130}Te for CUORE or ^{163}Ho for HOLMES.

In the field of nuclear physics, microcalorimeters have been used as high resolution spectrometers in Energy Dispersive X-ray Spectroscopy (EDS), now commercially available, with better energy resolution than the traditional semiconductor detectors [5]. In quantum communication, cryogenic Single Photon Detectors (SPD) have achieved photon number resolution [6]. In astronomy, low temperature detectors are widely use on earth (ALMA [7], SOFIA-GREAT [8], BICEP II [9], ect.) and in space (Hershel [10], Planck [11]), covering a wide frequency band from far infrared [12] to γ-ray range [13]. Cooling down a detector has the immediate benefit of reducing its noise and thus increasing the detector sensitivity compared to conventional detectors.

Several sensor technologies participated in the development of low temperatures detectors over the past decades [14, 15], and some of them have already found applications in other fields such as security screening [16].

Transition Edge Sensor (TES) is perhaps the most widely used thermal detector. A superconducting film is kept near its transition temper-

ature so that an incoming radiation will turn the sensor back to its normal state. By using Electro-Thermal Feedback (ETF), one can reduce the major drawbacks of a TES by both decreasing its response time and increasing its dynamic range [17]. In general, TES's are reaching record low noise in term of power (NEP below 10^{-20} $\mathrm{W}/\sqrt{\mathrm{Hz}}$ [18]) but they require a complex readout technology [19, 20] making large arrays of TES's complex to implement.

Superconducting nanowire Single Photon Detectors (SNSPD) are similar to TES's but the thin film is replaced by a wire (typically with a cross section of 20x100 nm) forming a meander [21]. When an incident photon hits the wire biased near its critical current, a hot spot is created turning a small section of the wire to its normal state. The full wire gets overheated quickly, increasing the voltage across the detector. Careful engineering allows one to design the wire so that a single photon is not enough to initiate a transition, but two photons are. This makes SNSPD interesting for measuring correlated event. The jitter time (the minimum time between two distinct measurable events) of such a detector is of the order of a few tens of ps [6].

To end the presentation of thermal detectors, one can say a few words about the hybrid NIS tunnel juntion, i.e. a junction between a normal metal N and a superconductor S, separated by an insulator I (see Chap. 3.2). NIS junctions have been proposed as a thermometer to monitor the temperature of the normal metal acting as an absorber [22]. The bolometers formed this way could possibly reach $\mathrm{NEP} \approx 10^{-19}$ $\mathrm{W}/\sqrt{\mathrm{Hz}}$ [23]. With a sensitivity comparable to TES's, but a low readout speed and some difficulty to multiplex due to their high impedances, NIS junctions are, however, less attractive than TES's for practical purposes.

The non-thermal detectors primarily use excess quasi-particle population in a superconductor as a probe. When radiation with energy larger than 2Δ hits a superconductor, it breaks one or several Cooper pairs and creates free quasiparticles above the gap. These quasiparticles are detected via a SIS tunnel junction (Single Tunnel Junction detector, STJ), via a change of resistance (Hot Electron Bolometer), or via the modification of the kinetic inductance of the superconductor (KID for Kinetic Inductance Detector).

Historically the STJ's was one of the first detectors able to resolve

multiple photons [6] when used as a pair breaking device. By nature of the excitation process, the incoming radiation must have an energy larger than 2Δ which is setting a low frequency detection bound around 100 GHz when using aluminium as a superconductor[24, 25]. Nevertheless terahertz cameras have shown good performance, demonstrating NEP of the order of 10^{-15}–10^{-16} $\mathrm{W}/\sqrt{\mathrm{Hz}}$ [26, 27], the first number being typical for an array of a few tens of pixels. STJ's can also be used as a SIS mixer to downconvert an incoming radiation (typically in the 10–200 GHz range) down to microwave frequencies (4–8 GHz) where the signal can be processed with traditional electronics [27]. In addition to their great bandwidth, these detectors have the advantage to be coherent, thus keeping information about the phase of the incoming radiation. Unfortunately SIS mixers are limited by their internal losses to frequencies lower than 4Δ [28].

Hot Electron Bolometer (HEB) is also making use of heterodyne detection to downconvert signals above 1 THz [29],i.e. at frequencies where SIS mixers do not work properly anymore. Such a detector employs a thin superconducting film, made either of a high T_C superconductor like NbN or $\mathrm{YBa_2Cu_3O_{7-\delta}}$ (YBCO) for the fast detectors or a low T_C superconductor like titanium to reach low NEP $\approx 10^{-19}$ $\mathrm{W}/\sqrt{\mathrm{Hz}}$ [30, 31]. A new generation of HEB's made out of graphene [32, 33] might compensate the speed of high T_C HEB with a sensitivity sufficient in space born applications in near future [34].

Research on KID's' has been growing fast[35] since the original publication in 2003 [36]. KID is using the change of the kinetic inductance with quasi-particle density as a probe [37]. This variable inductance can be either part of a lumped element resonator (LEKID [38]) or embedded into a microwave stripline (MKID [39]). Both can be intrinsically frequency multiplexed in large arrays [40], some of them reaching the photon limited regime [41] with NEP around 10^{-17} $\mathrm{W}/\sqrt{\mathrm{Hz}}$.

Finally, the Magnetic MicroCalorimeter (MMC) [42] is based on measuring the magnetic susceptibility to deduce the temperature of the absorber, which can be a paramagnetic alloy (like Au:$\mathrm{Er_{300ppm}}$) or a diamagnetic superconductor [43]. Compared to a resistive thermometer, reading out the susceptibility using a SQUID has two main advantages: the dissipation is smaller inside the absorber and there is no galvanic connection between the absorber and the thermometer. Well suited for X-rays (up to

98% of the incident beam can be absorbed), these detectors can reach a measured linewidth as small as a few eV ($\Delta E_{\mathrm{FWHM}} = 2$ eV at $E = 6$ keV [44], up to $E = 60$ keV). Furthermore, creating large MMC arrays is possible using the setup described in [45], where a single SQUID is reading out 4 different absorbers.

Of all the detectors described above, only TES's [46–50] and MMC's [51, 52] are reaching the thermodynamic limit, for which the sensitivity is limited by the fluctuation of the absorber's energy [1]. For TES's, an excess noise has been observed and explained using a complex thermal model [53, 54].

This thesis aims at summarizing our efforts to develop and optimize thermometers for nano-sized objects at low temperatures to study thermal fluctuations. Devices based on a tunnel junction made of aluminium were studied experimentally, and were optimized to decrease the influence of the thermometer on the system studied. These nano-devices are expected to exibit temperature fluctuations, and we aim to construct a thermometer able to detect these fluctuations. Studying these temperature fluctuation spectrum can give tools to reduces excess noise in current TES's .

The first chapter is describing the temperature and its possible fluctuations in a general way. A few words will be said about thermometers, bolometers and calorimeters, as they are the practical applications that can most probably benefit from this thesis.

The second chapter is summarizing different theoretical elements needed to interpret the experiments. The question of electrical and thermal transport through a tunnel junction will be at the heart of this chapter. We aim to provide a basic understanding of the phenomena, providing references that go further and beyond the approximations done for the purpose of simplification.

The third chapter discusses some practical topics, such as the device fabrication and the low temperature measurement apparatus. As we aim to measure fluctuations, we emphasize there the role of noise in a transport measurement set-up.

The fourth chapter is dedicated to the experiments and their results. We will start by setting the requirements for the thermometer to catch the

[1] This limit does not apply for STJ and SNSPD.

fluctuation spectrum. Then a few thermometers will be discussed, with the common feature that they are based on aluminium tunnel junctions. The conclusion of this chapter is merging the experimental results in a single figure, in which we compare the noise of the thermometers with the expected fluctuation spectrum.

The data presented in this thesis are mainly unpublished results (unless specified). The published works have been referenced in the text with roman numbers. In Publication I, the heat current across a Josephson junction is studied theoretically. A titanium island connected to two aluminium leads by Josephson junctions has been used as a thermometer in Publication II. Possible use of such a device as a bolometer is considered. In Publication III, titanium inside the island is replaced by a titanium-gold multilayer. A strong disorder-enhanced Andreev current was observed, which can be used as a sensitive thermometer at low temperatures.

2. Temperature and its fluctuations

2.1 Introduction

Temperature is a notion as old as humanity. The word temperature is from the Latin *temperare*, meaning *to be mixed*. The first temperature scale was indeed constructed by mixing ice and boiling water. An equal quantity of each substance mixed together leads to the definition of *neutral* temperature. By varying the ratio of boiling water and ice, four degrees above and below this neutral temperature defined the first known temperature scale, as described in the writings of Gallen (AD 130-200) [1]. A comprehensive review of the early age thermometers starting from the first air thermometers in the 17^{th} century can be found in the *history of the thermometer* by W.E. Knowles Middelton [55]. The human body itself can be considered as a thermometer as we have feelings of temperature, with the help of two kinds of thermosensors for cold $<36^{\circ}$C and hot $>36^{\circ}$C temperatures [56]. The body is self-regulating its own temperature around 37°C, but it is also experiencing some fluctuations, impacting the perception of the environmental temperature.

A common confusion exists between the temperature, *the degree or intensity of heat present in a substance or object* [...] and the heat, *seen as a form of energy arising from the random motion of the molecules of bodies* [...] [57] . Hence, the first part of this chapter defines the concept of temperature which we will use thoroughly in the following chapters. The temperature fluctuation spectrum of a system in quasi-equilibrium will be then studied. This spectrum appears usually as the ultimate sensitivity of a certain kind of a radiation sensor, which will be the topic of the last part of this chapter.

2.2 Thermodynamic temperature

A simple example to illustrate the concept of temperature is the ideal gas, formed by non-interacting mono-atomic particles in a box. Each single particle of mass m is fully defined given its position and momentum at any time t [Fig. 2.1 (a)]. If one considers a collection of N particles [Fig. 2.1 (b)] instead of a single atom, the number of variables needed to fully describe the system is $6N$. The equations become heavy to solve as N increases. Instead, the statistical physics allows one to deduce macroscopic properties of the system without knowing the position and momentum of each atom in detail. As an example, in Fig. 2.1 (c), one counts how many of the 10 000 helium atoms have the velocity v, given that the gas rests at room temperature and at atmospheric pressure (so-called standard condition). The histogram is compared with the Maxwell-Boltzmann distribution (solid line), describing the probability dp of finding an atom with a momentum in the interval $[\mathbf{v}, \mathbf{v} + \mathbf{dv}]$:

$$dp(\mathbf{v}) = \left(\frac{m}{2\pi k_\mathrm{B} T}\right)^{3/2} |\mathbf{v}|^2 \mathrm{e}^{-m|\mathbf{v}|^2/2k_\mathrm{B}T} \quad dv_\mathrm{x} dv_\mathrm{y} dv_\mathrm{z} \tag{2.1}$$

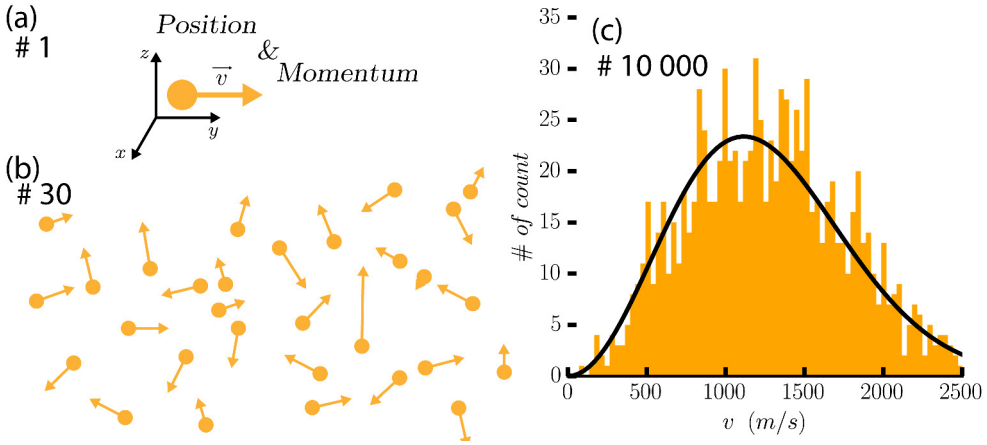

Figure 2.1. Statistical description of an ideal gas. (a) A single particle is fully described given its position and momentum. (b) Giving the positions and the momenta of a population of 30 particles with times, including all the collisions, becomes tedious. (c) The statistical approach, where a given population is described by a probability distribution, allows one to estimate some properties of the system. The plot is considering 10^4 molecules of ^{4}He under standard NTP conditions.

Some assumptions need to be done about the system to derive its statistical distribution. In the previous example, the gas has to be ideal and the velocity distribution to be isotropic to derive the Maxwell-Boltzmann distribution [58]. In the limit of a large number of particles, the histogram and the probability distribution agree perfectly. Nevertheless some deviations are visible in Fig. 2.1 (c), although the 10000 atoms considered in the

numerical estimation might be seen as a large number. Fortunately, the typical number of atoms in a cubic meter of gas is 2.7×10^{25} (≈ 45 mole), and the deviations in that case are almost impossible to observe. From Eq. (2.1), one can see that the Maxwell-Boltzmann distribution has a single argument T, the thermodynamic temperature of the gas, for a given atomic species of mass m. One can interpret the temperature as the measure of the random motion of the atoms with average speed $\langle v \rangle = 2\sqrt{\frac{2k_{\mathrm{B}}T}{\pi m}}$. Given that it is sufficient to fix the temperature in order to describe macroscopically the gas at equilibrium, one can use this gas as a thermometer by measuring its pressure [1]. The equilibrium distribution is ensured by the numerous collisions taking place in the gas. The next section will describe how a container of gas can reach equilibrium.

2.3 Thermal equilibrium

Temperature can also be defined as *a quantity which takes the same value in two systems that are brought into thermal contact with one another and allowed to come to thermal equilibrium* [1]. The time required for the two systems to reach an equilibrium depends on how fast the heat is transferred between them. Supposing that the temperature in each of the systems can be defined at all times, this heat transfer $\dot{Q}$ can be characterized by a thermal conductance G_{th} so that $\dot{Q} = G_{\mathrm{th}}\Delta T$. The time evolution of the temperature difference between the two systems ΔT is given, in the absence of fluctuations, by

$$\mathcal{C}\frac{d\Delta T}{dt} = -G_{\mathrm{th}}\Delta T \, . \tag{2.2}$$

The heat capacity $\mathcal{C}$ of the system describes how much heat δQ is needed to raise the temperature of the system by δT, i.e. $\mathcal{C} \equiv \delta Q/\delta T$. From Eq. (2.2), one finds $\Delta T = \Delta T(0)\mathrm{e}^{-t/\tau}$, where we have defined the relaxation time $\tau = \mathcal{C}/G_{\mathrm{th}}$. On a time scale long compared to this relaxation time, the system is found at equilibrium and both sides have the same temperature. This approach is based on the assumption that the temperature can be defined in each system at any time, which defines the quasi-equilibrium condition. It implies that the heat flow $\dot{Q}$ is slow enough to let the collisions bring the gas to a Maxwell-Boltzmann distribution in each sub-system. Hence, the collision time defines the shortest time scale in such a system.

2.4 Free electron gas model

The free electron gas model is the extension of the theory of the ideal gas to the electrons in a metal. In this model, the electrons are the equivalent of the non-interacting gas particles. At a high temperature, the Maxwell-Boltzmann distribution is still valid. The direct application of the kinetic theory of gases to the valence electrons in metals is known as the Drude model [59]. At low temperatures, the Maxwell-Boltzmann distribution has to be replaced by the Fermi-Dirac distribution to account for the Pauli exclusion principle [58]: to construct a state with N electrons, one has to fill N different one-electron levels [59]. At zero temperature, the lowest energy states are filled one by one until a certain energy, the Fermi energy E_{F}, is reached. The corresponding wavelength is denoted k_{F} (Fermi wavelength). The probability for a one-electron level k with the energy E_k to be occupied at the equilibrium temperature T is given by the Fermi-Dirac distribution

$$f(E_k) = \frac{1}{\mathrm{e}^{\frac{E_k-\mu}{k_{\mathrm{B}}T}}+1}\,, \tag{2.3}$$

where μ is the chemical potential: $\lim_{(\mathrm{T}\to 0)}\ \mu = E_{\mathrm{F}}$. The main properties of a metal can be obtained from this distribution with the help of the Sommerfeld expansion [59], which assumes that the electrons participating in the conduction are located near E_{F}. Some of these properties, like the heat capacity, will be discussed in Chapter 3.5. The conditions for a free electron gas to be at (quasi-)equilibrium are discussed in [60]. The collisions between electrons provide the main relaxation path. Experimentally, the quasi-equilibrium condition is valid on time-scales of the order of nanoseconds [61, 62]. The electron-electron Coulomb interaction can also be considered, and a theoretical treatment of this problem can be found in textbooks, see e.g. [63]. It leads to the definition of the *Laudau quasiparticles* which replace the electrons in the Drude model. The energy spectrum of these quasiparticles is depicted as a dashed line in Fig. 3.2.

2.5 Heat Equation

The system we will consider from now on follows the free electron gas model in quasi-equilibrium regime described above. This system is con-

nected to N reservoirs at temperatures T_n by the thermal conductances $G_{\mathrm{th},n}$. In most cases we can make the approximation that the system is only coupled to a single bath with few thermal conductances in parallel, i.e. $T_n = T_{\mathrm{bath}}$ for all n[1]. This situation is depicted in Fig. 2.2 (a). The bath temperature is not supposed to be constant, but can vary only slowly compared to the relaxation time of the system $\tau = \mathcal{C}/G_{\mathrm{th},\Sigma}$, where $G_{\mathrm{th},\Sigma}$ is the sum over all parallel heat conductances. $G_{\mathrm{th},\Sigma}$ is accounting for the heat conduction by phonons, photons, quasiparticles, etc. A constant external heat flow $\dot{Q}_0$ can be applied to the system, to describe the detection of an external radiation or to account for the electronic temperature saturation observed experimentally, like in Publication III. In addition, some random and instantaneous impulses of heat $\dot{Q}_i(t) = \Delta E_i\ \delta(t - t_i)$ can be injected to the system to mimic the detection of radiation quanta.

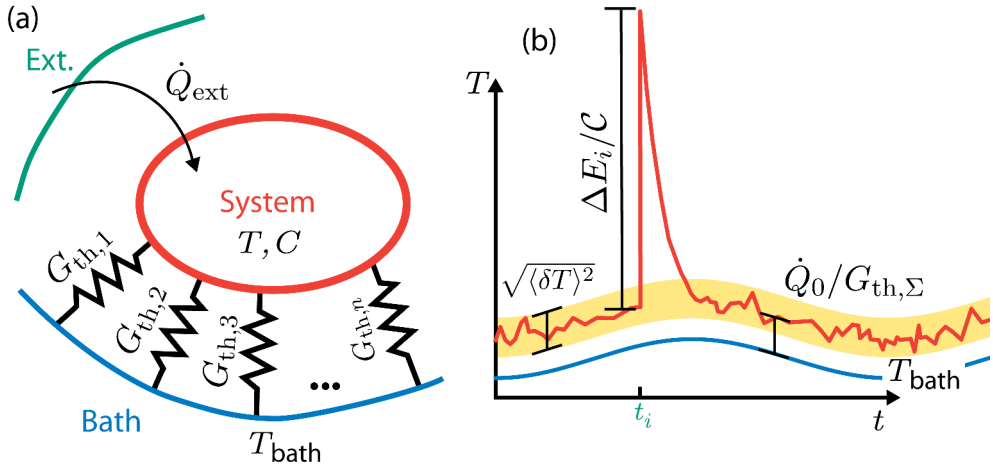

Figure 2.2. Heat equation model and its basic result. (a) System in quasi-equilibrium, connected to the bath by n thermal conductances $G_{\mathrm{th},n}$ in parallel. The system receives the heat $\dot{Q}_{\mathrm{ext}} = \dot{Q}_0 + \sum_i \Delta E_i \delta(t - t_i)$ from external sources. (b) Illustration of the typical temperature response of such a system. The temperature of the system deviates on the average from the bath temperature by an amount $\dot{Q}_0/G_{\mathrm{th},\Sigma}$. The peak, and the following exponential decay, are the temperature response to an incoming radiation of energy ΔE_i. The scatter in the system temperature is denoted $\delta T(t)$ in the text.

Within this model, the time evolution of the system temperature is given by the heat equation:

$$\mathcal{C}\frac{dT}{dt} = \dot{Q}_0 + \sum_i \dot{Q}_i(t) + G_{\mathrm{th},\Sigma}(T_{\mathrm{bath}} - T)\,. \tag{2.4}$$

Heat conductances entering into $G_{\mathrm{th},\Sigma}$ will be described in Chapter 3.4, and are functions of the temperature and some other external parameters. The linear approximation, only valid for small deviations around

[1]An example of $T_n \neq T_{\mathrm{bath}}$ is the temperature of the phonons when they are decoupled from the bath [64].

T_{bath}, allows us to ignore the temperature dependence of G_{th}. Under these approximations, Eq. (2.4) can be solved by means of Fourier transform, and the solution reads

$$T - T_{\mathrm{bath}} = \frac{\dot{Q}_0}{G_{\mathrm{th},\Sigma}} + \sum_i \frac{\Delta E_i}{\mathcal{C}} e^{-(t-t_i)/\tau} \theta(t - t_i) \,. \tag{2.5}$$

From Eq. (2.5) it can be seen that the system temperature T responds to energy quanta instantaneously and then relaxes exponentially back to the bath temperature with a time constant $\tau = \mathcal{C}/G_{\mathrm{th},\Sigma}$ [like in Fig. 2.2 (b)]. However, one needs to consider the fact that the quasiequilibrium condition is provided by the electron-electron collisions and thus the smallest time scale that can be considered is of the order of $\tau_{\mathrm{e-e}}$. In addition, this model must be refined to account for the noise created by the heat flowing through the thermal conductances $G_{\mathrm{th},n}$. This will be the subject of the next section.

2.6 Fluctuation spectrum

The Fluctuation-Dissipation Theorem *states a general relationship between the response of a given system to an external disturbance and the internal fluctuation of the system in the absence of the disturbance* [65]. Formally, this can be written as

$$\left\langle \delta\dot{Q}_n(t) \delta\dot{Q}_n(t') \right\rangle = 2 G_{\mathrm{th,n}} k_{\mathrm{B}} T^2 \, \delta(t - t') \tag{2.6}$$

for a delta-correlated Markovian noise [66]. The temperature of the system has to be modified accordingly to take into account these fluctuations: δT is the noise created by $\delta\dot{Q}$, the sum of the heat fluctuations over the thermal channels. δT is solution of a heat equation similar to Eq. (2.4) and using again the Fourier transform, one gets

$$\delta T(t) = \frac{1}{\mathcal{C}} \int_{-\infty}^{t} dt' \, \delta\dot{Q}(t') \, e^{-(t-t')/\tau} \tag{2.7}$$

from which one can derive the temperature fluctuation spectrum

$$S_T(\omega) \equiv \int dt \, \langle \delta T(t) \delta T(0) \rangle \, \mathrm{e}^{i\omega t} \tag{2.8}$$

$$= \frac{2 k_{\mathrm{B}} T^2}{G_{\mathrm{th},\Sigma}} \frac{1}{1 + (\omega\tau)^2} \,. \tag{2.9}$$

From the spectrum S_T, the mean square fluctuation can be calculated as

$$\left\langle \delta T^2 \right\rangle \equiv \int \frac{d\omega}{2\pi} S_T(\omega) = \frac{k_{\mathrm{B}} T^2}{\mathcal{C}} \,. \tag{2.10}$$

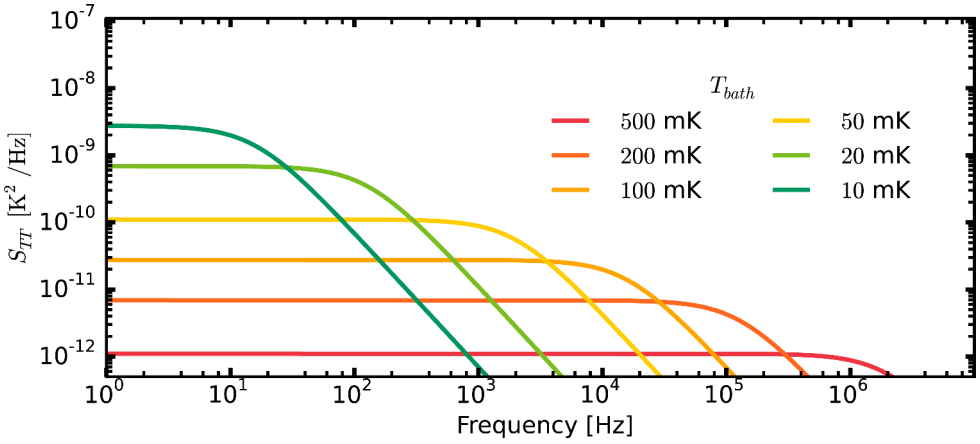

Figure 2.3. Temperature fluctuation spectrum S_T for a *typical* sample based on a copper normal island: $\mathcal{V} = 0.01\ \mu\text{m}^3$, $\Sigma = 2\ \text{nW}/\mu\text{m}^3/\text{K}^5$ and $\gamma_\text{T} = 100 \times 10^{-18}\ \text{J}/\mu\text{m}^3/\text{K}^2$.

There was a period when temperature fluctuations were discussed in popular literature [67, 68]. The fluctuation $\langle \delta T^2 \rangle$ of the temperature [Eq. (2.10)] has been derived for a system in quasi-equilibrium. Thus, temperature fluctuations do not exist in a large reservoir. Nevertheless systems in quasi-equilibrium are relatively common in mesoscopic physics where the small size of the considered objects, combined with the low temperatures, reduces drastically their heat capacity. Experimentally, the temperature fluctuations have a direct impact on the performance of bolometers and calorimeters by limiting their sensitivity [17, 46].

In order to give an estimate of the magnitude of the fluctuation, let us consider a copper island, coupled to a bath mainly by electron-phonon interaction. Anticipating results of the next chapter, we have $G_{\text{th},\Sigma} \approx 5\Sigma\mathcal{V}T^4$ and $\mathcal{C} = \gamma_\text{T}\mathcal{V}T$. $\mathcal{V}$ is the volume of the island, and Σ and γ_T are two material constants. The values of these constants are given in Table 3.1. Figure 2.3 displays the resulting temperature fluctuation spectrum S_T for a few different bath temperatures. Under the previous assumptions the relaxation time $\tau = \gamma_\text{T}/5\Sigma T^3$ is the electron-phonon characteristic time, where the volume of the island cancels out. Hence, both the minimum bandwidth needed to measure the full spectrum and the zero frequency limit of S_T depend strongly on the bath temperature, as can be seen in Fig. 2.3. At 100 mK, with the same parameters as in Fig. 2.3 ($\mathcal{V} = 0.01\ \mu\text{m}^3$, $\Sigma = 2\ \text{nW}/\mu\text{m}^3/\text{K}^5$ and $\gamma_\text{T} = 100 \times 10^{-18}\ \text{J}/\mu\text{m}^3/\text{K}^2$), the expected magnitude of the fluctuations is $\sqrt{\langle \delta T^2 \rangle} \approx 1.2\ \text{mK}$. In the same condition, one has $\sqrt{S_\text{T}(0)} \approx 5.25\,\mu\text{K}/\sqrt{\text{Hz}}$ and $\tau \approx 63\,\mu\text{s}$. Lowering the bath temperature both reduces the bandwidth and increases the zero frequency amplitude of the fluctuations, and thus simplifies the measurement of the tempera-

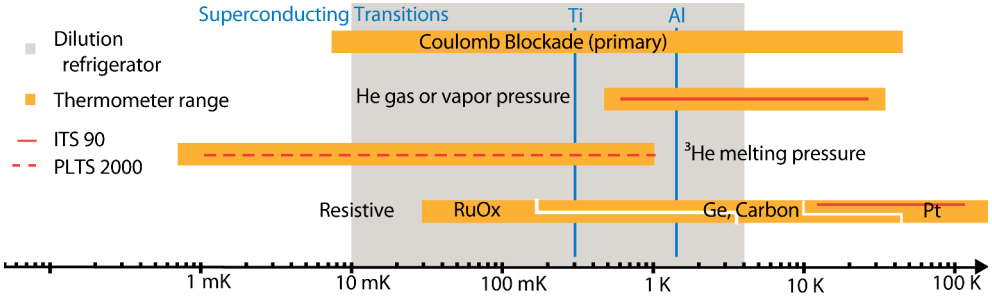

Figure 2.4. Low temperature thermometers and scales. The operating temperatures of some of the various thermometers described in [70] are depicted as orange bars. The shaded area represents the range of temperatures accessible by most common cryogenic refrigerators. The superconductors employed in this thesis have their transition temperatures denoted by blue lines. The defining methods of the official temperature scale (ITS90, PLTS2000) [71, 72] are plotted in red.

ture fluctuation spectrum.

2.7 Thermometers

Thermometers are a cornerstone of experimental physics, from the premises of thermodynamics to the latest observations of the universe [55, 69]. Usually one thermally anchors a thermometer to the object whose temperature needs to be known. In low temperature physics, attaching a thermometer to a system requires special care as the heat conductivities are usually small in the low temperature regime.

Figure 2.4 depicts some of the thermometers widely used in low temperature apparatus. For practical applications, mainly resistive thermometers are employed due to their ease of use. Unfortunately these thermometers are secondary, meaning that a calibration is required [1]. The same applies to any new kind of a thermometer, which has to be compared with a calibrated reference. For the thermometers discussed in this thesis, we usually compare the reading of the device under test to a calibrated Ruthenium Oxide (RuOx) thermometer [70]. Many quantities depend directly on this calibration, like the sensitivity. For this reason, we rely on the Coulomb Blockade Thermometer (CBT) [73, 74] to provide the absolute temperature reading needed to calibrate the RuOx thermometer. Both CBT and RuOx thermometers are covering the full temperature range achievable in our low temperature apparatus.

The sensitivity of a thermometer is usually given in terms of its Noise Equivalent Temperature, or NET, in $\mathrm{K}/\sqrt{\mathrm{Hz}}$. The NET is the noise of the

reading converted into temperature

$$\mathrm{NET} = \sqrt{S_T + \left(\frac{n_\mathrm{f}}{\partial V/\partial T}\right)^2} \tag{2.11}$$

where n_f is the voltage noise of the readout and $\partial V/\partial T$ the responsivity of the thermometer (Ch. 4.3). The temperature fluctuations S_T contribute directly to the NET, but are usually negligible compared to the readout noise $\mathrm{NET} \approx \mathrm{NET}_\mathrm{amp} = n_\mathrm{f}/(\partial V/\partial T)$. Chapter 2.8 presents some sensors based on low temperature thermometers where the fluctuation of temperature might be observed.

2.8 Bolometers and Calorimeters

A bolometer detects the average power radiation arriving at the detector, usually in the infrared range [12, 75, 76]. One realization of such a detector is based on an absorber, whose temperature is monitored, as depicted schematically in Fig 2.5. This absorber is well decoupled from the bath, thus any constant incoming radiation will elevate its temperature in a way that is detectable by a thermometer.

A calorimeter is formally a sensor of heat. In the context of radiation detectors, the concept of a microcalorimeter is usually associated with the detection of a single X-ray photon [30, 77]. The instantaneous response of the system temperature when a photon hits the absorber is monitored. Some systems, like the Transition Edge Sensor (TES), can be operated either as a bolometer or as a microcalorimeter [78]. One can summarize the situation by recalling Eq. (2.5) giving the response of an isolated system to an external heat load as

$$T = T_\mathrm{bath} + \overbrace{\frac{\dot{Q}_0}{G_{\mathrm{th},\Sigma}}}^{\text{Bolometric response}} + \sum_i \overbrace{\frac{\Delta E_i}{\mathcal{C}} e^{-(t-t_i)/\tau}\theta(t-t_i)}^{\text{Calorimetric response}} . \tag{2.12}$$

Temperature fluctuations are of prime interest for research on bolometers and calorimeters as they are fundamentally limiting their sensitivities [81]. As reducing the heat capacity of an absorber is increasing its calorimetric response ($\Delta T = \Delta E_i/C$), the calorimeters tend to have small heat capacity. Unfortunately, the amplitude of the temperature fluctuations is then increased, as $\langle \delta T^2 \rangle = k_\mathrm{B} T^2/\mathcal{C} \propto T$ for metals. The ultimate sensitivity of a calorimeter is usually given as an energy resolution $\delta E \equiv C\sqrt{\langle \delta T^2 \rangle}$.

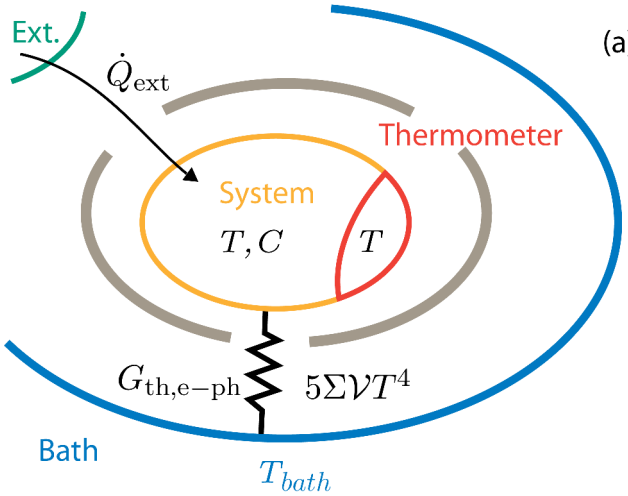

(a)

(b)

O Langley devised the bolometer:
It's really kind of thermometer
Which measures the heat
From a polar bear's feet
At a distance of half a kilometer.
Anon.

Figure 2.5. Bolometer. (a) Schematic. The absorber receives radiation $\dot{Q}_{\rm ext}$ from outside. The system, here an electron gas, is well isolated from the bath, so that the total heat conductance is dominated by the electron-phonon coupling. The temperature of the electron gas is measured by a thermometer attached to it, or directly probing it. (b) description of a bolometer, as found in [79]. S.P. Langley invented the bolometer in 1882 [80], and primarily used it to measure the infrared radiation emitted by the Sun.

In comparison, the sensitivity of a bolometer is usually given as Noise Equivalent Power (NEP). NEP corresponds to the heat flow generating a signal equal to the output noise of the detector. The temperature fluctuations are setting the optimal low frequency NEP one can achieve [82], $\mathrm{NEP} = \sqrt{2k_{\rm B}T^2G_{\rm th,\Sigma}}$. A bolometer performing in this regime is said to operate in the *thermodynamic limit*. It is indeed directly probing the temperature fluctuation spectrum [46, 49]. Such a bolometer, given a reasonable volume $\mathcal{V} \approx 0.1\mu\mathrm{m}^3$ would be also well performing in deep-sky observation [30], as one could expect $\mathrm{NEP} \approx 1 \times 10^{-21}\mathrm{W}/\sqrt{\mathrm{Hz}}$ at 20 mK. In comparison, a NEP in the range of $10^{-19} - 10^{-20}\mathrm{W}/\sqrt{\mathrm{Hz}}$ is required to observe the cosmological background [83].

A perfect radiation sensor would consist of a system in quasi-equilibrium for which the temperature can be measured without noise. Furthermore, this system should be well isolated from the bath so that the relaxation time is long enough to allow the measurement of the temperature. A small metallic island is approaching this description of a perfect bolometer / calorimeter for few reasons. First, the electrons inside a metallic conductor are typically in quasi-equilibrium. They can easily absorb heat and its total heat capacity is small at low temperatures ($C \propto T$). Second, the thermal conductivity is dominated by the electron-phonon coupling $G_{\text{th,e-ph}} = 5\Sigma\mathcal{V}T^4$ (see next chapter, Sec. 3.4.1), which is also vanishing at low temperatures. Such a detector, would detect any heat elevating the

temperature above the threshold given by the temperature fluctuations.

3. Theory introduction

In this chapter we provide the theoretical framework which will be used later on in order to explain our measurements. We will first derive the current-voltage I-V characteristics of a potential barrier between two normal metals, modeled by a δ-function, which is a good model for a normal metal - insulator - normal metal (NIN) tunnel junction. Next, after a brief general overview of superconductivity, we will generalize our model to a normal metal - insulator - superconducting (NIS) junction. Here we will follow the famous work by Blonder, Tinkham and Klapwijk (BTK) [84] from 1982. Then we will consider a tunnel junction between two different superconductors (S and S') and discuss the Josephson effect. The last part of this theoretical introduction will be dedicated to the heat related quantities, such as the heat conductance and the heat capacity of an electronic system. These important quantities are directly entering the temperature fluctuation spectrum we are interested in.

3.1 NIN tunnel junction

A tunnel junction between two conducting electrodes is basically a potential barrier which is high enough to forbid classical transfer of electrons over the barrier, but thin enough to permit their quantum tunneling under the barrier. The theory of electron tunneling has been developed in detail during the last 50 years. Unfortunately, presenting a full theory of this effect goes far beyond the scope of this thesis. Here we will only focus on the results relevant for the experiments with metallic junctions. The main distinction of a good metal is the short Fermi wave length of electrons, which allows one to consider them as wave packets behaving classically. In this regime, one can model almost any barrier by a δ-function

at the junction interface. The corresponding model is simple enough to be treated analytically.

Single channel transmission probability We consider two one dimensional (1D) quantum conductors separated by a tunnel barrier at $z = 0$. If the barrier is modeled by a δ-function $V(z) = \Phi\delta(z)$, the transmission probability $\mathcal{T}_k$ of a plain wave with wave vectors k and energy E_k can be found analytically as in [84, 85]

$$\mathcal{T}_k = 1/(1 + Z^2)\,, \tag{3.1}$$

where we defined the dimensionless parameter $Z = \sqrt{m}\Phi/\hbar\sqrt{2E_k}$ characterizing the barrier strength, with m the effective mass of an electron. For low transparencies and potentials varying at scales much longer than the Fermi wavelength, the transmission probability is generally a function of the energy and reads $\mathcal{T}_k = \exp\left(-\frac{1}{2\hbar}\int_{z_1}^{z_2} dz\sqrt{8m(V(z) - E_k)}\right)$ [86, 87].

Current through a NIN Tunnel junction The next step is to derive the total current trough an NIN tunnel junction. Forward and backward scattering in multiple channels has to be considered.

First we need to know the density of states for a given wave vector k available in the bulk material. The conduction electrons in metals have energies around Fermi energy E_F, and for small applied voltages one can assume that the density of states, ν_N, is constant [88]. Besides that, we need to know how many conducting channels contribute to the total current. This parameter is related to Sharvin resistance [89],also known as the focusing effect [90, 91], and can be estimated as $N_> = \pi\hbar\mathcal{A}\nu_\mathrm{N}v_\mathrm{F}a$, where $\mathcal{A}$ is the junction surface area, a a geometrical parameter and v_F is the Fermi velocity. Experimentally, the microscopic details of the barrier are usually unknown [92], and the effective transmission coefficient of the junction is estimated from its resistance R_T as

$$\mathcal{T} = \frac{R_\mathrm{K}}{R_\mathrm{T}N_>}\,, \tag{3.2}$$

where we introduced the quantum of resistance $R_\mathrm{K} = h/2e^2 \approx 12.9\,\mathrm{k\Omega}$. In general, the total current through a tunnel junction may be written in the form

$$I(V) = \frac{1}{2e}\int d\epsilon\, g(\epsilon)\left[f_\mathrm{L}(\epsilon, \mu_\mathrm{L}) - f_\mathrm{R}(\epsilon, \mu_\mathrm{R})\right]\,, \tag{3.3}$$

where $g(\epsilon)$ is the spectral conductance and $\epsilon = E - E_{\mathrm{F}}$ the energy measured with respect to E_{F}. For the particular case of a NIN junction, $g(\epsilon)$ does not depend on the energy ϵ and reads

$$g(\epsilon) = \frac{1}{R_{\mathrm{K}}} \sum_{\mathrm{n}=1}^{N_{>}} \mathcal{T}_n \equiv \frac{1}{R_{\mathrm{T}}} \,. \tag{3.4}$$

Equation (3.4) is known as Landauer-Büttiker formula for the conductance [93, 94]. The occupation probabilities of the electronic states in the leads are governed by the distribution functions $f_{\mathrm{L,R}}(\epsilon, \mu_{\mathrm{L,R}})$ [95–97]. At equilibrium, they are given by the Fermi-Dirac Distribution [88]

$$f_i(\epsilon, \mu_i) = \frac{1}{1 + \mathrm{e}^{\frac{\epsilon - \mu_i}{k_{\mathrm{B}} T_i}}} \,, \tag{3.5}$$

where T_i is the temperature of lead i and the chemical potential μ_i is measured with respect to E_{F}.

Only elastic scattering has been considered so far, i.e. we have assumed $|k| = |k'|$. One can also consider transitions between two states with different energies if one allows the exchange of energy with the environment [98, 99]. This has been discussed by Ingold and Nazarov in Ref. [100], who review the so-called $P(E)$ theory. The importance of this correction will arise while discussing the sub-gap conductance of an NIS tunnel junction.

3.2 NIS Tunnel junction

Before discussing NIS tunnel junction in detail, we briefly introduce the phenomenon of superconductivity.

3.2.1 Superconductivity

Superconductivity, in terms of disappearance of electrical resistance, was discovered by Kamerlingh Onnes in 1911 when the cryogenic temperatures became available by liquefying helium [101]. Later on, in 1914, a persistent current (called supercurrent) was demonstrated to flow indefinitely in a superconducting ring.

The first model describing the supercurrent and the repulsion of magnetic field associated with it has been developed by Fritz and Heinz London in 1935 [102]. Their phenomenological model has been able to describe most of the effects characteristic of superconductivity. However,

this model did not reveal the origin of superconductivity. For example, it could not explain why different metals have different transition temperatures. One had to wait until 1957 to get the answer to this question, until the first microscopic theory of superconductivity by Bardeen, Cooper and Schriffer (BCS) [103] was put forward.

To qualitatively understand the BCS theory, one has first to remember that at low temperatures electrons occupy the states with energies lower than E_{F}, forming what is called Fermi sea [88]. Cooper pointed out that the Fermi sea is unstable if electrons are attracted to each other, even weakly. Two electrons of opposite momentum and spin tend then to form a bound state – a *Cooper pair*. As a result, the density of states is depleted in the interval of energies $E_{\mathrm{F}} \pm \Delta$, where Δ is called the superconducting gap. The wave function a Cooper pair is complex and takes the form $\Psi \propto \Delta \mathrm{e}^{i\varphi_{\mathrm{S}}}$ where φ_{S} is the phase of the condensate. The BCS theory states that the attractive potential between electrons is mediated by phonons [104], and can be characterized by a coupling constant λ. The superconducting gap is then determined by the equation

$$\frac{1}{\lambda} = \int_{\Delta}^{\hbar\omega_{\mathrm{d}}} d\epsilon \frac{1}{\sqrt{\epsilon^2 - \Delta^2}} \tanh\left(\frac{\epsilon}{2k_{\mathrm{B}}T}\right), \tag{3.6}$$

where the Debye frequency ω_{d} provides a high energy cutoff and is related to the phonon density of states [88]. Solving Eq. (3.6), one finds that the superconducting gap is a function of temperature, and that it vanishes at the critical temperature T_{C}. The zero-temperature gap Δ_0 and the critical temperature are related through the interaction constant $\lambda \ll 1$:

$$\Delta_0 = \frac{\hbar\omega_{\mathrm{d}}}{\sinh(1/\lambda)} \approx \hbar\omega_{\mathrm{d}} \exp^{-1/\lambda} = 1.764\, k_{\mathrm{B}} T_{\mathrm{C}}\,. \tag{3.7}$$

The temperature dependence[1] of the gap, depicted in Fig. 3.1, is a universal function if scaled properly.

According to the BCS theory, no quasiparticle excitation can exist at energies in the range $E_{\mathrm{F}} \pm \Delta$. Above the gap, i.e. at $|E - E_{\mathrm{F}}| > \Delta$, four different quasiparticle states exist for a given energy E. The wave vectors of these states should be found from the equation $q_{\pm}^2 = k_{\mathrm{F}}^2 \pm \frac{2m}{\hbar}\sqrt{\epsilon^2 - \Delta^2}$ [106]. Excitations with wave vectors q_+ and $-q_+$ are electron-like quasiparticles, while excitations with wave vectors q_- and $-q_-$ are hole-like ones. Figure 3.2 (b) shows half of the spectrum of these quasi-particles,

[1] The following formula is used as an approximation of Eq. (3.6): $\Delta(T)/\Delta_0 = \tanh\left[1.1056\left(\tan[\frac{\pi}{2}(1 - T/T_{\mathrm{C}})^{0.55}]\right)^{0.5/0.55}\right]$ [105].

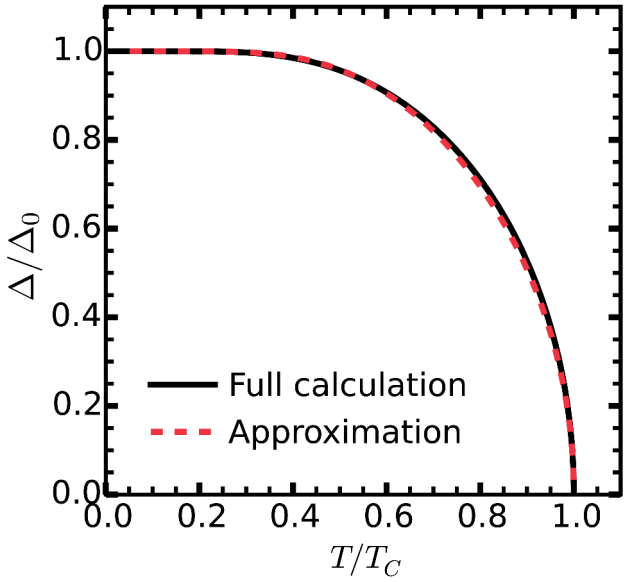

Figure 3.1. Calculated superconducting gap as a function of temperature using Eq. (3.6) and an approximate formula[1].

along with the spectrum of quasi-particles existing in a normal metal. The density of states of these excitations, scaled by normal state density of states ν_{N} is given by

$$n_{\mathrm{s}}^{\mathrm{BCS}}(\epsilon) = \frac{\theta(|\epsilon| - \Delta)\,|\epsilon|}{\sqrt{\epsilon^2 - \Delta^2}}\,. \tag{3.8}$$

This expression is plotted in Fig. 3.2 (a). For aluminium the normal state density of states is $\nu_{\mathrm{Al}} = 1.15 \times 10^{47}\,\mathrm{J}^{-1}\mathrm{m}^{-3}$ [88]. In the Table 3.1 we have summarized the densities of states and some other relevant parameters of a few materials typically used in experiments.

It is possible to estimate the number of excited quasiparticles per unit volume in a superconductor at a given temperature as follows

$$n_{\mathrm{qp}} = \nu_{\mathrm{N}} \int d\epsilon\, n^{BCS}(\epsilon) f(\epsilon)\,. \tag{3.9}$$

At low temperatures, the concentration of quasiparticles is exponentially suppressed, leading to the suppression of their contribution to the current. This is the topic of the next section.

3.2.2 Current through an NIS tunnel junction

The current through an NIS tunnel junction is again given by Eq. (3.3), but one has to modify spectral conductance $g(\epsilon)$ to account for the density of states in a superconductor, which is now given by Eq. (3.8) and

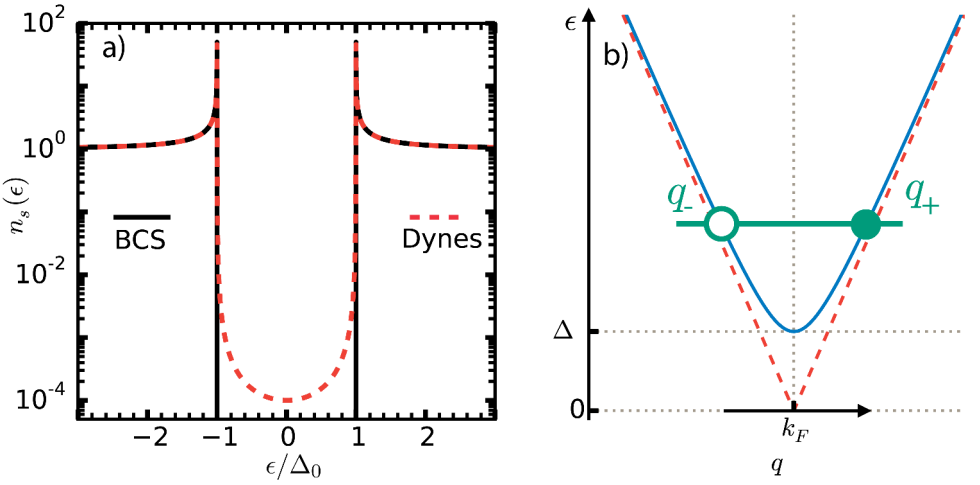

Figure 3.2. Quasiparticles in a superconductor. (a) BCS density of state, plotted along the Dynes density of states [Eq. (3.11)] with $\gamma = 1.\ 10^{-4}$. (b) Excitation spectrum. For a given energy ϵ, four possible solutions exist. Two of these states with the same direction of the wave vector are shown: an electron-like excitation above Fermi surface (solid circle) and a hole-like excitation (empty circle) with its group velocity opposite to direction of momentum $\mathbf{k}_F$. The dashed line shows the excitation spectrum in the normal state.

depicted in Fig. 3.2 (a). The starting point is to identify the possible processes involving a single quasiparticle coming from one side of the barrier, see Fig. 3.3.

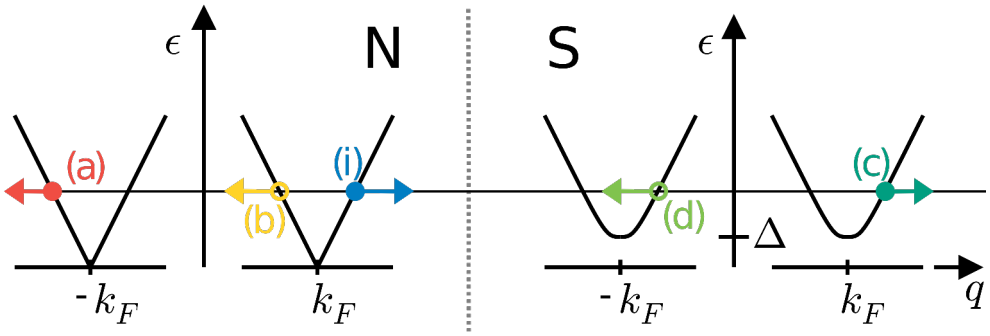

Figure 3.3. Schematic diagram of a NIS interface. An incident electron (i) in the normal metal is either normally reflected (a) or reflected as a hole as in Andreev reflection (b) generating a Cooper pair in the S side. When transmitted through the barrier, it can be either as a forward electron-like quasiparticle (c) or a backward hole-like quasiparticle (d).

Let us assume that a quasiparticle with energy ϵ and momentum k is coming from the left side of the barrier. After scattering it can end up in four possible states, which due to energy conservation lie on the horizontal black line drawn in Fig. 3.3, and these states are further restricted due to conservation of momentum. The corresponding four possible processes are

(a) the incident excitation can be normally reflected in the same way

as in an NIN junction;

(b) it can also be reflected as a hole back into the normal metal, creating a Cooper pair in the condensate, this process is called Andreev reflection;

(c) at $|\epsilon| > \Delta$ it can tunnel through the barrier and create an electron-like quasiparticle in the superconductor;

(d) at $|\epsilon| > \Delta$ it can also tunnel through the barrier and create a hole-like quasi-particle in the superconductor.

While calculating the probabilities associated with the processes (a), (c) and (d) is similar to what is done in the normal junction (see chapter 3.1), the process (b) is special because it is accompanied by the transfer of two electron charges through the barrier. This effect was first addressed by Andreev in Ref. [107]. It is responsible for finite conductance of the junction below the gap. The probabilities associated with all of the processes (a), (b), (c), and (d) have been derived in Ref. [84] by Blonder, Tinkham and Klapwijk. Their analysis is known as the BTK theory. The resulting spectral conductance reads

$$g^{\mathrm{BTK}}(\epsilon) = \frac{1}{R_{\mathrm{K}}} \sum_n \left[\frac{2\mathcal{T}_n\, \theta(|\epsilon| - \Delta)|\epsilon|}{\mathcal{T}_n|\epsilon| + (2 - \mathcal{T}_n)\sqrt{\epsilon^2 - \Delta^2}} + \frac{2\mathcal{T}_n^2\, \theta(\Delta - |\epsilon|)\Delta^2}{\mathcal{T}_n^2\epsilon^2 + (2 - \mathcal{T}_n)^2(\Delta^2 - \epsilon^2)} \right]. \tag{3.10}$$

One can easily verify that Eq. (3.3) with the spectral conductance g^{BTK} given by Eq. (3.10) is reduced to the Ohmic dependence $I = V/R_{\mathrm{T}}$ if one puts $\Delta = 0$. At small but finite values of the transmission coefficients $\mathcal{T}_n$, one finds that the sub-gap conductance ($eV < \Delta$) is a second order contribution due to Andreev tunneling. One can approximate the conductance by replacing the BCS density of states by the phenomenological Dynes expression [108]

$$n_{\mathrm{s}}^D(\epsilon) = \left| \Re\mathrm{e} \left(\frac{\epsilon/\Delta + i\gamma}{\sqrt{(\epsilon/\Delta + i\gamma)^2 - 1}} \right) \right| \tag{3.11}$$

where the parameter γ accounts for all sources of sub-gap conductance, including the environmentally assisted tunneling [109]. In this latter process, a photon is emitted or absorbed in the environment supplying the energy $\epsilon - \Delta$ needed to create or annihilate an excitation in the superconductor [100]. The phenomenological parameter γ is extracted from the zero bias conductance of the junction at low temperature, $G_0^{\mathrm{BTK}}(T \to 0) = \partial I/\partial V|_{\mathrm{v}=0} = \gamma/R_{\mathrm{T}}$. One can estimate the zero temperature value of

the zero bias conductance due to the regular Andreev tunneling from Eq. (3.10) as

$$\gamma = \frac{1}{N_>}\frac{R_\mathrm{K}}{R_\mathrm{T}}\,. \tag{3.12}$$

The only unknown parameter is the number of channels $N_>$ participating in tunneling. A simple estimate of the channel area $A_\mathrm{c}h$ for a square barrier made of aluminium oxide, is $A_\mathrm{ch} = \pi d\hbar\sqrt{2/mU}$[85, 110]. Choosing the barrier thickness $d \approx 1\,\mathrm{nm}$ and the barrier height with respect to the fermi energy $U = \Phi - E_\mathrm{F} \approx 1\,\mathrm{eV}$ as in [111], one gets $A_\mathrm{ch} \approx 2\,\mathrm{nm}^2$. The number of channels is then given by $N_> = \mathcal{A}/A_\mathrm{ch}$. The non-uniformity of the barrier usually leads to an order of magnitude larger channel area [92].

Calculated *I*-*V* characteristics are depicted in Fig. 3.4 for few electronic temperatures.

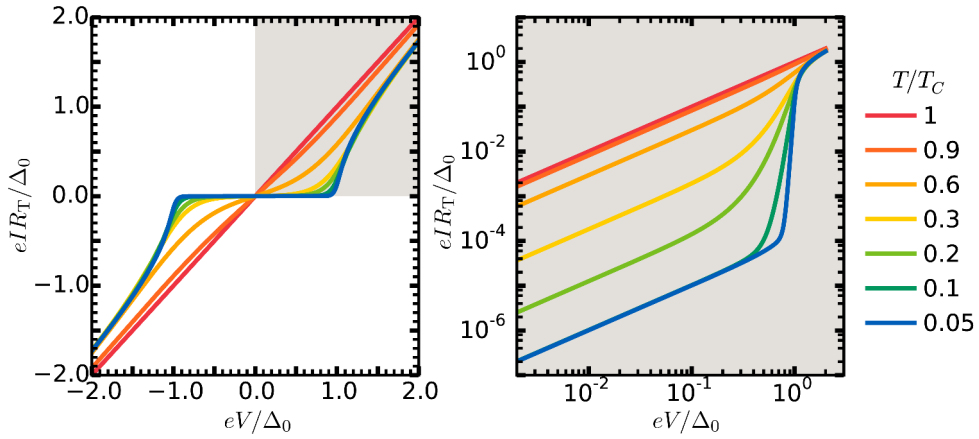

Figure 3.4. Calculated *I*-*V* characteristics at different temperatures. On the left, linear scale. On the right, logarithmic scale. Deep into the gap, the finite current is due to the leakage parameter $\gamma = 1.\ 10^{-4}$ entering the Dynes density of states [Eq. (3.11)].

Thus, the use of the γ parameter allows us to consider higher order processes in a phenomenological way. There is, however, an exception from this simple rule, namely, the disorder-enhanced Andreev reflection. It is important for relatively transparent junctions and at low temperature, where it results in a step on the *I*-*V* characteristic near zero bias voltage. In the next section we discuss this process.

3.2.3 Disorder-enhanced Andreev reflection

The disorder-enhanced Andreev reflection appears in the second order correction to the sub-gap current in powers of small channel trans-

mission probabilities $\mathcal{T}_n \ll 1$. Basically, it adds two extra contributions to the spectral conductance $g(\epsilon)$ due to the proximity and inverse proximity effect around the barrier. The proximity effect, i.e. the penetration of the superconducting properties into the normal side of the junction, leads to an extra current, forming a step on the *I-V* characteristic near zero bias voltage. The inverse proximity effect, associated with the reduction of the order parameter near the junction, introduces a finite density of states within the gap, leading to an extra current proportional to the applied voltage, similar to the one generated by the Dynes parameter.

The disorder-enhanced Andreev reflection has been first studied by Hekking and Nazarov in [112, 113] and it has been observed experimentally for transparent junctions [114]. The corresponding spectral conductance for $\mathcal{T}_n \ll 1$ reads (see e.g. [115])

$$g(\epsilon) = g^{\mathrm{BTK}} + \frac{\theta(\Delta - |\epsilon|)\Delta^2}{\Delta^2 - \epsilon^2} \frac{\Xi_{\mathrm{N}}\left[2\epsilon\right]}{2e^2\nu_{\mathrm{N}}R_{\mathrm{T}}^2} + \frac{\Delta^2}{\Delta^2 - \epsilon^2} \frac{\Xi_{\mathrm{S}}\left[2W(\epsilon)\right]}{2e^2\nu_{\mathrm{S}}R_{\mathrm{T}}^2}\,, \tag{3.13}$$

where $\nu_{\mathrm{N(S)}}$ is the density of state of N (or S), $W(\epsilon) = i\sqrt{\Delta^2 - \epsilon^2}$ for $|\epsilon| < \Delta$, $W(\epsilon) = \mathrm{sign}(\epsilon)\sqrt{\epsilon^2 - \Delta^2}$ for $|\epsilon| > \Delta$. Disorder-enhanced Andreev reflection appears in Eq. (3.13) via the combinations

$$\Xi_{\mathrm{N(S)}}[\epsilon] = \frac{1}{\mathcal{A}^2}\left(\int d^2r \int d^2r' \mathrm{Re}\left[\mathcal{C}^{r,r'}_{\mathrm{N(S)}}(\epsilon)\right]\right), \tag{3.14}$$

which are the double integrals over the junction area $\mathcal{A}$ of the Cooperon function $\mathcal{C}^{r,r'}_{\mathrm{N(S)}}$. The latter is the solution of the diffusion equation

$$\left(-i\omega + 1/\tau_{\varphi,\mathrm{N(S)}} - D_{\mathrm{N(S)}}\nabla^2\right)\, \mathcal{C}^{r,r'}_{\mathrm{N(S)}}(\omega) = \delta(r - r')\,. \tag{3.15}$$

Thus the Andreev current trough a junction is a function of the dephasing time $\tau_{\varphi,\mathrm{N(S)}}$, the diffusion constant $D_{\mathrm{N(S)}}$ and it also depends on the geometry of the sample.

If the effective Thouless energy of the device, $E_{\mathrm{Th}} \sim \hbar/\tau_{\varphi,\mathrm{N}} + \hbar D/\mathcal{A}$ [116, III], is small as compared to typical bias voltage and/or temperature, one can use simple approximations for the functions $\Xi_{\mathrm{N(S)}}[\epsilon]$. Namely, since $\Xi_{\mathrm{N}}[2\epsilon]$ quickly decays at high energies $|\epsilon| > E_{\mathrm{Th}}$, while $\Xi_{\mathrm{S}}[2W(\epsilon)]$ varies slowly at energies $|\epsilon| < \Delta$, one can approximate

$$\Xi_{\mathrm{N}}[2\epsilon] \approx \frac{4\pi}{\mathcal{A}\, t_{\mathrm{N}}}\delta(\epsilon) \quad , \quad \Xi_{\mathrm{S}}[2W(\epsilon)] \approx \frac{4}{\mathcal{A}\, t_{\mathrm{S}}}\frac{1}{\sqrt{\Delta^2 - \epsilon^2}}, \tag{3.16}$$

where $t_{\mathrm{N,S}}$ is the thickness of the corresponding film (see Fig. 3.5). The total current then includes two extra contributions due to the disorder-

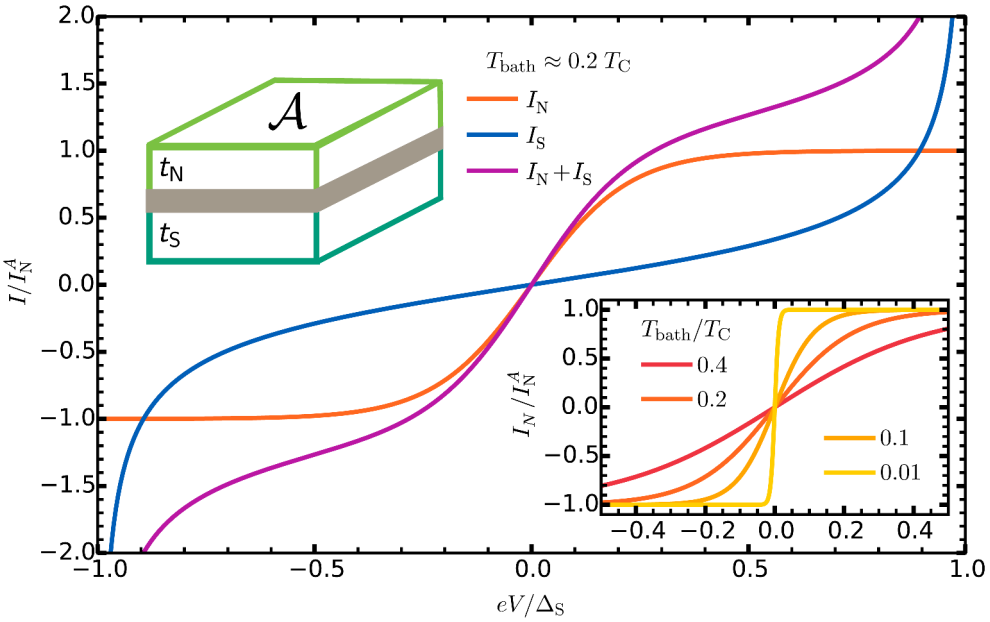

Figure 3.5. Andreev currents $I_{\rm N}$ and $I_{\rm S}$. The top inset depicts the model of large junctions of area $\mathcal{A}$, where $t_{\rm N,S}$ is the film thickness. In the main plot, depicting the sub-gap region of an *I-V* characteristic, the thickness has been chosen so that $\nu_{\rm N} t_{\rm N} = \nu_{\rm S} t_{\rm S}$. The bottom inset depicts $I_{\rm N}$ for few temperatures, showing the smearing of the step as the temperature is increased.

enhanced Andreev reflection and takes the form

$$I_{\rm tot} = I_{\rm BTK} + I_{\rm N} + I_{\rm S} \tag{3.17}$$

$$I_{\rm N}(V) = I_{\rm N}^A \tanh \frac{eV}{2k_{\rm B}T} \quad , \quad I_{\rm S}(V) = I_{\rm S}^A \frac{eV}{\sqrt{\Delta^2 - e^2V^2}}. \tag{3.18}$$

The currents $I_{\rm S}(V)$ and $I_{\rm N}(V)$ are displayed in Fig. 3.5. In the inset we have plotted $I_{\rm N}(V)$ for different electronic temperatures. On a phenomenological level one can include the contribution $I_{\rm S}(V)$ in an effective γ parameter together with the regular Andreev reflection and environment-assisted tunneling. The disorder-enhanced Andreev tunneling contribution to the phenomenological γ parameter is given by

$$\gamma_{\rm AS} = \frac{eI_{\rm S}^A R_{\rm T}}{\Delta} = \frac{1}{2\nu_{\rm S}\mathcal{A}t_{\rm S}\Delta}\frac{R_{\rm K}}{R_{\rm T}}. \tag{3.19}$$

In contrast the contribution $I_{\rm N}(V)$, originating from the proximity effect in the normal lead, has a singular shape at $eV, k_{\rm B}T \ll \Delta$. It forms a step in the *I-V* characteristic with the current changing from $-I_{\rm N}^A$ to $I_{\rm N}^A$ around zero voltage. The step is smeared by temperature. For large junctions of area $\mathcal{A}$, depicted in the top inset of Fig. 3.5, theory predicts the following values for the currents $I_{\rm N,S}^A$

$$I_{\rm N}^A = \frac{\pi\hbar}{e^3\nu_{\rm N}\mathcal{A}t_{\rm N}R_{\rm T}^2}, \qquad I_{\rm S}^A = \frac{\pi\hbar}{2e^3\nu_{\rm S}\mathcal{A}t_{\rm S}R_{\rm T}^2}. \tag{3.20}$$

Note that these current amplitudes are given only for a *large* junction. Other geometries have been also considered [113]. It leads only to changes in the current amplitudes $I^A_{\mathrm{N,S}}$ while the general shape of the dependences $I_{\mathrm{N,S}}(V)$ remains the same.

In conclusion, Eq. 3.3 provides a general expression describing the *I-V* characteristics of a NIS tunnel junction, including the higher order processes like Andreev reflection.

3.3 SIS' Tunnel junction

A SIS' tunnel junction is a junction between two superconductors with different gaps. By convention, S' is denoting the superconductor with the smaller gap. The total current flowing through a SIS' tunnel junction can be divided into two main parts [117] $I_{\mathrm{J}}(\varphi) + I^{\mathrm{SIS'}}_{\mathrm{qp}}(V)$. The first part arises from the Josephson coupling between both sides of the junction [118]. This current is a function of the phase difference $\varphi = \varphi_{\mathrm{S}} - \varphi_{\mathrm{S'}}$ between the two superconductors, and it can flow through the junction even if no voltage is applied. It will be discussed in the second half of this section. The second term $I^{\mathrm{SIS'}}_{\mathrm{qp}}(V)$ is the quasiparticle current and will be discussed in the next section.

3.3.1 Quasiparticle current

Quasiparticle transport in SIS' tunnel junctions has been studied extensively from the 60's [119, 120] until recently [121]. Such junctions might offer an alternative to NIS on-chip micro coolers [122–124], and improve their performance [125]. Making use of the same formalism as in chapter 3.2.2, we find the quasiparticle current in the form

$$I^{\mathrm{SIS'}}_{\mathrm{qp}}(V) = \frac{1}{eR_{\mathrm{T}}} \int d\epsilon \, n^D_{\mathrm{S}}(\epsilon) n^D_{\mathrm{S'}}(\epsilon + eV) \big[f_{\mathrm{S}}(\epsilon) - f_{\mathrm{S'}}(\epsilon + eV) \big]. \tag{3.21}$$

Eq. (3.21) is better understood with the help of Fig. 3.6 (a) - 3.6 (c), showing the densities of states of both superconductors when a voltage V is applied. The *I-V* characteristic of a SIS' tunnel junction [Fig. 3.6 (d)] has an extra peak at $eV = \Delta_{\mathrm{S}} - \Delta_{\mathrm{S'}}$, a new feature as compared to a NIS junction. It is due to the excitation above the gap in the superconductor with the smaller gap. Hence, this feature is quite sensitive to the temperature of S'.

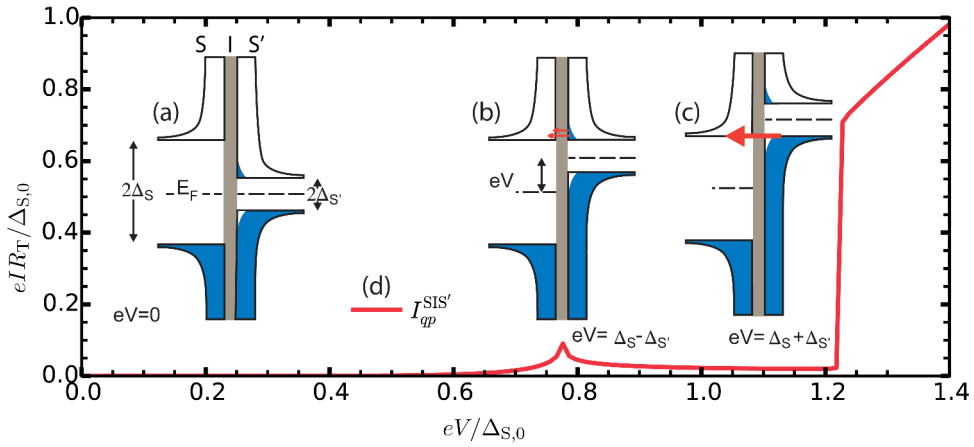

Figure 3.6. Quasiparticle transport in SIS' tunnel junction. (a)-(c) Densities of states, where the filling represents the thermal occupation at finite temperature. The chemical potential difference is set by the external applied voltage V. (b) *I-V* characteristic computed numerically using Eq. (3.21), where the smaller gap is set to $\Delta_{S',0} = \Delta_{S,0}/4$ and $T_{S'} = T_S = 0.66\ T_{C_{S'}}$. For this temperature, the smaller gap is slightly reduced $\Delta_{S'} = 0.95\ \Delta_{S',0}$, while the bigger one is not affected.

3.3.2 Josephson junction and the RCSJ model

Josephson considered a junction between two superconductors in 1962 [117]. He has predicted that a supercurrent

$$I_J = I_C \sin\varphi \tag{3.22}$$

should flow through the junction if a finite phase difference $\varphi = \varphi_S - \varphi_{S'}$ is applied between the two superconducting electrodes. Here I_C is the critical current, i.e. the maximum supercurrent the junction can support. Furthermore, Josephson has predicted that if a voltage V is applied to the junction, the phase difference φ should linearly grow in time

$$\frac{d\varphi}{dt} = \frac{2e\ V}{\hbar}. \tag{3.23}$$

Equations (3.22) and (3.23) are known as the Josephson relations. The critical current of a tunnel junction, I_C, is given by the integral [126–128]

$$I_C = \frac{1}{eR_T}\int_{\Delta_{S'}}^{\Delta_S} d\epsilon \frac{\Delta_{S'}\Delta_S\left[1-2f_{S'}(\epsilon)\right]}{\sqrt{\epsilon^2-\Delta_{S'}^2}\sqrt{\Delta_S^2-\epsilon^2}}. \tag{3.24}$$

Here we have again chosen $\Delta_{S'} < \Delta_S$, i.e. superconductor S' is supposed to be weaker than superconductor S. For a symmetric junction, $\Delta_{S'} = \Delta_S$, the integral reduces to a simple form $2eI_CR_T = \pi\Delta_S \tanh\left(\Delta_S/2k_BT\right)$. It is interesting to note that in this case near T_C the critical current vanishes at $T \to T_C$ as $I_C \sim \Delta_S^2 \propto T_C - T$. In general, i.e. for $\Delta_{S'} \neq \Delta_S$, the critical

current approaches zero with an infinite slope, $I_c \sim \Delta_{S'} \propto \sqrt{T_{C_{S'}} - T}$. Finally, it is useful to derive the zero temperature limit of Eq. (3.24),

$$I_{C,0} = \frac{\Delta_{S',0}}{eR_T} K_0 \left(\sqrt{1 - \left(\frac{\Delta_{S',0}}{\Delta_{S,0}} \right)^2} \right) , \tag{3.25}$$

where K is the modified Bessel function of the second kind.

To model a junction biased by a current $I_x > I_C$ and find out how the phase evolves in time, one needs to go beyond Eqs. (3.22) and (3.23). The most commonly used model for this regime is the Resistively and Capacitively Shunted Junction (RCSJ) model [129, 130]. The shunting capacitance C is usually determined by the geometry of the junction. It is finite because a parallel plate capacitor is formed by the two metals separated by the insulating layer. In order to ensure classical behavior of the phase in the wide range of parameters we also require $E_J \gg E_C$ where $E_C = e^2/2C$ is the charging energy and $E_J = \hbar I_C/2e$ is the Josephson energy. The shunt resistance R_S is a parallel combination of the environment resistance and the quasi-particle one, $R_{qp}(V)$ [131]. The equivalent circuit corresponding to RCSJ model is depicted in the inset of Fig. 3.7. In the regime of weak noise, the low frequency dynamics of the phase φ is determined by the Langevin equation

$$C\frac{\hbar\ddot{\varphi}}{2e} + \frac{1}{R_S}\frac{\hbar\dot{\varphi}}{2e} + I_C \sin\varphi = I_x + \xi_S. \tag{3.26}$$

It formally describes the motion of a particle with the coordinate φ in an effective tilted washboard potential

$$U(\varphi) = -E_J \cos\varphi - \hbar I_x \varphi/2e. \tag{3.27}$$

The noise ξ_S comes from the resistor R_S and possibly from other sources. At sufficiently high temperature it is defined by the correlator

$$\langle \xi_S(t)\xi_S(t') \rangle = \frac{2k_B T^*}{R_S}\delta(t - t'). \tag{3.28}$$

The noise temperature T^* may deviate from the base temperature of the experiment if an additional noise comes from outer circuit elements. At low temperatures $E_J \ll k_B T^*$ and low bias current $I_x < I_C$, $\dot{\varphi} = 0$ is solution of Eq. (3.26), leading to a supercurrent peak at $V = 0$. In the limit of small McCumber parameter, $\beta_c = 2eI_C R_S C/\hbar \ll 1$, one can set $C = 0$ in Eq. (3.26), which then becomes exactly solvable [132]. The junction is then said to be in the overdamped regime, and this limit is relevant for our experiments since in the interesting range of temperature, namely

near the transition temperature of the weaker of the two superconductors, the critical current is small. For the case of large McCumber parameter (underdamped regime), Eq. (3.26) has been numerically studied by Kautz and Martinis [131]. They have solved it using a Monte-Carlo algorithm, and specifically focused on switching between the phase diffusion –a supercurrent branch with a finite slope– and quasiparticle branches of the *I-V* characteristic. The Phase diffusion regime is achieved by considering high temperatures $E_{\mathrm{J}} \approx k_{\mathrm{B}}T^{*}$ and high damping. Due to the current noise caused by the finite temperature T^{*}, the phase escapes and retrappes from the washboard potential wells, leading to a finite voltage appearing across the junction. Hence, the reduced temperature $k_{\mathrm{B}}T^{*}/E_{\mathrm{J}}$ and the damping due to R_{s} are controlling the transition between the supercurrent regime ($V = 0$) and the phase diffusion regime ($V \neq 0$) at finite bias $I_{\mathrm{x}} < I_{\mathrm{C}}$.

If $C = 0$, the time averaged current through the junction at high bias $\hbar(I_{\mathrm{x}} - I_{\mathrm{C}})/e \gg k_{\mathrm{B}}T^{*}$ may be expressed in the form [118]

$$\langle I \rangle = \int_{-\pi}^{\pi} d\varphi \sigma(\varphi) \left[I_{\mathrm{qp}}^{\mathrm{SIS'}}(I_{\mathrm{x}}R_{\mathrm{S}} - I_{\mathrm{C}}R_{\mathrm{S}} \sin\varphi) + I_{\mathrm{C}} \sin\varphi \right] . \tag{3.29}$$

Here we have introduced the probability distribution function of the phase in the stationary limit, $\sigma(\varphi)$, given by

$$\sigma(\varphi) = \frac{\hbar\langle V \rangle}{4\pi e R_{\mathrm{S}} k_{\mathrm{B}} T^{*}} \int_{\varphi}^{\infty} d\varphi' \mathrm{e}^{\hbar I_{\mathrm{x}}(\varphi - \varphi')/2ek_{\mathrm{B}}T^{*}} \times \mathrm{e}^{(\cos\varphi - \cos\varphi')E_{\mathrm{J}}/k_{\mathrm{B}}T^{*}} . \tag{3.30}$$

$\sigma(\varphi)$ is normalized as $\int_{-\pi}^{\pi} d\varphi \sigma(\varphi) = 1$. The effect of phase fluctuations appears as a smearing of the *I-V* characteristics of the junction over a voltage interval of the order of $k_{\mathrm{B}}T^{*}/e$, as can be seen in Fig. 3.7.

From Eq. (3.29) one can derive zero bias resistance of the junction, which reads

$$R_0(T) = \left(\frac{\partial\langle V \rangle}{\partial\langle I \rangle} \right)_{\mathrm{I_x}=0} = \frac{R_{\mathrm{qp}}(T)}{I_0^2 \left(\frac{\hbar I_{\mathrm{C}}(T)}{2ek_{\mathrm{B}}T} \right)} . \tag{3.31}$$

Here we replaced R_{S} by R_{qp}, accounting for a current biased junction. I_0 is the modified Bessel function of the first kind and its argument can be rewritten as $E_{\mathrm{J}}/k_{\mathrm{B}}T$. As $E_{\mathrm{J}}/E_{\mathrm{J},0}$ is an universal function of $T/T_{\mathrm{C_{S'}}}$, the zero bias resistance has different temperature behavior depending on the ratio $E_{\mathrm{J},0}/k_{\mathrm{B}}T_{\mathrm{C_{S'}}} \approx 1.74\, K_0\left(\sqrt{1 - T_{\mathrm{C_{S'}}}^2/T_{\mathrm{C_S}}^2}\right) R_{\mathrm{K}}/R_{\mathrm{T}}$, as can be seen in Fig. 3.8. The special case $E_{\mathrm{J},0} = 0$, in red, corresponds to the quasi-particle

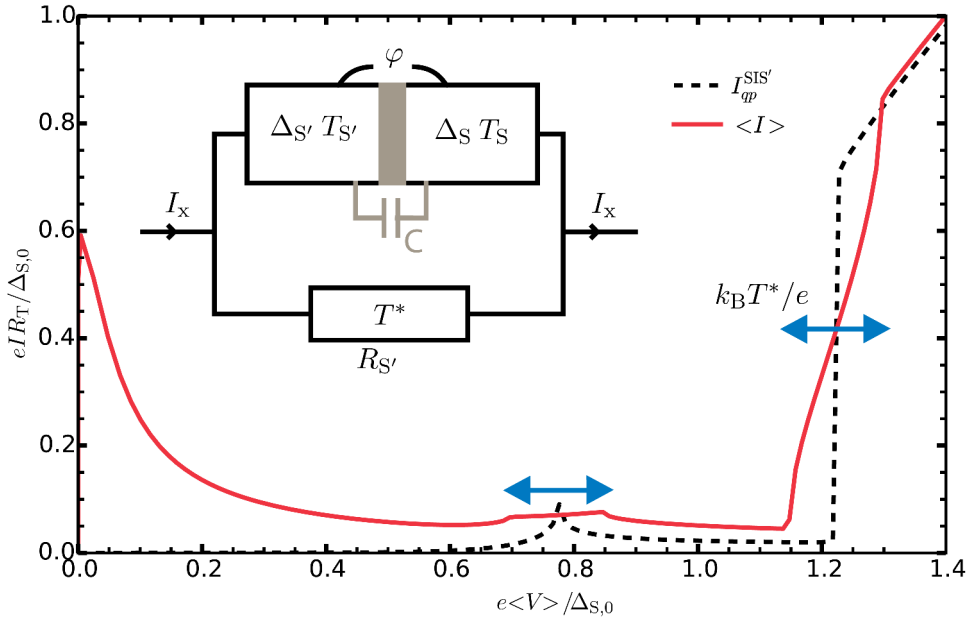

Figure 3.7. Effect of the phase fluctuations on the *I-V* characteristics. The parameters are the same as for Fig. 3.6 but a biasing resistor $R_S = 100\ \Omega$ is added to model the environment. *inset* : RCSJ circuit model.

resistance computed from Eq. (3.21). Once $\Delta_{S',0}$ is fixed, two different regimes can occur depending of the value of the normal state resistance R_T. If R_T is small and $E_{J,0} \gg k_B T_{C_{S'}}$, the critical current is rising as soon as $T < T_{C_{S'}}$, and zero bias resistance of the junction quickly drops to zero. The device based on such a junction behaves as a Transition Edge Sensor (TES) since its zero bias resistance monitors the superconducting transition of the weaker superconductor. Alternatively, if R_T is large and $E_{J,0} \lesssim k_B T_{C_{S'}}$, the supercurrent is smeared by the noise and the associated thermal fluctuations of the phase. Zero bias resistance of the junction is then smoothly varying with temperature. The drop in the resistance happens much below $T_{C_{S'}}$, at a temperature $T_0 \approx E_{J,0}/k_B$. At very large R_T one can reach the limit $2E_{J,0} < \Delta_{S,0}$, in which case the resistance never vanishes, instead it continues to grow even at very low temperatures if Dynes parameter γ is vanishing. $R_0(T)$ for various parameters is shown in Fig. 3.8.

3.4 Heat Conductance

So far we have discussed how charges are transported through a barrier, covering the NIN, NIS and SIS' cases. Charge transport is associated with energy current. Current flowing through a resistor results in Joule

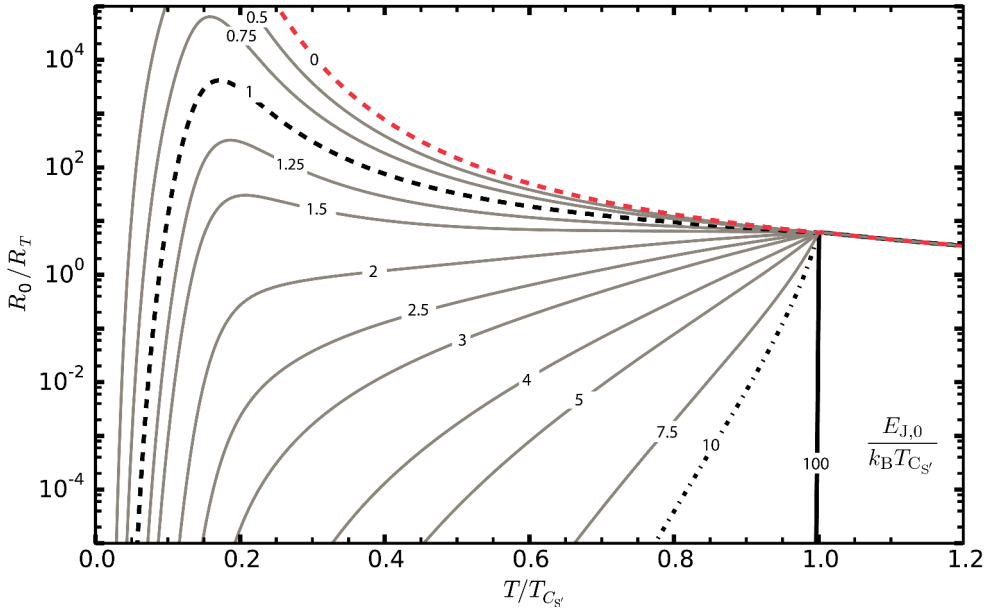

Figure 3.8. Zero bias resistance R_0 scaled by the normal state resistance R_T, as a function of temperature for several values of the ratio $E_{\mathrm{J},0}/k_\mathrm{B}T_{\mathrm{C_{S'}}}$, the latter parameter depending only on the normal state resistance once $T_{\mathrm{C_{S'}}}$ is fixed by the choice of material.

heating $P = IV$. In case of an NIN junction half of this energy is released in the first lead, while the other half – in the second one. The situation is different for a NIS junction, because in this case the superconducting gap acts as an energy filter. Under certain conditions it allows only *"hot"* quasiparticles to tunnel out of the normal metal, the latter is then left colder than before the tunneling event.

Quite generally, the temperature T of a small superconducting island S', coupled to a big superconducting lead S via a Josephson junction, should be found from the heat balance equation

$$\dot{Q}_{\text{e-ph}}(T, T_{\text{ph}}) + \dot{Q}_{\text{J}}(V, T, T_{\text{S}}) + \dot{Q}_{\nu}(T, T_{\text{env}}) + \dot{Q}_0 = 0. \tag{3.32}$$

Here $\dot{Q}_{\text{e-ph}}$ is the heat current from electrons to phonons. $\dot{Q}_{\text{J}}$ is the heat flow through a tunnel junction to the superconducting lead S, and it is the only term which is bias dependent; $\dot{Q}_{\nu}$ is the heat flow carried away by photons to an external environment. $\dot{Q}_0$ is either a spurious term accounting for a phenomenological heating from the measurement electronics, or the external heat flow applied to the sensor, in the case of a bolometer.

In what follows we consider the situation where the phonons, the superconducting lead S and the environment are at equilibrium so that $T_{\text{ph}} = T_{\text{S}} = T_{\text{env}} = T_{\text{bath}}$. For example we neglect the Kapitza resistance [133, 134] between the phonons in the island and the substrate, and as-

sume that the island is thermally connected to a single bath through different thermal conductances in parallel. Besides that, we will mainly consider the situation not far from equilibrium. Hence a linearized heat balance equation is sufficient for our purposes. It reads

$$\dot{Q}_0 = \left(G_{\mathrm{th,e\text{-}ph}} + G_{\mathrm{th,J}} + G_{\mathrm{th},\nu}\right)\delta T, \tag{3.33}$$

where $G_{\mathrm{th},x} = \partial \dot{Q}_x / \partial T$ are the heat conductances corresponding to the various heat transport processes described above. The heat conductances for typical sample parameters are plotted in Fig. 3.11.

3.4.1 Electron-Phonon heat conductance

The electron-phonon coupling originates from inelastic scattering between quasiparticles and phonons [135, 136], and leads to the excitation of non-equilibrium quasiparticles and to their relaxation or recombination. The general expression for the heat current from an electron subsystem with the temperature T to the phonon subsystem with the temperature T_{ph} is given by the integral [137]:

$$\begin{aligned}\dot{Q}_{\mathrm{e\text{-}ph}}(T, T_{\mathrm{ph}}) = &\frac{\Sigma \mathcal{V}}{24\zeta(5) k_{\mathrm{B}}^5} \int_0^\infty dE\, E^3 \big(n_{\mathrm{ph}}(E,T) - n_{\mathrm{ph}}(E, T_{\mathrm{ph}})\big) \times \\ &\int_{-\infty}^{\infty} d\epsilon\, n_{\mathrm{S}'}(\epsilon) n_{\mathrm{S}'}(E+\epsilon) \left(1 - \frac{\Delta_{\mathrm{S}'}^2}{\epsilon(E+\epsilon)}\right) \big(f_{\mathrm{S}'}(\epsilon) - f_{\mathrm{S}'}(E+\epsilon)\big)\end{aligned} \tag{3.34}$$

where $n_{\mathrm{ph}}(E,T) = 1/(e^{E/k_{\mathrm{B}}T} - 1)$ is the Bose distribution function of phonons, $\mathcal{V}$ is the volume of the superconducting island and Σ is a material parameter (see Table 3.1).

For a normal metal island one should put $n_{\mathrm{S}'}(\epsilon) = 1$, and the integral in the Eq. (3.34) can be solved analytically

$$\dot{Q}_{\mathrm{e\text{-}ph}}(T, T_{\mathrm{ph}}) = \Sigma \mathcal{V} \left(T^5 - T_{\mathrm{ph}}^5\right). \tag{3.35}$$

For a superconducting island we expect a different result since the density of states is now given by the BCS density of states Eq. (3.8). At low temperature, $k_{\mathrm{B}} T_{\mathrm{ph}} \ll k_{\mathrm{B}} T \ll \Delta$, the integral (3.34) can be approximated as [137, 138]

$$\begin{aligned}\frac{\dot{Q}_{\mathrm{e\text{-}ph}}}{\Sigma \mathcal{V}} \approx \frac{\pi}{3\zeta(5) k_{\mathrm{B}}^5} &\left(k_{\mathrm{B}} T \Delta_{\mathrm{S}'}^4 + \frac{7}{4} (k_{\mathrm{B}} T)^2 \Delta_{\mathrm{S}'}^3\right) e^{-2\Delta_{\mathrm{S}'}/k_{\mathrm{B}}T} \\ &+ \quad T^5\, e^{-\Delta_{\mathrm{S}'}/k_{\mathrm{B}}T}.\end{aligned} \tag{3.36}$$

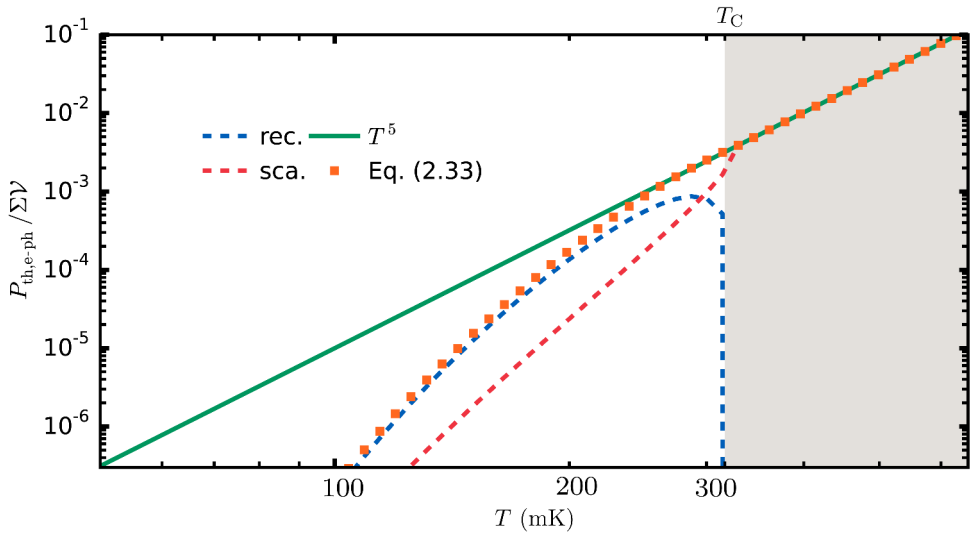

Figure 3.9. Electron-phonon heat current at $T_{\mathrm{ph}} = 0$ in a normal metal (full line) and in titanium with $\Delta_{\mathrm{S}',0} = 50\ \mu$eV (dotted line). The dashed lines represent recombination and scattering terms in Eq. (3.36).

The first line of this equation comes from recombination of quasiparticles, while the second one from small-energy scattering on phonons.

In Figure 3.9, we show electron-phonon heat current both in a normal metal and in a superconductor (titanium). The plot clearly demonstrates the reduction of the heat current in the superconducting state by an exponential factor $\mathrm{e}^{-2\Delta_{\mathrm{S}'}/k_{\mathrm{B}}T}$ at intermediate temperatures. In the case of a normal metal island, or a superconducting island near T_{C}, one finds

$$G_{\mathrm{th,e\text{-}ph}} \approx 5\Sigma\mathcal{V}T^4\,. \tag{3.37}$$

3.4.2 Heat transport through a tunnel junction

The heat current through a Josephson junction has been derived in [122, 139–141, I]. Here we will briefly summarize its main results and estimate the heat conductance of a tunnel junction, covering the NIN, NIS and SIS' cases.

Let us first consider a tunnel junction between two normal metals. The quasiparticle heat current is closely related to electrical current since every quasiparticle carries an energy ϵ,

$$\dot{Q}_{\mathrm{qp}}^{\mathrm{NIN}}(V) = \frac{1}{e^2 R_{\mathrm{T}}}\int d\epsilon\,(\epsilon - eV)\,[f_{\mathrm{L}}(\epsilon,\mu_{\mathrm{L}}) - f_{\mathrm{R}}(\epsilon,\mu_{\mathrm{R}})]\,. \tag{3.38}$$

The integration can be carried out analytically and the heat conductance[2]

[2] We consider the heat flow from the left side to the right side of the junction, so that $G_{\mathrm{th,qp}}^{\mathrm{NIN}} = \partial\dot{Q}_{\mathrm{qp}}^{\mathrm{NIN}}/\partial T_{\mathrm{L}}$

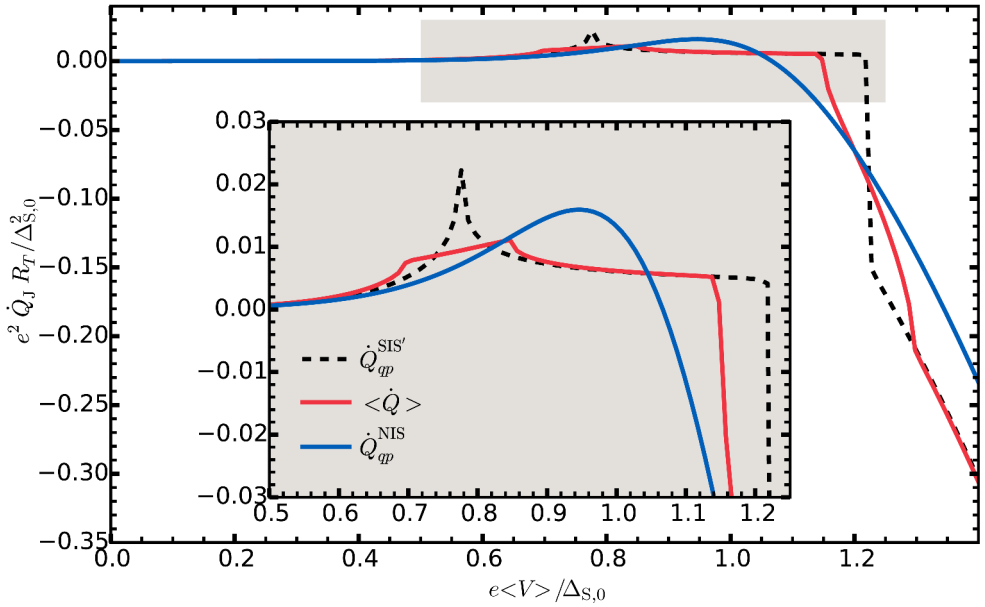

Figure 3.10. Heat transport trough a tunnel junction. The NIS case ($\Delta_{S',0} = 0$) is depicted as a blue line. Cooling takes place when a voltage $eV \approx \Delta_S - k_B T$ is applied across the junction. An extra feature appears in the SIS' cases (dashed line), at voltage $eV \approx \Delta_S - \Delta_{S'}$, leading to effective quasiparticle removal. This extra feature is smeared if one considers the full RCSJ model (red line).

is obeying the Wiedermann-Franz law :

$$G_{\mathrm{th,qp}}^{\mathrm{NIN}} = \frac{\pi^2 k_B^2}{3e^2 R_T} T\,. \tag{3.39}$$

Treating the NIS case is done by inserting the superconducting density of states inside the integral of Eq. (3.38). One can also get the same result by setting $\Delta_{S',0} = 0$ in the following discussion concerning a voltage biased Josephson junction. We use the same RCSJ model as previously and put $\varphi(t) = 2eVt/\hbar$. In this case the heat current from the weaker to the stronger superconductor takes the form

$$\dot{Q}_J^{SIS'}(t) = \dot{Q}_{qp}^{SIS'}(V) + \dot{Q}_{\cos}(V)\cos(\varphi(t)) + \dot{Q}_{\sin}(V)\sin(\varphi(t)). \tag{3.40}$$

Here $\dot{Q}_{qp}^{SIS'}(V)$ is the quasiparticle contribution, while the two other terms are related to the Josephson current and they oscillate in time.

The heat extracted from the S' side, in quasi-equilibrium at temperature T, of a S'IS junction by the quasiparticles is

$$\dot{Q}_{qp}^{SIS'}(V) = \frac{1}{e^2 R_T}\int d\epsilon\, n_{S'}(\epsilon - eV) n_S(\epsilon)(\epsilon - eV)\left[f_{S'}(\epsilon - eV) - f_S(\epsilon)\right]\,. \tag{3.41}$$

In the limit of low bias voltage and low temperature, $eV, k_B T, k_B T_S \ll \Delta_S -$

$\Delta_{S'}$, one finds

$$\dot{Q}_{\rm qp}^{\rm SIS'}(V) = \frac{\sqrt{2\pi}}{e^2 R_{\rm T}} \frac{\Delta_{\rm S}^{5/2}}{\sqrt{\Delta_{\rm S}^2 - \Delta_{\rm S'}^2}} \Big[\sqrt{k_{\rm B}T}\, e^{-\Delta_{\rm S}/k_{\rm B}T} \cosh \frac{eV}{k_{\rm B}T} - \sqrt{k_{\rm B}T_{\rm S}}\, e^{-\Delta_{\rm S}/k_{\rm B}T_{\rm S}} \Big], \tag{3.42}$$

$$\dot{Q}_{\cos}(V) = -\frac{\Delta_{\rm S'}}{\Delta_{\rm S}} \dot{Q}_{\rm qp}^{\rm SIS'}(V). \tag{3.43}$$

The contribution $\dot{Q}_{\sin}(V)\sin(\varphi(t))$ in Eq. (3.40) averages out to zero for any realization of phase fluctuation described by Eq. (3.30), therefore we ignore this term from now on.

The heat current averaged over the time and noise is expressed in the form similar to the average current (3.21), and under the same assumptions it reads

$$\langle \dot{Q} \rangle = \int_{-\pi}^{\pi} d\varphi \sigma(\varphi) \big[\dot{Q}_{\rm qp}^{SIS'}(I_{\rm x} R_{\rm S} - I_{\rm C} R_{\rm S} \sin\varphi) + \dot{Q}_{\cos}(I_{\rm x} R_{\rm S} - I_{\rm C} R_{\rm S} \sin\varphi)\cos\varphi \big]. \tag{3.44}$$

One can easily verify that $\langle \dot{Q} \rangle$ reduces to $\dot{Q}_{\rm qp}^{SIS'}(V)$ as soon as $E_{\rm J} = 0$. We will be interested in the limit of low bias and low temperature, $eV \lesssim k_{\rm B}T, k_{\rm B}T_{S'} \ll \Delta_{\rm S}, \Delta_{\rm S'}$. One can show that in this limit the heat conductance derived from Eq. (3.44) takes the form

$$G_{\rm th,J}(T_{\rm S'}) \approx \sqrt{\frac{\pi}{2}} \frac{\Delta_{\rm S}^2}{e^2 R_{\rm T}} \frac{\Delta_{\rm S}}{\sqrt{\Delta_{\rm S}^2 - \Delta_{\rm S'}^2}} \sqrt{\frac{k_{\rm B}T}{\Delta_{\rm S}}} \frac{1}{T} {\rm e}^{-\Delta_{\rm S}/k_{\rm B}T} \times \left[1 + \frac{2\Delta_{\rm S}}{k_{\rm B}T} + \frac{e^2 \langle V \rangle \sqrt{I_{\rm C}^2 R_{\rm S}^2 + \langle V \rangle^2}}{(k_{\rm B}T)^2} \left(\frac{\Delta_{\rm S}}{k_{\rm B}T} - \frac{3}{2} \right) \right]. \tag{3.45}$$

3.4.3 Photonic heat current

For completeness, we also consider the energy exchange mediated by photons between the electron gas in the island and the environment. This problem has been addressed theoretically in Refs. [142, 143]. If one models the island and the environment by resistors $R_{\rm e}$ and $R_{\rm env}$ respectively, the net heat flow acquires the form

$$\dot{Q}_{\nu}(T_{\rm e}, T_{\rm env}) = \int_0^{\infty} \frac{d\omega}{2\pi} \frac{4 R_{\rm e} R_{\rm env}}{|Z_{\rm t}(\omega)|^2} \hbar\omega \left[n_{\rm e}(\omega) - n_{\rm env}(\omega) \right], \tag{3.46}$$

where $Z_{\rm t}(\omega)$ is the total series impedance including possible losses in the connection between the two resistors, and $n_{\rm e,env}(\omega) = 1/({\rm e}^{\hbar\omega/k_{\rm B}T_{\rm e,env}} - 1)$

are boson occupation factors. For lossless connection between the two systems, the corresponding heat conductance reads

$$G_{\mathrm{th},\nu} = r_0 \frac{\pi k_\mathrm{B}^2 T}{6\hbar} \equiv r_0 G_\mathrm{Q}, \tag{3.47}$$

where $r_0 = 4R_\mathrm{e}R_\mathrm{env}/(R_\mathrm{e}+R_\mathrm{env})^2$ is the matching factor and $G_\mathrm{Q} = \pi k_\mathrm{B}^2 T/6\hbar$ is the quantum of heat conductance. Radiative thermal coupling has been demonstrated experimentally in several experiments [144, 145]. In all of those systems the matching factors were close to 1, $r_0 \approx 1$. In our experiments the matching between the environment and the sample is expected to be much worse, especially in the sub-gap regime where the impedance of the sample can be as high as few GΩ. In addition, the connection between the environment and the device has its own cut-off frequency, reducing further the coupling [146]. We estimate the effective photonic heat conductance to be $G_{\mathrm{th},\nu} \approx 10^{-4} \times G_\mathrm{Q}$ for our typical sample. This number is small enough for the photonic heat current to be negligible compared to electron-phonon coupling at high temperature. Nevertheless, this term can set the lower bound of the sum of the heat conductances at low enough temperature, as can be seen by extrapolating the temperature axis of Fig. 3.11.

3.4.4 Comparison of the heat conductances

In Figure 3.11, we have compared the different heat conduction channels for a typical sample with the parameters summarized in the caption. Few remarks can be made. First, unless the temperature is really low, the radiative thermal coupling can be neglected. Second, one can see that in order to isolate the system using NIN tunnel junctions, the junction resistances should be large, typically above a few hundreds of kΩ. In contrast, NIS tunnel junctions efficiently suppress heat escape from the island in a wide range of sub-gap bias voltages. The quality of the junction (i.e. Dynes parameter γ) influences the degree of its thermal isolation.

In the experiments, we usually neglect the heat conductance trough the tunnel junction at zero bias compared to the electron-phonon coupling. This approximation is supported by the large impedance of our typical junction.

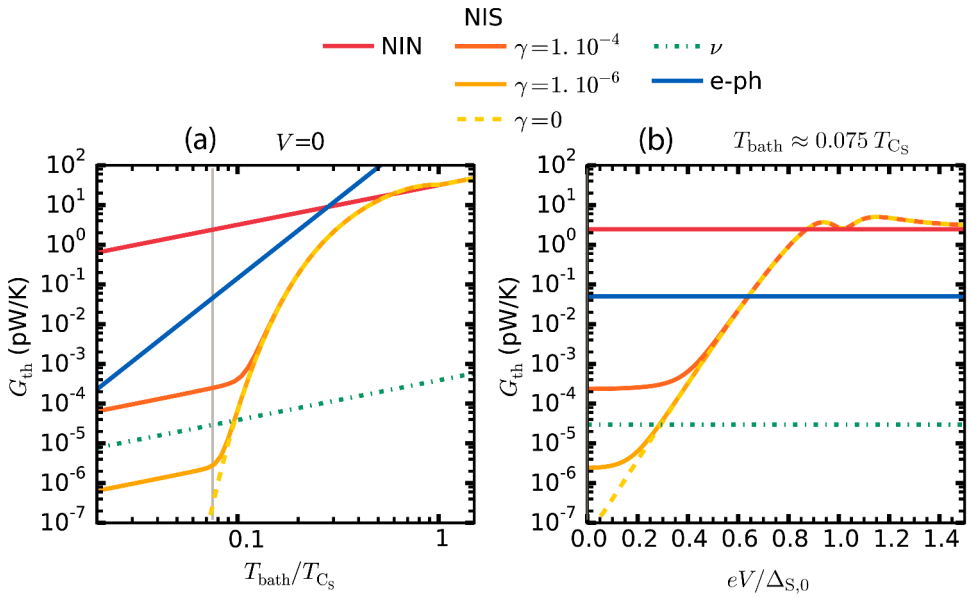

Figure 3.11. Comparison of the different heat conductances for a *typical* sample based on a normal island ($\Sigma\mathcal{V} = 0.1\,\mathrm{nW/K^5}$) connected to a superconducting lead ($\Delta_{\rm S,0} = 200\,\mu\mathrm{eV}$) with a tunnel junction ($R_{\rm T} = 1\,\mathrm{k\Omega}$). We account for poor matching between the lines and the sample by setting $G_{\rm th,\nu} \approx 10^{-4} \times G_{\rm Q}$

3.5 Electronic heat capacity

The heat capacity of an electronic system influences its finite frequency dynamics. With respect to the internal energy at zero temperature $U(0)$ one may write for the normal state electrons in equilibrium

$$U(T) - U(0) = 2\nu_{\rm N}\mathcal{V}\int_0^\infty d\epsilon\, \epsilon f(\epsilon)\,. \tag{3.48}$$

By definition, $\mathcal{C}_{\rm N} = dU(T)/dT$, and thus

$$\mathcal{C}_{\rm N} = \frac{2\nu\mathcal{V}}{k_{\rm B}T^2}\int_0^\infty d\epsilon\, \epsilon^2 f(\epsilon)\,[(1-f(\epsilon)] \tag{3.49}$$

$$= \frac{\pi^2}{3} 2\nu\mathcal{V}k_{\rm B}^2 T\,, \tag{3.50}$$

where in the last stage we assumed f to be the Fermi-Dirac distribution. In the literature, one usually refers[3] to $\gamma_{\rm T}$ defined by $\mathcal{C}_{\rm N}/\mathcal{V} = \gamma_{\rm T} T$ [59], so that for the free electron model one has $\gamma_{\rm T} = \frac{mk_{\rm F}k_{\rm B}^2}{3\hbar^2}$. The measured values of $\gamma_{\rm T}$ for few metals can be found in Table 3.1.

In the superconducting case, Eq. (3.48) has to be modified to account for the density of states. The heat capacity is modified accordingly and reads

$$\mathcal{C}_{\rm S} = 2\nu_{\rm N}\mathcal{V}\int_\Delta^\infty d\epsilon\epsilon\, n^{\rm BCS}(\epsilon)\, f(\epsilon)\left[\frac{\epsilon}{k_{\rm B}T^2}\,(1-f(\epsilon)) + \frac{\Delta}{\epsilon^2-\Delta^2}\frac{d\Delta}{dT}\right]. \tag{3.51}$$

[3] We added the index $_{\rm T}$ to avoid the confusion with the Dynes parameter γ

At low temperatures ($k_\mathrm{B}T \ll \Delta$) the heat capacity is suppressed by the factor

$$\mathcal{C}_\mathrm{S}/\mathcal{C}_\mathrm{N} = \frac{3\sqrt{2}}{\pi^{3/2}} \left(\frac{\Delta}{k_\mathrm{B}T}\right)^{5/2} \mathrm{e}^{-\Delta/k_\mathrm{B}T} \tag{3.52}$$

as compared to the normal state value at the same temperature. A small heat capacity is increasing the calorimetric response of a system described by Eq. (2.12). Thus, a calorimeter using a superconductor as an absorber will see its responsivity greatly enhanced as the temperature is lowered below Δ.

Table 3.1. Material constants. The Fermi velocity v_F and the density of state ν are calculated at the Fermi energy E_F using the free electron model [59]. The heat capacities γ_T are measured [70]. The values of the diffusion constant D are usually extracted from weak localization measurements at low temperature. The electron-phonon coupling Σ values are also measured in various experiments, whose references can be found in [122]. All the values given for titanium are taken from [147].

	E_F	v_F	γ_T	ν_N	D typ.	Σ
	eV	10^6 ms^{-1}	Jm^{-3}K^{-2}	10^{47} J^{-1}m^{-3}	cm^{2}s^{-1}	nWK$^{-5}\mu$m^{-3}
Al	11.7	2.03	135	1.15	50 [148]	0.3
Ag	5.49	1.39	64	1.03	60-120 [148, 149]	0.5
Au	5.53	1.40	67	1.0	1 [150]	2.4
Cu	7.0	1.57	97	1.45	100 [149]	2.0
Ti	1.42	0.32	310	7	4	1.3

4. Experimental methods

The measurements presented in this thesis have been performed on devices fabricated in the Micronova clean-room facility [the Otaniemi research infrastructure for Micro and Nanotechnologies (OtaNano)]. We employ micro and nano fabrication techniques as briefly summarized below. The apparatus needed to perform the electrical transport measurements at low temperatures will be described in the second half of this chapter.

4.1 Device fabrication

We fabricate our devices using shadow angle deposition, also called Dolan technique [151, 152], and all steps are summarized in Fig. 4.1 (a)-4.1 (b). The main idea is to pattern a suspended mask, which is then metallized using two different angles. The tunnel junctions are formed within the overlapping areas of these two films. The device fabrication can be divided into two main parts : the pattern definition [Fig. 4.1 (a)] and its metallization [Fig. 4.1 (b)].

4.1.1 Pattern definition

Electron Beam Lithography (EBL) is a cornerstone of nano fabrication. Some incident electrons are accelerated to a high energy (100 keV) and directed toward the wafer. They are then scattered in silicon, creating lower energy secondary electrons which break the chains of a polymer resist. The exposed resist then becomes more soluble in a specific developer (typically Methyl IsoButyl Ketone, or MIBK in short). Resolution and sensitivity vary between different resists in use. The better the resolution is

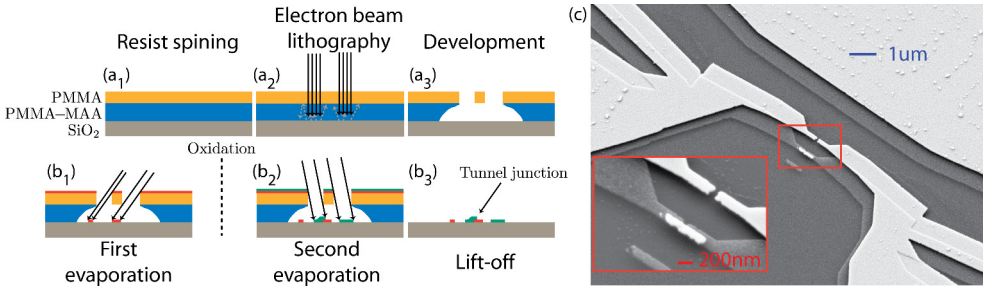

Figure 4.1. Device fabrication. (a) and (b) Step-by-step fabrication process illustrating the shadow angle deposition technique. Details are given in the text. (a_1) Wafer covered with a bilayer of resist. The areas exposed with electrons (a_2) are the areas to be removed (positive resist) by the developer (a_3). The first film is deposited under a positive angle (b_1) before oxidization. The second film is then deposited with another angle (b_2), a tunnel junction is created in the overlapping area. (b_3) The extra resist is then removed in an acetone bath. (c) Scanning Electron Micrograph (SEM) of a typical sample. The lighter film is titanium, the darker one is aluminium.

(how fine a detail can be patterned), the worse is the sensitivity (related to the dose, or how many electrons are needed to break a polymer chain). In order to create the suspended mask, a bilayer is used, as depicted in Fig. 4.1 (a_1). The top layer, defining the pattern, needs to have a high resolution. A thin layer (typ. 100nm) of PMMA (polymethyl methacrylate) serves this purpose. One can add to this top layer an even thinner (20-30 nm), mechanically more robust germanium layer forming a "hard mask" [153] version of the process, the main advantage being better resolution. The bottom layer needs to be much more soluble and thus more sensitive to the electron exposure, in order to create a large enough undercut needed for the angle deposition. PMMA-(8.5)MAA (a mixture of PMMA and 8.5% methacrylic acid) is then used. The thickness of this bottom layer sets an upper limit to the possible shift between the two films called shadows. Both resist layers are spin-coated onto the wafer, tuning the spinning speed allows one to tune the final resist thickness. In principle, nothing prevents spinning more than one layer of copolymer to increase its thickness. Samples presented in this thesis typically employ from two to three MMA layers, resulting in a total thickness of about 1 μm, and allowing a lateral shift of subsequently deposited shadows up to about 2 μm.

After exposure to the electron beam [Fig. 4.1 (a_2)], the resist is developed in MIBK for 20-60 s at room temperature. The development time depends both on the received dose and on the geometry. As the MMA dissolves faster than the top PMMA layer, it allows one to create the undercut needed for the angle deposition [Fig.4.1 (a_3)].

4.1.2 Metal deposition

We are depositing metal films using a high vacuum electron beam evaporator, with in-situ argon plasma gun[1]. After the argon plasma, the metal deposition itself can be started. The electron beam heats a target made of the material to be deposited, which then evaporates (or sublimates). After the first layer has been deposited [Fig. 4.1 (a_3)], introducing oxygen into the chamber (typ. 0.4 mbar during 1 min) allows the metal to oxidize, creating an oxide barrier [Fig. 4.1 (b_1)]. High quality tunnel junctions can be obtained with aluminium / aluminium oxide junction (Al/AlO_x), explaining the popularity of this material for this purpose. The second layer can then be deposited to create the overlapping junction(s) [Fig. 4.1 (b_2)]. The interface between the two metals is an important factor for many physical processes [92] and justifies the use of buffer layers, as explained below.

The last step of the fabrication process is to dissolve the remaining resist, removing at the same time all the metal which has been deposited on top. This operation, called lift-off, is typically done by immersing the chip into acetone until all the traces of resist disappear [Fig. 4.1 (b_3)].

Titanium. The transition temperature of a thin titanium film is known to depend on the deposition conditions [121]. The critical temperature of titanium is easily reduced below its bulk value in dirty conditions, or with a poor material quality. On the other hand, evaporated thin films can reach T_C of about 0.6 K, well exceeding the bulk value of 0.38 K. A suspected reason for such variations is the fact that titanium is a very strong getter material. Thus, increasing the deposition rate is one solution to obtain good film quality, but we observed a degradation of the carbon crucible containing the titanium when a too strong electron beam is used. A special care has been taken to clean the evaporation chamber, but these fluctuations of the film quality are still an issue for all devices based on

[1] Using a mild argon plasma after the development to roughen the surface of the resist helps the lift-off process. A continuous flow of argon gas is provided to the gun, where the gas is turned into a plasma using a microwave source (~ 300 W). The ions constituting the plasma are then accelerated by a voltage of 1-2 kV toward the sample holder. The ion current is of the order of 200 μA distributed on a 50 mm^2 area. The Ar pressure inside the chamber is maintained at around 2×10^{-5} mbar. We call this process a *mild* plasma in comparison with the plasma used to etch metals, which would require currents at least an order of magnitude higher.

superconducting titanium.

Another trouble arises from the junction quality, when Al/AlO_x is put in direct contact with titanium, probably originating from the diffusion of oxygen in the titanium layer. For this reason, a thin aluminium layer (2-3 nm) is usually evaporated prior to the titanium film deposition to form an Al/AlO_x/Al/Ti junction. This thin aluminium buffer layer does not interfere with titanium superconductivity, as it is fully proximized by the thicker titanium layer.

Device characterization. Inspecting for possible major defects in the fabricated device, is usually performed with the help of a Scanning Electron Micrograph (SEM, [154]). An example can be seen in Fig. 4.1 (c). SEM gives information about the structural integrity, the junction size, the grain size, etc. Atomic Force Microscope (AFM) image is a good complement of an SEM image (see [155] for a description of an AFM). This imaging method allows one to measure the exact thickness of the metal layers.

4.2 Electrical transport measurements at low temperature

In this section we will discuss the apparatus needed to measure the electrical properties of a sample at low temperatures. First the cryogenic apparatus will be briefly introduced, motivating the choice of a $^3He/^4He$ dilution refrigerator. Then, an essential part of such a setup, the wiring, will be addressed.

4.2.1 Cryogenic apparatus

Measurements involving superconductors usually require a sophisticated cryogenic apparatus allowing to refrigerate the device below its superconducting critical temperature (1.3 K for Al films, 300 mK for Ti). $^3He/^4He$ dilution refrigerators are the most convenient system to perform measurement at around 100 mK and below. A detailed description of this kind of a refrigerator is found in [70], but we briefly review its main features. The cooling power of a dilution refrigerator comes from energy needed to mix ^3He into a diluted $^3He/^4He$ phase. The ^3He can be removed from the dilute phase by pumping. Re-injecting it provides a closed cycle

operation with a cooling power $\dot{Q} = 84\dot{n}T^2$ where $\dot{n}$ is the molar flow of ^{3}He per unit time. This way, the circulating ^{3}He is carrying away some heat from the mixing chamber where the experiment is thermally anchored. All measurements were performed in a Plastic Dilution Refrigerators (PDR) [156] immersed in a liquid ^{4}He bath at 4.2 K. The cooling power of such a dilution refrigerator is around $50\,\mu$W at 100 mK, which is sufficient for the measurements reported here. The minimum achievable temperature is around 30 mK, measured by a ruthenium oxide thermometer (RuOx) calibrated against Coulomb Blockade Thermometer (CBT), the latter being a primary thermometer.

In addition to the PDR a dry dilution refrigerator is at our disposal. Its main advantages are a larger cooling power (250 μK at 100 mK) and a smaller base temperature (7 mK). In a dry dilution refrigerator, the liquid ^{4}He bath is replaced by a mechanical cryo-cooler [70]. This dry dilution refrigerator is preferred to the PDR for radio-frequency measurements [157, 158] where components like circulators and filters can be fiited at at low temperatures (typ. at 4 K), improving their performance.

4.2.2 Shielding and filtering

Noise is detrimental in two ways. First, superimposed to the measured signal, noise is degrading the information by increasing the variance of the signal. Secondly, noise has a direct influence on the signal itself, as seen for example in the Langevin equation associated with the RCSJ model of a Josephson junction [Eq. (3.26)]. A comprehensive review of major cryogenic filters can be found in [159]. All filters presented in this review aim to suppress high frequency noise using an RC or a lossy filter. In the following lines, we will introduce the solution that is in use in our laboratory, emphasizing that this already demonstrates excellent results on highly resistive samples such as a SINIS turnstile [137].

Manganin twisted pairs are used between room temperature and 4 K, where the thermalization of the wires has to be done carefully. They are commercially available as loom of manganin wire (110 μm in diameter), twisted to avoid picking extra magnetic noise. The absence of a shield allows to reduce the global heat leak along the wire and provide an easier thermalization, see Fig. 4.2 (a). The resistivity of twisted pairs is around 60 Ω/m, providing a high frequency cut-off at around 1 GHz [160]. Their

flexibility makes then easy to mount, but on the other hand they are more sensitive to vibration, which is often responsible for low frequency noise (microphonic pickup noise).

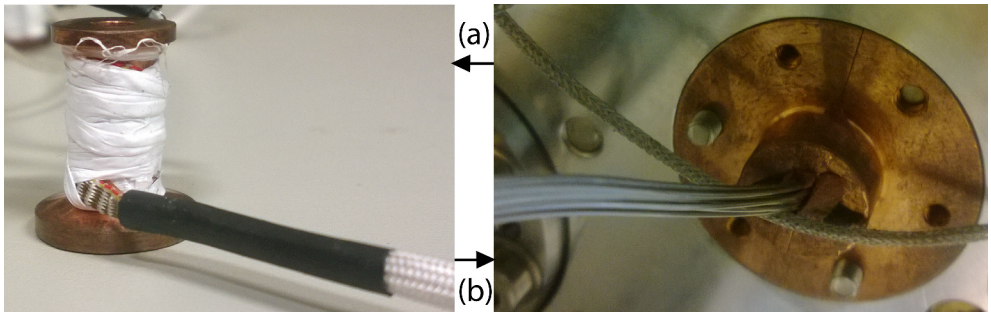

Figure 4.2. Wiring and thermalization. (a) 12 manganin twisted pairs assembled as a loom, thermalized around a copper coil. The Teflon tape is maintaining temporarily the loom around the copper coil. (b) Harness of thermocoax lines clamped by two copper half sleeves, fixed on the 4K stage on a dry dilution refrigerator.

Thermocoax is a commercial coaxial cable developed as a vacuum compatible heater element. It uses stainless steel as a shield and magnesium oxide as an insulator, and thus this cable provides the low thermal conduction needed in a cryogenic apparatus. Thermocoax uses skin effect in the nickel-chromium inner part (60 Ω/m) to attenuate drastically high frequency noise [161]. The rigidity of such a cable combined with its relative fragility makes it relatively hard to install but the rigidity of a dozen of thermocoax cables tight together [Fig. 4.2 (b)] is such that microphonic pick-up is efficiently suppressed.

A well shielded sample stage prevents high frequency noise which would excite quasi-particles in superconducting aluminium (where $\Delta \approx 50$ GHz) [162]. The sample is enclosed in a box usually made out of brass, or copper. The cover [Fig. 4.3 (a)] is sealed using an indium toric joint [Fig. 4.3 (b)] making the box vacuum and radiation tight. A second cover [Fig. 4.3 (c)] is screwed in addition to further decrease possible leakage in the joint. As every electrical cable represents an open hole to the outside world, the number of cables is reduced to the minimum. Metallic coaxial lines enable soldering the outer shield hermetically to the box. If thermocoax lines are used, no other attenuation is needed, but the cables have to be thoroughly thermalized. This is done in two steps. First a significant length of cable is glued to the body [Fig. 4.3 (d)] using conductive two component epoxy charged with silver powder. Second, a special care is taken to ensure a good thermal contact between the Printed Circuit Board [PCB, Fig. 4.3 (d)] and the stage. The bottom of the PCB is separated from

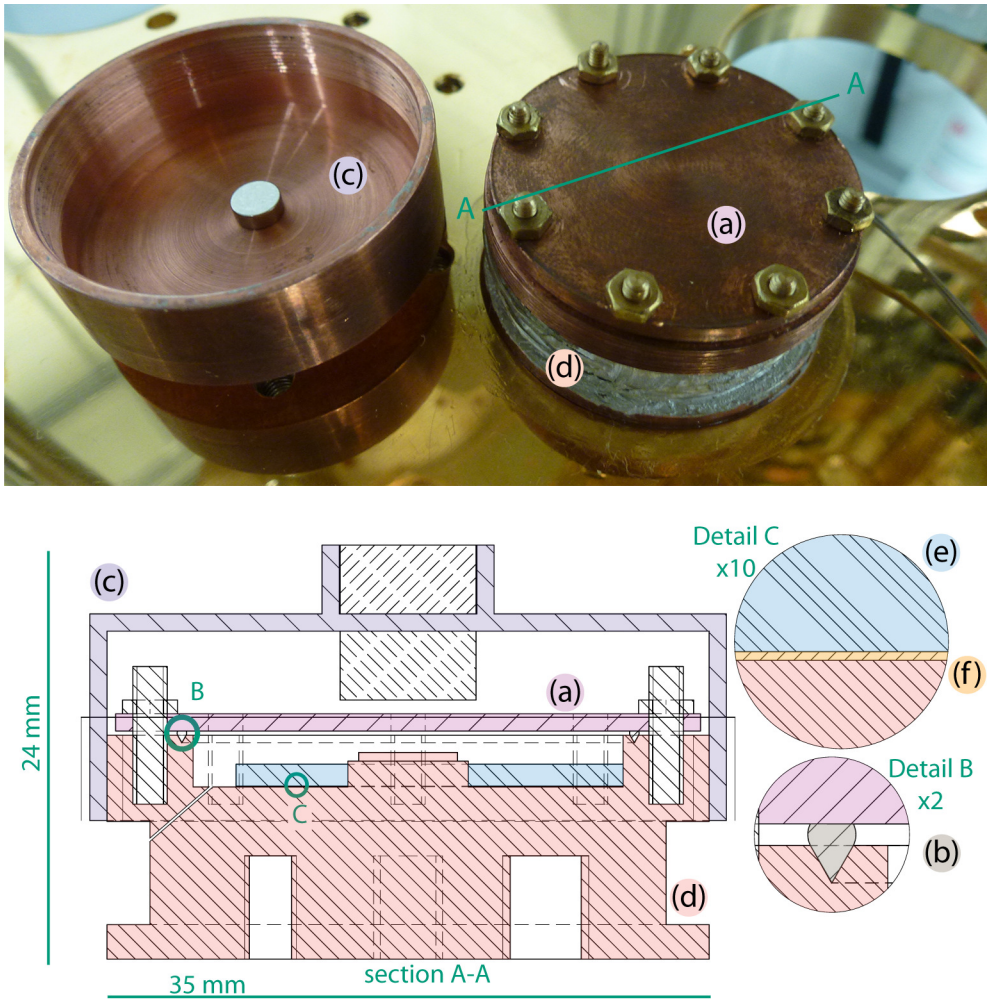

Figure 4.3. Picture of a double shielded sample stage (top) and its cross section (bottom). The sample stage is closed with cover (a), made radiation tight by an indium toric joint (b). A second cover (c), here supporting a magnet, is providing an extra level of attenuation. Two thermocoax cables are thermalized around the copper body (d) using silver epoxy. The full sample stage is screwed from the bottom to the mixing chamber flange of a dry dilution refrigerator. The sample, a commercial CBT, is connected to a PCB (e) thermally anchored to the body using a thin grease layer (f).

the body by a thin layer of grease [Fig. 4.3 (f)] to provide a good thermal contact. A resistor, or a discrete RC network might be used to further increase the thermal coupling between the electrical lines and the box. Last but not least, the box has to be thermally anchored to the mixing chamber plate of the dilution refrigerator. Gold coating of the box is of great help to avoid the oxidization of the copper surfaces. Gold plating can be replaced by a fine layer of grease remembering that the heat conductivity of such a grease layer is orders of magnitude smaller than the equivalent metallic layer. The key advantage of using grease is the enhanced contact area. We used such a sample stage to measure a Coulomb blockade thermometer (CBT) which is used as a temperature reference in one of the dilution refrigerators.

Our cryogenic lines are usually a combination of twisted pairs (from room temperature to 1 K) and thermocoax (from 1 K to the sample stage at 50mK). Typical resistances are of the order of 400 Ω in combination with a capacitance of few nF. The use of an indium shield is made optional by the nature of the devices measured, with low impedance junctions. The bandwidth of the measurements is limited by a combination of cryogenic line capacitance and the largest resistance of the setup. Usually, the latter is either the sample impedance in a voltage biased scheme or the biasing resistor in a current biased scheme. The different measurement setups will be addressed in the next part.

4.3 Transport measurements

We are studying resistive thermometers, in which the resistance of the device is a function of the temperature. We will describe first how to perform a DC characterization of a non-linear component by measuring its Current-Voltage (*I*-*V*) characteristics. The next topic, the current biased phase-locked scheme, allows one to increase the precision of the measurement of a resistance compared to a DC characterization. Both DC and phase-locked scheme precision is limited by the noise of the first stage amplifier. Modeling such an amplifier allows one to optimize the global noise level of the thermometer. Next, in order to get the frequency spectrum of the thermometer signal, the output of the thermometer is sampled using a analog-to-digital acquisition card. The signal acquired this way is used to measure the noise of the thermometer, summing both internal sources of noise (like the temperature fluctuations) and external sources of noise (like the voltage noise of the amplifier). It leads to the pragmatic definition of the Noise Equivalent Temperature $\mathrm{NET}_{\mathrm{amp}}$ of a thermometer whose precision is limited by the noise of its readout electronic.

4.3.1 Current-Voltage (*I*-*V*) characteristics

I-*V* characteristics are usually measured with a 4-probe method allowing one to exclude the wire impedances from the measurement. Typical resistance of a NIS junction can vary from the kΩ to the GΩ range inside the gap, thus they are preferably voltage biased. The biasing net-

work acts as a perfect voltage divider as soon as the junction resistance is larger than the line resistance. On the contrary, when measuring supercurrent, the impedance can be much smaller than the line resistance. Then, a room temperature voltage bias is not working anymore and one has to use either a low temperature voltage bias resistor R_{shunt}, or consider to bias the device using current instead of voltage. The first solution is limiting the maximum voltage one can apply to the sample as a power $V_{\mathrm{bias}}^2/R_{\mathrm{shunt}}$ is dissipated at low temperatures. This extra heat flow might be enough to warm up the dilution refrigerator in which the experiment takes place. The second solution requires a large bias resistor if one wants to measure both the supercurrent and the sub-gap impedance, thus limiting the measurement bandwidth. In most cases this is not detrimental as *I-V* characteristics are measured in a quasi-DC manner.

4.3.2 Phase-locked measurement

Phase-locked measurement (also called Lock-In measurement) is a method especially efficient to measure a general impedance $Z_{\mathrm{t}} \equiv R + iX$. In addition, it reduces the overall noise by efficiently reducing the measurement bandwidth. R is the resistive part of the impedance, and X, the reactance, accounts for the capacitive and/or the inductive part of the impedance. Considering non linear *I-V* characteristics (such as for a diode, or a NIS tunnel junction), one can define the dynamical impedance as $Z \equiv dV/dI$ which differs from the total impedance Z_{t}. Taking a NIS tunnel junction at zero temperature as an example, one has $dV/dI(V) \propto 1/n_{\mathrm{S}}(V)$ leading to a simple way to measure the density of states, known as electrical spectroscopy. In this example the impedance is purely resistive, even if in real cases the impedance is complex, for instance due to the capacitance of the filtered lines.

In a current biased phase-locked measurement, a drive signal dI is generated at a frequency f_0, and the resulting dV is measured by a Lock-In amplifier, which is demodulating dV by mixing it with a copy of the drive signal[2]. Finally, the demodulated signal is averaged over a time τ (equivalent to a low pass filter). This integration time τ has to be larger than $1/f_0$ and can be increased to reduce the bandwidth, therefore allow-

[2]Amplitude demodulation by mixing with the carrier has been supplemented by numerical methods, where the signal is digitized before extracting the component at f_0.

ing efficient noise rejection.

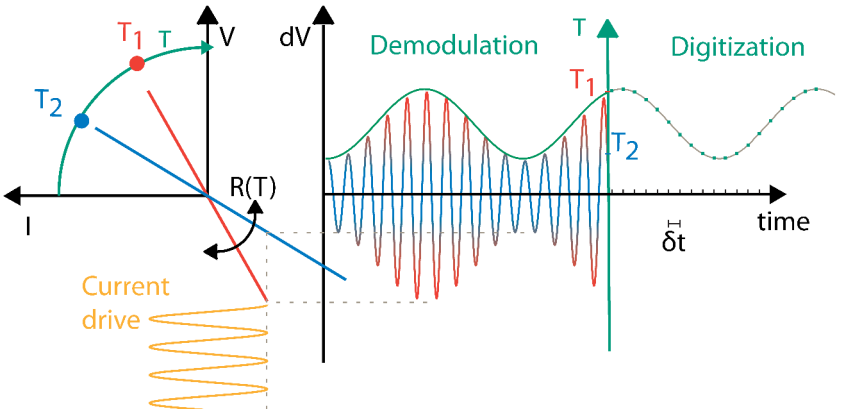

Figure 4.4. Illustration of zero bias thermometry: modulation, demodulation and digitization. The temperature variation is depicted as a sine wave of period larger than the driving period. The measured signal dV is then amplitude modulated (blue-red line). The Lock-In amplifier is extracting the amplitude of dV (green solid line) and generates an analog signal proportional to it. This signal is finally digitized by a DAC card, with a time step δt (green point).

In practice, a Lock-In amplifier is extracting the two components (amplitude and phase) needed to characterize fully the complex impedance Z. When using the zero bias impedance as a thermometer (see Fig. 4.4), a sinusoidal current of amplitude dI is applied to the device and the signal dV is amplified and fed into the Lock-In amplifier. The Lock-In amplifier is generating two analog signals corresponding to the amplitude $|dV|$ and phase θ of $dV = |dV|\ \mathrm{e}^{i\theta}$, so that the zero bias resistance is simply $|dV|/dI$ ($\theta \ll 1$). The maximum frequency of these analog outputs is set by the lock-in amplifier to 100 kHz. The real bandwidth limitation of this particular measurement scheme comes from the lock-in integration time τ typically around 100 ms leading to a bandwidth of a few Hz.

4.3.3 Noise model

Both DC and Phase-locked measurement are limited by the voltage noise created by the measurement chain. The noise model below is based on the observation that the first stage amplifier is usually the main source of noise.

Few definitions are helpful for the following discussion. The noise discussed in this thesis always refers to the *input* of the measurement chain, although it is measured at the *output*. This way, the total noise of two cascaded voltage amplifiers of gain G_1 and G_2, with respective voltage noise v_1 and v_2 is $v_{1+2} = \sqrt{v_1^2 + (v_2/G_1)^2}$. This formula, valid as long as

the noise voltages v_i are uncorrelated[3], is easily extended to the case of n cascaded amplifiers. Knowing the noise voltage v_i of an amplifier, we can define $\mathrm{F}_i = \frac{v_i^2}{4k_\mathrm{B}T_0R_\mathrm{s}}$, which is related to the noise factor $\mathcal{F}$ by $\mathcal{F} = 1 + \mathrm{F}_i$. The noise factor represents how much noise the amplifier under test adds to the Johnson noise of an input resistor R_s kept at the temperature T_0. This noise factor is sometimes expressed in terms of an equivalent noise temperature $T_i = T_0 \times \mathrm{F}_i$. The noise figure $\mathrm{NF_{dB}} = 10\log_{10}(1 + \Sigma_i \mathrm{F}_i)$ is usually given as a figure of merit of an amplifier, and is depicted in Fig. 4.5 (b) as a function of the sample impedance R_s and of the frequency.

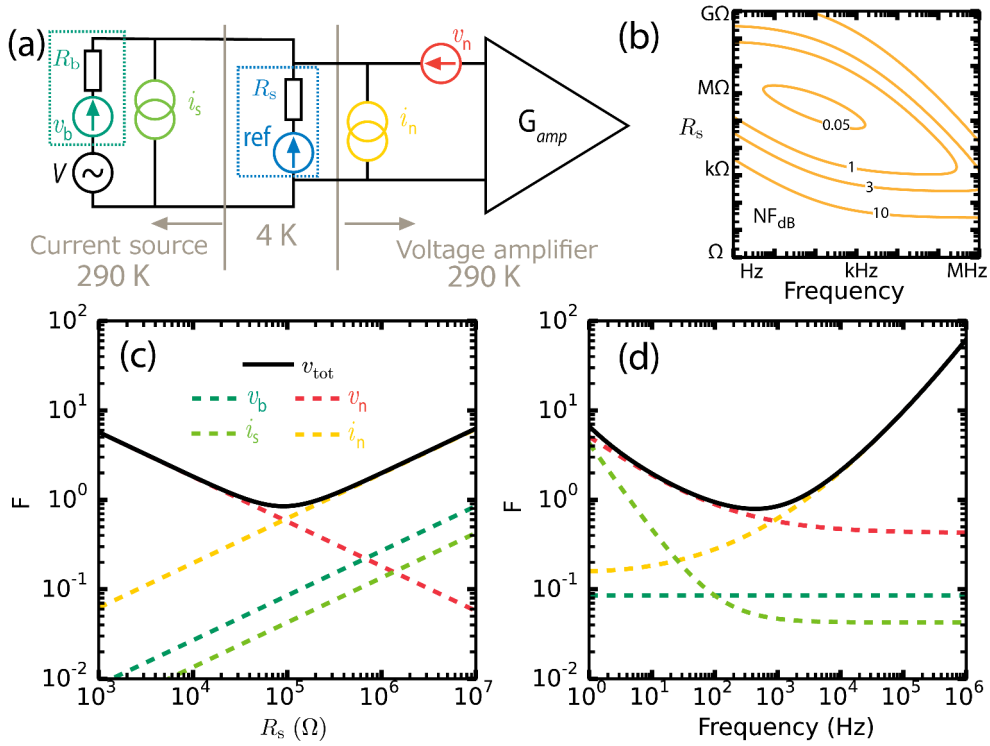

Figure 4.5. Noise model. (a) Scheme of a basic measurement setup. The bias resistor is set to $R_\mathrm{b} = 1$ GΩ. Note that no effect of filtering lines has been considered. (b) Empirical reproduction of a noise figure at 290 K, which is close to the one of the voltage pre-amplifier used in the measurements. In this example, the best noise performance (NF ≈ 0.04 dB) corresponds to a noise temperature of around 3.5 K. (c) and (d) Noise factor F as a function of the sample resistance [f=1 kHz, (c)] and the frequency [$R_\mathrm{s} = 100$ kΩ, (d)]. The noise figure (b) is used to reproduce the behavior of a typical low noise voltage pre-amplifier. The reference is the Johnson noise of a resistor R_s at 4 K, i.e. $\approx 0.47\mathrm{nV}/\sqrt{\mathrm{Hz}}$ for $R_\mathrm{s} = 1$ kΩ.

The noise model is depicted in Fig. 4.5 (a). For simplicity we will consider a sample of impedance R_s biased by a resistor R_b kept at room temperature (T) which generates the Johnson noise v_b. The voltage source is not perfect and generates extra current noise i_s. The voltage amplifier is modeled by a current noise source i_n and a voltage noise source v_n con-

[3] If the two noise voltages v_1 and v_2 are correlated, the sum v_{1+2}^2 is given by $v_{1+2}^2 = v_1^2 + (v_2/G_1)^2 + \Gamma_{1,2}v_1v_2/G_1$, where Γ is the covariance matrix.

nected to a perfect amplifier with gain G_{amp} [163]. Figures 4.5 (c) and 4.5 (d) are depicting the noise factor of the amplifier used to perform the measurements described in this thesis. First, we can see that the noise of the amplifier is dominating, for all source resistances and all frequencies, if the biasing impedance is large enough. In Fig. 4.5 (b), one can remark that an optimum impedance $R_{\mathrm{n}} = v_{\mathrm{n}}/i_{\mathrm{n}}$ exists, for which the output noise is minimum. In that case, the amplifier is said to match the source impedance. This optimum noise factor is achieved over a broad range of frequencies. Nevertheless, 1/f noise component make the situation worse by an order of magnitude at low frequency (1-100 Hz depending of the amplifier model). Under the assumption that all the previous noise sources are not correlated, the total noise voltage referred to the input of the amplifier is given by

$$v_{\mathrm{tot}}^2 = \sqrt{v_{\mathrm{b}}^2 + R_{\mathrm{s}}^2(i_{\mathrm{s}}^2 + i_{\mathrm{n}}^2) + v_{\mathrm{n}}^2}\,. \tag{4.1}$$

In the general case where the information about the correlation is unknown, we define n_{f} as the voltage noise of the measurement scheme, in V/$\sqrt{\mathrm{Hz}}$. Its measurement is the topic of the next paragraph. This number is usually close to the voltage noise of the first stage amplifier as given in the datasheet for small values of impedance measured.

4.3.4 Analog to digital conversion

Once the signal has been amplified (and demodulated, in case of a Phase-locked measurement), we use a Digital-Analog Converter (DAC) to acquire it and store it in digital form. The data acquired by this means are eligible for any numerical treatment [164], as filtering, averaging, or Fast Fourier Transformation (FFT). The latter treatment is especially interesting as it allows one to extract the spectral density from the real-time signal. The work of Shannon [165] illuminates the sampling process and the treatment of the signal. The spectral density characterizes the noise properties of the studied device.

Signal acquisition with a DAC allows one to sample a voltage at a fixed frequency f_{acq} during a time T. After a Fourier transform, the spectrum obtained will cover the frequency range $[1/T, f_{\mathrm{acq}}/2\,]$. As $f_{\mathrm{acq}}^{max} \approx 200$ kHz, usually a low-pass filter is inserted before the DAC. This has the double advantage of avoiding the saturation of the DAC by high frequency

noise, and to allow the extraction of the DAC noise by looking at frequencies above the filter cut-off frequency. In Fig. 4.6, a single time trace

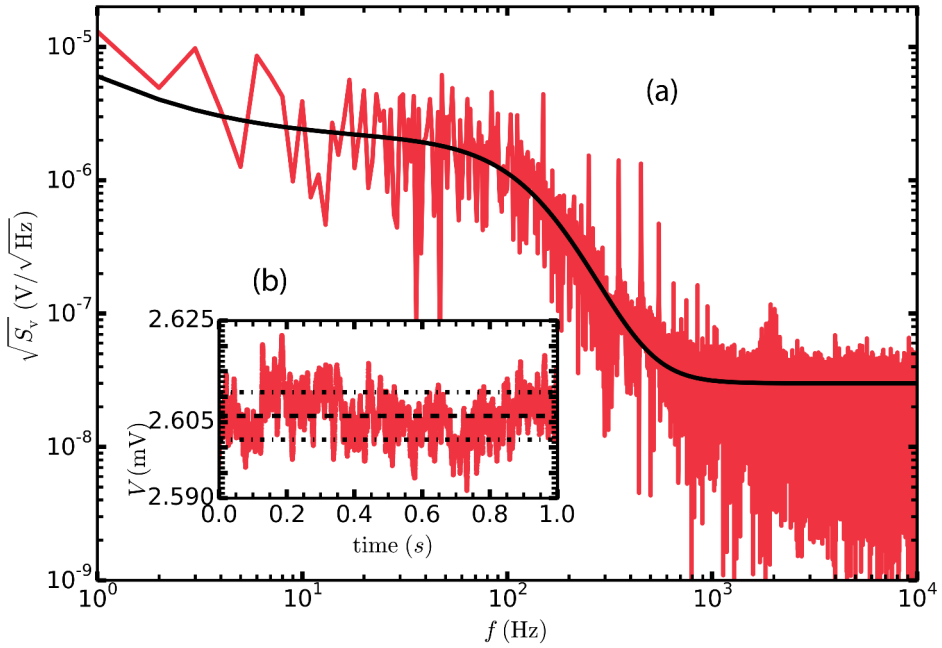

Figure 4.6. Illustration of a voltage sampling followed by numerical treatment. (a) Fast Fourier Transform of the signal. The cut-off around 100 Hz is corresponding to the time constant of the Lock-In amplifier. The peaks visible are multiples of 50 Hz, picked-up from the power lines of electronic equipment. The black line is the model described by Eq. (4.2), giving in this case $n_f = 2\ \mu\text{V}/\sqrt{\text{Hz}}$. (b) Raw data, before the FFT. The dashed line is the average value while the dashed-dot lines are the standard deviation.

has been acquired to generate the spectral density, leading to visible discrepancies from repeated acquisition of the same signal. A simple way to reduce the discrepancies is by averaging the FFT's. One can do so by repeating the measurement, by splitting the original time trace into N sub-intervals [thus reducing the frequency range to $[N/T, f_{\text{acq}}/2]$ (see [166])], or by artificially down-sampling the data into N traces (then the range becomes $[1/T, f_{\text{acq}}/2N]$).

Electric hum pick-up is a problem when using a DAC. Analog to digital conversion takes place in a data acquisition card installed in a computer, the latter saving the acquired data into a disk. This setup is connecting directly the ground of the experiment to the ground of the computer, increasing the pick-up of 50 Hz noise. This shows up on the frequency spectrum as a clear peak at 50 Hz, followed by all possible harmonics with decreasing amplitudes. Those peaks emerge from the background of Fig. 4.6. The easiest way of removing such noise is to insert an opto-isolator between the amplifier and the DAC.

The noise floor extraction is performed by fitting the FFT of the acquired signal. We are using a phenomenological model taking into account the measurement chain:

$$\sqrt{S_{\mathrm{v}}(\omega)} = \left(n_{\mathrm{f}} + b/\omega\right)\left[\frac{1}{1+(\omega\tau)^2}\right]^n + r\,. \tag{4.2}$$

The first term between parenthesis is the noise n_{f} of the signal with an extra $1/f$ noise component (b being a fitting parameter). The signal is then filtered by the lock-in amplifier, with a n^{th}-order low pass filter of time constant τ (the expression in the square brackets). The last term r account for the noise floor of the DAC itself. We consider the noise n_{f} to be frequency independent (i.e. white) in the range of frequencies $\omega_{\mathrm{drive}} \pm 1/\tau$ we are interested in. This noise is directly entering the definition of the NET as an independent source as described in chapter 2.7

$$\mathrm{NET} = \sqrt{S_T + \frac{S_{\mathrm{v}}}{\left(\partial V/\partial T\right)^2}} = \sqrt{S_T + \mathrm{NET}_{\mathrm{amp}}^2}\,, \tag{4.3}$$

where $\partial V/\partial T$ is the responsivity of the thermometer. When the sensor is resistive, i.e. $R(T)$ is the varying parameter, the readout noise is defined by $\mathrm{NET}_{\mathrm{amp}} = n_{\mathrm{f}}/(I_{\mathrm{bias}}\,\partial R/\partial T)$. I_{bias} can be either a DC current, or the amplitude of a sinusoidal signal. Hence $\mathrm{NET}_{\mathrm{amp}}$ is reduced by increasing I_{bias}, while a thermometer limited by temperature fluctuations has a constant NET$= \sqrt{S_T}$ (Ch. 2.7). Measuring a thermometer NET allows one to determine whether the noise of this thermometer originates from the fluctuation of its temperature or from its readout electronic.

5. Zero bias slope thermometry

This chapter is dedicated to measurements of temperature on two different kinds of islands. The first one is a normal conducting metal island for which we used quasiparticle NIS thermometers and Andreev current thermometers. The second island was made of titanium, for which we develop a thermometer based on the measurement of the zero bias slope of the *I-V* characteristics. The corresponding theory is described in the second chapter. To start with, let us recall the main results of the first chapter in order to define the figure of merit of a thermometer.

5.1 Figure of Merit

We aim to measure the temperature fluctuations of a free electron gas. This was described in the first chapter and the main result was the estimation of the temperature fluctuation spectrum

$$S_{\mathrm{T}} = \frac{2k_{\mathrm{B}}T^2}{G_{\mathrm{th},\Sigma}} \frac{1}{1+(\omega\tau)^2} \,, \tag{2.8}$$

where $G_{\mathrm{th},\Sigma} \approx G_{\mathrm{th,e\text{-}ph}}$ at best. Electron-Phonon (e-ph) coupling has been derived in Ch. 2, and reads $G_{\mathrm{th,e\text{-}ph}} = 5\Sigma\mathcal{V}T^4$ in a normal metal, where Σ is a material constant and $\mathcal{V}$ is the volume. The review [122] tells that Σ varies from 0.3 to $2.4 \times 10^{-9}\ \mathrm{Wm^{-3}K^{-5}}$ for usual metals, the lowest value is for aluminium and the highest is for gold. Experimentally, one can tune the strength of the electron-phonon coupling (hence the temperature fluctuation spectrum) by either varying the volume of the sample or by changing the electronic temperature.

To record the temperature fluctuations, few requirements emerge from Eq. (2.8).

The heat conductances have to be small enough to decouple the electron gas from the bath sufficiently. Superconducting tunnel junctions exhibit good thermal isolation as the high resistance prohibits tunneling events effectively, especially at low bias voltage. Nevertheless, as soon as any current is flowing, heat is transported, and one has to consider the quantity $\frac{\partial \dot{Q}_{\mathrm{J}}}{\partial T}(V, T, T_{\mathrm{bath}})$ and compare it with the limit set by electron-phonon heat conductance $G_{\mathrm{th,e\text{-}ph}}$. Recalling the result of chapter 3.4, we can already remark that $\frac{\partial \dot{Q}_{\mathrm{J}}}{\partial T}$ is minimum for $V = 0$. In this limit the heat conductance is dominated by the electron-phonon coupling. This is motivating the study of zero bias thermometers at low temperatures.

The sensitivity to be achieved is set by the zero frequency limit $S_{\mathrm{T}}(0)$ of Eq. (2.8). If the heat conductance is dominated by electron-phonon coupling, Noise Equivalent Temperature of the amplifier (NET_{amp}, see Ch. 4.3.4) of the thermometer has to be lower than $\sqrt{\frac{2k_{\mathrm{B}}}{5\Sigma\mathcal{V}T^2}}$. The lower the temperature, the larger is the amplitude of temperature fluctuations. When the NET is reaching this limit, the thermometer is said to reach the thermodynamic limit, as the temperature fluctuations define in this case the lowest achievable NET [167]. Reducing the volume is also increasing the amplitude of the zero-frequency fluctuations. The total NET (incl. the phonon noise) is given by

$$\mathrm{NET} = \sqrt{\frac{2k_{\mathrm{B}}T^2}{G_{\mathrm{th},\Sigma}} + \left(\frac{n_{\mathrm{f}}}{I_{\mathrm{bias}}\,\partial R/\partial T}\right)^2} \tag{5.1}$$

where n_{f} is the amplifier noise described in Sec. 4.3.3.

The bandwidth of the thermometer has to be larger than the cut-off frequency $\omega_{\mathrm{c}} = 5\Sigma T^3/\gamma_{\mathrm{T}} \equiv 1/\tau_{\mathrm{e\text{-}ph}}$ when $G_{\mathrm{th},\Sigma} \sim G_{\mathrm{th,e\text{-}ph}}$. It is worth noting that the electron-phonon relaxation time $\tau_{\mathrm{e\text{-}ph}}$ is independent of the volume considered, unlike $S_{\mathrm{T}}(0)$.

In conclusion and with respect to these criteria, a good thermometer to reach the temperature fluctuation limit should be sensitive at low temperatures (ideally below 100 mK) and should have as little back action as possible, so that the heat conductance is dominated by the electron-phonon coupling. In the following, we will address few attempts to realize such a thermometer, based on NIS or SIS' tunnel junctions, and focus on their properties near zero bias. The choice of using a tunnel junction is motivated by the fact the heat conductance can be further suppressed, compared to a clean NS contact.

5.2 Model of the zero bias conductance of a hybrid tunnel junction device

We will consider two junctions in series, forming a SINIS or SIS'IS structure. We will suppose that both junctions are independent and have the same normal state resistance R_{T}. Under these assumptions the applied voltage is split equally between the junctions and $I_{\mathrm{SINIS}}(V) = I_{\mathrm{NIS}}(V/2)$.

In chapter 2, the different contributions to the total current have been derived. To summarize, the current through a tunnel junction is a sum of quasiparticle current (due to regular tunneling, or Andreev reflection) and Josephson current. All these contributions appear in the following equation, which gives the conductance at zero applied voltage bias as

$$G_0(T) = \left[\frac{1}{R_{\mathrm{T}}}\left(\gamma + \sqrt{\frac{2\pi\Delta_{\mathrm{S}}}{k_{\mathrm{B}}T}}\exp^{-\Delta_{\mathrm{S}}/k_{\mathrm{B}}T}\right) + \frac{eI_{\mathrm{N}}^{A}}{2k_{\mathrm{B}}T}\right] I_0^2\left(\frac{\hbar I_{\mathrm{C}}(T)}{2ek_{\mathrm{B}}T}\right) . \quad (5.2)$$

This model of zero bias conductance covers all the measured devices, in which the charging energy can be neglected. It takes several phenomenological parameters, which can usually be extracted in different ways as explained below.

The normal state resistance R_{T} is measured at a temperature above the aluminium transition temperature (1.3 K), by fitting the *I-V* characteristics with a linear model: $V = R_{\mathrm{T}}I$.

The effective γ parameter is introduced to account for all the sub-gap leakage. Usually, this parameter is extracted from a measurement of the conductance at the lowest achievable temperature. When the value of γ is too low to be measured with a usual ammeter, one can use a Single Electron Transistor (SET) to monitor every sub-gap event [162]. The γ parameter is usually seen as a figure of merit of the junction quality, as it closely relates to the error rates of the devices (SET, single electron pump) based on them [168].

The zero temperature superconducting gap $\Delta_{\mathrm{S},0}$, appearing in the temperature dependent gap Δ_{S}, can be extracted in two ways. First by fitting the SINIS *I-V* characteristics using Eq. (3.3) for the current. Due to the heat flows at finite voltage, the normal metal island might be strongly cooled or heated, and this needs to be taken into account in the fitting

process [169, 170]. Thus, this approach has to be combined with the computation of the heat balance equation to extract the electronic temperature [169, 171]. The second way of determining $\Delta_{S,0}$ is to use the Eq. (5.2) to fit the zero bias slope, for which thermal effects can be neglected, at temperatures where the quasiparticle conductance dominates.

The disorder-enhanced Andreev current I_N^A is also considered as a parameter. It can be theoretically estimated for a large and uniform junction using Eq. (3.20): $I_N^A = \pi\hbar/e^3\nu_N\mathcal{A}t_N R_T^2$. Nevertheless the value extracted by fitting the step at zero bias in the *I-V* characteristics might deviate from this theoretical value [114, 172]. The barrier inhomogeneity, like the variation of its thickness, has been proposed as a probable reason for this discrepancy [92, 110].

The critical current $I_C(T)$ is known thanks to the Ambegaokar-Baratoff (AB) formula, which take the gap of the weaker superconductor $\Delta_{S',0}$ as a parameter (in addition to R_T and $\Delta_{S,0}$ which are supposed to be already known from a fit above the transition temperature $T_{C_{S'}}$). Equation (5.2) is only valid for an overdamped junction, in the limit of small McCumber parameter, $2eI_C RC/\hbar \ll 1$. In this limit the critical current can be extracted directly from the *I-V* characteristics without requiring specific switching measurement (see chapter 5.4.1).

A spurious heat flow $\dot{Q}_0$ is added to the list of the five previous parameters to account for the electronic temperature saturation observed experimentally. The system temperature T is then given by a simplified heat balance equation $\dot{Q}_0 = \Sigma\mathcal{V}(T^5 - T_{bath}^5)$ where we have neglected all heat conductances but the electron-phonon coupling.

The multiple parameters entering this model allow it to be valid over a broad range of devices which exhibit different behaviors. Few restrictions apply however: the charging energy is neglected; the Thouless energy is negligible; the junctions are overdamped in the temperature range we are interested in.

5.3 SINIS measurement

In a SINIS structure the central island is made of a normal metal, usually copper [122], and connected to superconducting leads through

tunnel junctions. The superconducting gap, acting as an energy filter, provides the necessary thermal isolation of the island. We will present the results of two different thermometers, the first one based on quasiparticle current and the second one based on the magnitude of the zero bias Andreev current.

5.3.1 Quasiparticle thermometer

First we ignore Andreev current and set $I_{\mathrm{N}}^{A} = 0$. We further assume a SINIS structure with $\Delta_{\mathrm{S}',0} = 0$ in the model of zero bias conductance [Eq. (5.2)]. In the case where the γ parameter is strictly vanishing, one could expect infinite responsivity as the conductance is vanishing like $\mathrm{e}^{-\Delta_{\mathrm{S}}/k_{\mathrm{B}}T}$. Experimentally, the γ parameter is finite and the zero bias responsivity eventually vanishes as the conductance saturates to γ/R_{T}. The responsivity can be simplified depending on whether the zero bias resistance is saturating due to the γ parameter or not

$$\left.\frac{\partial R}{\partial T}\right|_{0} = \begin{cases} -\frac{R_{\mathrm{T}}}{T}\sqrt{\frac{\Delta}{2\pi T}}\mathrm{e}^{\Delta/k_{\mathrm{B}}T} & (T > T_0) \\ -\frac{R_{\mathrm{T}}\sqrt{2\pi}}{T\gamma^2}\left(\frac{\Delta}{k_{\mathrm{B}}T}\right)^{3/2}\mathrm{e}^{-\Delta/k_{\mathrm{B}}T} & (T < T_0, R/R_{\mathrm{T}} \sim 1/\gamma)\,. \end{cases} \tag{5.3}$$

The cross-over temperature between the two regimes is given by $T_0 = \Delta/k_{\mathrm{B}}[\ln(\sqrt{2\pi\Delta/k_{\mathrm{B}}T_0}) - \ln(\gamma)] \sim \Delta/k_{\mathrm{B}}\ln(1/\gamma)$ for small γ. The γ parameter can reach a value as low as 1.2×10^{-7}, obtained in highly resistive junctions [162]. If the junction resistance is low, the Andreev current is setting the lower bound of the parameter γ, as can be seen from Eq. (3.12).

In a typical SINIS device presented in Fig. 5.1, with the junction area $\mathcal{A} = 0.1\ \mu\mathrm{m}^2$ and the normal state resistance $R_{\mathrm{N}} = 8\ \mathrm{k}\Omega$, the usual Andreev tunneling sets $\gamma > 3.22 \times 10^{-5}$. If one includes in addition the disorder-enhanced Andreev reflection in the 25 nm thin aluminium leads, the γ parameter is theoretically larger than $\gamma > 1.34 \times 10^{-4}$. The value extracted from the fit, $\gamma = 2.17 \times 10^{-4}$, is in good agreement with this theoretical prediction, and is limiting the responsivity at temperatures below 200 mK. For this particular device, the responsivity is found to be -720 MΩ/K at 200 mK, leading to a NET estimated to be 1 $\mu\mathrm{K}/\sqrt{\mathrm{Hz}}$ (with $I_{\mathrm{bias}} = 5$ pA leading to $G_{\mathrm{th,J}} = G_{\mathrm{th,e\text{-}ph}}/10$ and $n_{\mathrm{f}} = 1$ nV/$\sqrt{\mathrm{Hz}}$). This value is close to the expected magnitude of the temperature fluctuations at zero frequency, $\sqrt{S_{\mathrm{T}}} \approx 0.5\ \mu\mathrm{K}/\sqrt{\mathrm{Hz}}$ for the given volume $\mathcal{V} = 0.18\ \mu\mathrm{m}^3$ of the normal island. The bandwidth of the temperature fluctuations is expected to be around 160 kHz while the impedance of the SINIS structure is lim-

iting the measurement bandwidth to 1 kHz at best, because of the line capacitance.

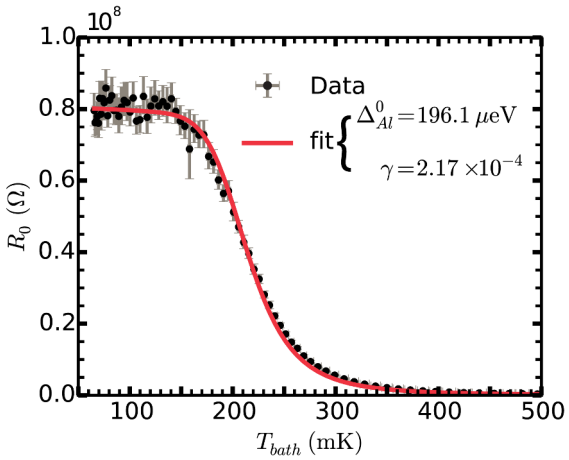

Figure 5.1. Zero bias resistance of a SINIS device. The zero bias resistance is extracted from a low bias fit of the voltage biased *I-V* characteristics. The error bars are the 95 % confidence interval of the linear fit in the range from -2 to 2 pA. At a low temperature, the resistance increases and the current is reduced. Thus, the signal-to-noise ratio is decreasing when the temperature is lowered, leading to visible error bars at low temperatures.

Increasing the normal state resistance gives two benefits, which directly follow from Eq. (5.3). First the sensitivity is increased. Second, the γ parameter is expected to be smaller as the Andreev tunneling is suppressed, and thus the thermometer will still saturate, but at a lower temperature ($T_0 \approx 165$ mK for $\gamma = 1 \times 10^{-6}$) [173]. Unfortunately, increasing R_T does have a major drawback: the bandwidth is reduced, especially in the sub-gap region where the conductance is small. Embedding a NIS thermometer in a resonant circuit [157] demonstrates better performance, as the bandwidth reaches 10 MHz, without sacrificing much of the NET of the device: $90\ \mu\mathrm{K}/\sqrt{\mathrm{Hz}}$ (only 25 times higher than the thermodynamic limit set by the temperature fluctuations). The sample design resembles the attempt realizing a NIS micro-bolometer [22]. The detailed noise derivation can be found in [23], showing that an optimal resistance exists as a trade off between heat isolation (large R_T) and small shot noise (R_T small). Embedding such a NIS tunnel junction in a resonant circuit [174] allows overcoming the limited bandwidth, usually at the cost of a reduced sensitivity. Nevertheless, further measurements performed within the PICO group [175] demonstrate a thermometer with NET around $10\ \mu\mathrm{K}/\sqrt{\mathrm{Hz}}$, reported as a star in Fig 6.1. Precisely the same thermometer performing with the same sensitivity at around 40 mK would be enough to record the full spectrum of the temperature

fluctuations. The microbolometer based on it would be able to measure a single GHz photon [158].

In conclusion, operating a quasi-particle thermometer near zero bias has the double advantage of reducing shot noise, as the current is kept low, and to provide a better heat isolation. The wide temperature range of such a device is limited only by the junction leakage.

5.3.2 Disorder-enhanced Andreev thermometer

Disorder-enhanced Andreev current offers another alternative for thermometry, providing a positive responsivity at temperatures lower than T_0, i.e. when the quasiparticle conduction is saturated or equivalently when $G_0(T) \approx \gamma/R_\mathrm{T} + eI_\mathrm{N}^A/2k_\mathrm{B}T$. One can define T_1 as the temperature where the disorder-enhanced Andreev current is dominating the conductance. Under the previous assumption, it reads $T_1 \sim eI_\mathrm{N}^A R_\mathrm{T}/2k_\mathrm{B}\gamma < T_0$. One can already remark that the previous inequality does not always hold. A cross-over between the disorder-enhanced Andreev current and the quasiparticle current can happen at a temperature above T_0. It is the case presented in Fig. 5.2, where the resistance first increases, as the quasiparticle conductance is exponentially suppressed. Then, the resistance decreases again below the temperature[1] $k_\mathrm{B}T_1 \sim \Delta/\ln(\Delta/eI_\mathrm{N}^A R_\mathrm{T})$. The responsivity on the linear slope is positive, and reads

$$\frac{\partial R_0}{\partial T} = \frac{2k_\mathrm{B}}{eI_\mathrm{N}^A}\,. \tag{5.4}$$

It remains constant over a wide range of temperatures, up to the effective Thouless energy E_Th of the device. For a typical sample, the Thouless energy is of the order of a few mK, as in Publication III. Below this temperature the conductance is saturating again, and the responsivity vanishes. This phenomenon is also called re-entrance effect, and it has been predicted in the context of a NIS junction theoretically [176] and measured subsequently [177]. Hence, the working temperatures of a disorder-enhanced Andreev thermometer are in the range from T_1 to $E_\mathrm{Th}/k_\mathrm{B}$.

In our experiments, we were not able to reach this lower bound as the electronic temperature saturates at around 120 mK when cooling the bath below this temperature. This can be seen in Fig. 5.2 were an external heat

[1] We assumed $\Delta/eI_\mathrm{N}^A R_\mathrm{T} \ll \sqrt{2\pi k_\mathrm{B}T_1/\Delta}$ to simplify the given expression of T_1.

load of $\dot{Q}_0$ has to be introduced into the heat balance equation to capture the experimental results (blue line). From the parameters of this device, namely $R_\mathrm{T} = 620\,\Omega$/ junction, $\Delta_{\mathrm{Al},0} = 225\,\mu\mathrm{eV}$, $\gamma = 3.2 \times 10^{-4}$ and $I_\mathrm{N}^A = 140$ pA, one can expect $T_1 \approx 330$ mK which is in good agreement with the maximum of conductance observed in Fig. 5.2. The value of $\gamma = 3.2 \times 10^{-4}$ extracted from the fit can be related to the disorder-enhanced Andreev reflection in the superconducting electrode, given by Eq. (3.19): $\gamma_\mathrm{AS} \approx 3.9 \times 10^{-4}$ for this device.

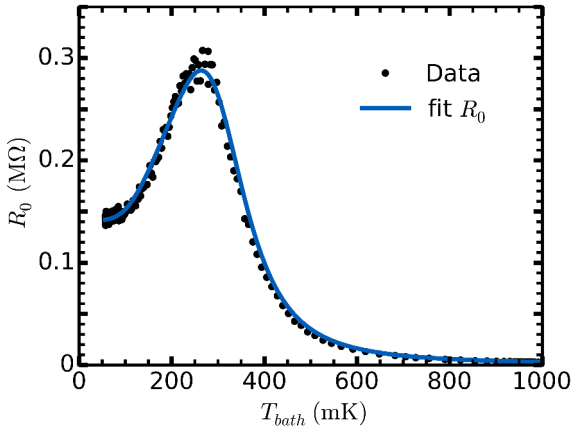

Figure 5.2. Zero bias resistance of a SINIS device which exhibits strong disorder-enhanced Andreev current. The non-monotonic shape of the zero bias resistance is also called re-entrance effect. The saturation at low temperature is modeled as a spurious heat load. The parameters entering the model of Eq. (5.2) are given in the text.

Because of the constant responsivity $\partial R_0/\partial T = 2k_\mathrm{B}/eI_\mathrm{N}^A$, the NET is temperature independent and reads NET $\approx 3\ \mu K/\sqrt{\mathrm{Hz}}$. In this regime, a thermometer based on Andreev current of ~ 100 pA should reach the limit set by the phonon noise at temperatures around 80 mK. On the other hand, such a device is extremely sensitive to any external heat load both because of the low electron temperature and the small volume. In order for the device depicted in Fig. 5.2 to reach an electronic temperature below 80 mK, one has to reduce the external heat load to below 100 aW, which is however realistic.

In Publication III, we demonstrated a constant responsivity down to 85 mK. The main difference between the device presented here and the device presented in Publication III, explaining the lower saturation temperature, is the different volume. Common for these two devices is an engineered normal metal island, where copper has been replaced with a multilayer sandwich of titanium and gold. An additional thin aluminium buffer layer ensures a good junction quality. The multilayer structure is expected to enhance the interference in the normal side of the junction,

but a systematic study would be required to make definite statements. In this last sample, where $I_{\mathrm{N}}^{A} = 37.5$ pA, the NET is estimated to be $20\ \mu\mathrm{K}/\sqrt{\mathrm{Hz}}$, which is still 10 times higher than the limit set by the temperature fluctuations at 100 mK. The maximum voltage responsivity is achieved for a current drive amplitude I_{N}^{A}, and is then only a function of fundamental constants $\partial V/\partial T_{\max} = 2k_{\mathrm{B}}/e \approx 172\ \mu\mathrm{V/K}$. Hence, the only possible optimization of such a device would be to decrease the electron-phonon coupling either by reducing the island volume or the working temperature. We have been limited by an external heat load to electronic temperatures saturating at about 85 mK. Using this kind of a thermometer would nevertheless be a step forward toward a non-invasive electronic thermometer for low temperatures.

5.4 SIS'IS

Substituting the normal metal N by a superconductor S' should enhance the temperature fluctuations as the electron-phonon coupling is reduced by a factor $\mathrm{e}^{-\Delta_{\mathrm{S}'}/k_{\mathrm{B}}T}$ at low temperatures, provided that the junction is still isolating the superconducting island form the external environment. The energy resolution $\delta E = \sqrt{2k_{\mathrm{B}}T^2\mathcal{C}}$ of a calorimeter is also improving as the heat capacity $\mathcal{C}$ of the absorber is decreased by the same amount (ch. 3.5). The temperature of such an island is defined by the quasiparticle occupation function, thus we request the central island S' to be in quasi-equilibrium. In the following sections, we will describe zero bias slope thermometry of such a junction.

5.4.1 SIS'IS cooling

One question regarding Eq. (3.26) which governs the phase of a SIS' junction within the RCSJ model is as follows: is the zero bias slope thermometer measuring the electronic temperature T or the temperature of its immediate physical environment? The saturation of the zero bias slope, observed when the bath temperature is lowered, gives a hint as it suggests that the zero bias slope saturates the same way as the electronic temperature. One may still wonder whether the temperature of the environment, modeled by the shunt resistance R_{s}, saturates as well. In order to conclude between these possibilities, we conceived a device

where a central titanium island is contacted with two sets of junctions [121], allowing us to tune locally the electronic temperature of the island only [see Fig. 5.3 (b)]. The first set of junctions is resistive enough and thus $E_J \lll k_B T$ so that the current is dominated by the quasiparticles. Hence, strong cooling (or heating) is expected when a current is passed trough these junctions. The other set is formed by large junctions, which have low impedance and thus can carry a large supercurrent. We are using them as a thermometer. Experimentally, a current of I_{cool} is applied across the cooling junctions, while the *I-V* characteristics of the large junctions are measured. The circuits are isolated from each other.

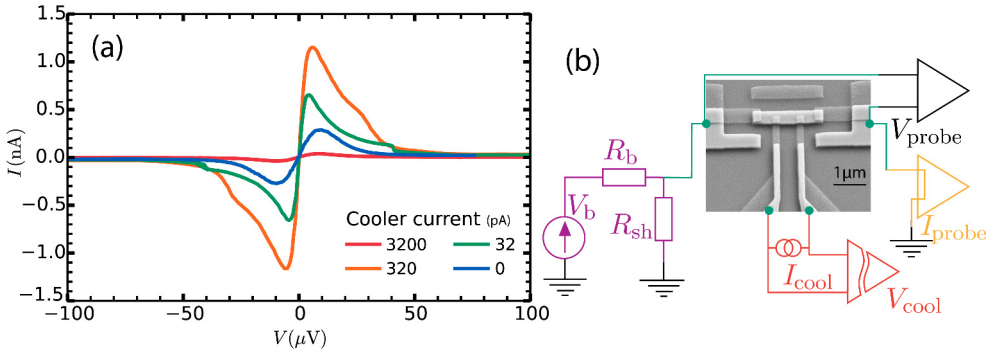

Figure 5.3. Effect of the electronic temperature on the supercurrent peak. (a) *I-V* characteristics for few different currents applied on the cooling junctions. Optimal cooling is found experimentally around 350 pA. (b) Scheme of the measurement circuit. The probe junctions are voltage biased at room temperature (in violet). The *I-V* characteristics of the cooler are also measured, with the help of an opto-isolator (depicted as a red broken triangle).

Fig. 5.3 presents the measurement scheme [Fig. 5.3 (b)] along with the resulting *I-V* characteristics for four cooling currents [Fig. 5.3 (a)]. The Ambegaokar-Baratoff formula predicted the maximum of the supercurrent peak to be $I_{C,0} \approx 17$ nA for this device. Thus, we expect the junction to be overdamped, as $\beta_c = 0.025$. With $T_{bath} = 60$ mK, the switching mechanism is expected to be mainly thermal [178, 179], and the maximum of the supercurrent peak is smaller than its zero temperature prediction. The amount this maximum current is reduced from the critical current depends on the frequency dependence of the environment, in addition to the junction characteristics [131].

For this reason our analysis is only qualitative, but the influence of the cooling current is clearly standing out as seen in Fig. 5.3 (a). The larger maximum current is obtained when the coolers are biased near their optimum working point at 320 pA. In addition, the zero bias slope gets steeper as predicted by the model of phase diffusion [131]. If a large

current is applied through the coolers, they overheat the island strongly, and this explains why the supercurrent peak almost vanishes in the red curve. With this measurement, we proved that a thermometer based on the supercurrent slope is indeed measuring the electronic temperature of the titanium island [124].

5.4.2 Titanium transition edge sensor

Starting from the first measurements, the fabrication has been optimized to increase the ratio $E_{\mathrm{J}}/k_{\mathrm{B}}T_{\mathrm{C}}$, both by increasing the transparency of the junctions and by improving the material quality. Titanium films with their T_{C} around the bulk value have been successfully and reproducibly fabricated by increasing the deposition rate and carefully cleaning the deposition chamber. In the device whose zero bias slope is plotted in Fig. 5.4, the normal state resistance is around 300 Ω per junction and $\Delta_{\mathrm{Ti},0} \approx 60\ \mu\mathrm{eV}$. The switching current around 300 nA leads to $E_{\mathrm{J}}/k_{\mathrm{B}}T_{\mathrm{C}} \sim 25$. In this case the zero bias resistance vanishes quickly as the gap Δ_{Ti} develops. In this sense, our device is very similar to a Transition Edge Sensor (TES) described in [12]. In the case of SIS', the resistance is varying over a much larger scale compared to a traditional TES. Instead of varying from zero to the normal state resistance of the film (a few ohms), the resistance of a SIS'-TES spans a few decades up to the zero bias quasiparticle resistance, and this is enhancing greatly the temperature responsivity.

The zero bias resistance is usually measured in a phase locked manner, described in the experimental methods (Ch. 4.3). The AC amplitude of the biasing current is kept constant, and the frequency ranges from Hz to few kHz, limited only by the line impedance. The bath temperature can be controlled by means of a resistive heater anchored on the sample stage, while monitoring the zero bias slope. The fact that a finite amplitude is used leads to a smearing of the R(T) response curve when the switching current becomes comparable to the biasing current, as can be seen in Fig. 5.4 (a).

To estimate the switching current, a full *I-V* characteristics are acquired for each bath temperature. The result is depicted in Fig 5.4 (b) along with a fit making use of the Ambegaokar-Baratoff formula of Eq. (3.24). The resistance extracted this way is larger than the normal state

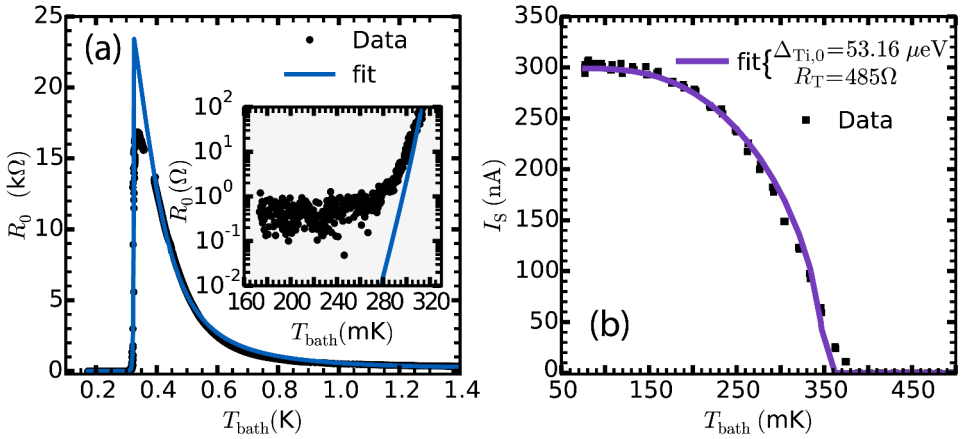

Figure 5.4. Titanium transition edge sensor. (a) The zero bias resistance is extracted from an AC current biased measurement, with a phase-locked voltage measurement. The smearing near T_{C} is a consequence of the finite AC drive amplitude. The fit (solid blue line) is using Eq. (5.2) setting $I_{\mathrm{N}}^{A} = 0, \dot{Q}_0 = 0$. The inset emphasizes the saturation of the zero bias slope, while the model demonstrates decay exponentially towards zero. (b) With the same sample, the *I-V* characteristics are measured as a function of the bath temperature, from which the switching current can be extracted. The fit (solid violet line) uses the Ambegaokar-Baratoff formula, Eq. (3.24).

resistance of the device by a factor of ~ 60. This effect, a critical current reduction at all temperatures, has been observed in various other experiments involving small SIS tunnel junctions and is a direct consequence of the influence of the environment on the dynamics of the Josephson junction [180].

The device responsivity can be extracted by a numerical derivation of the $R_0(T)$ characteristic. We used the responsivity extracted this way to compute the NET. As we are using the supercurrent slope as a thermometer, the maximum amplitude is limited by the switching current of the weaker one of the two junctions. Exceeding this limit leads to a strong overheating of the SIS' junction. The NET in this device was estimated to be around $2\ \mu\mathrm{K}/\sqrt{\mathrm{Hz}}$ at 330 mK in Publication II.

One way to reduce the gap between the thermometer NET and the temperature fluctuation noise is to reduce the temperature at which the thermometer is operated. The inset of Fig. 5.4 (a) demonstrates the saturation of the measurement for impedances below a few Ω. As a matter of fact, this saturation is restricting the operating range to temperatures above 250 mK. The next section has the goal to extend this temperature range by allowing low noise measurements of devices having impedances below one Ω.

5.4.3 Low impedance measurement

TES resistances usually range from vanishing resistance to a few Ω and their readout electronics is a mature technology. In order to measure a TES impedance using heavily shielded and thus resistive lines, it is practical to use a shunt resistor close to the device to voltage bias it at a low temperature and to employ a Superconducting QUantum Interference Device (SQUID) to measure the current [12]. A SQUID amplifier can be seen as a magnetometer monitoring the magnetic field generated by the current flowing into the input coil. A SQUID is formed by a superconducting loop, interrupted by two Josephson junctions. By measuring the critical current across the device, one can extract the phase difference between the two superconducting branches, this difference itself is proportional to the magnetic flux enclosed inside the loop. A SQUIPT (Superconducting QUantum Interference Proximity Transistor) [181–183] works on the same principle, but does have a few advantages over a SQUID, especially its low power dissipation. Furthermore it is a high impedance device matching well with the noise impedance of our amplifier. For these reasons, we developed a SQUIPT amplifier, merging an on-chip superconducting input coil and a SQUIPT. The noise of such a SQUIPT transducer has not been measured yet, and all attempts so far were limited by the noise of the voltage pre-amplifier [183, 184].

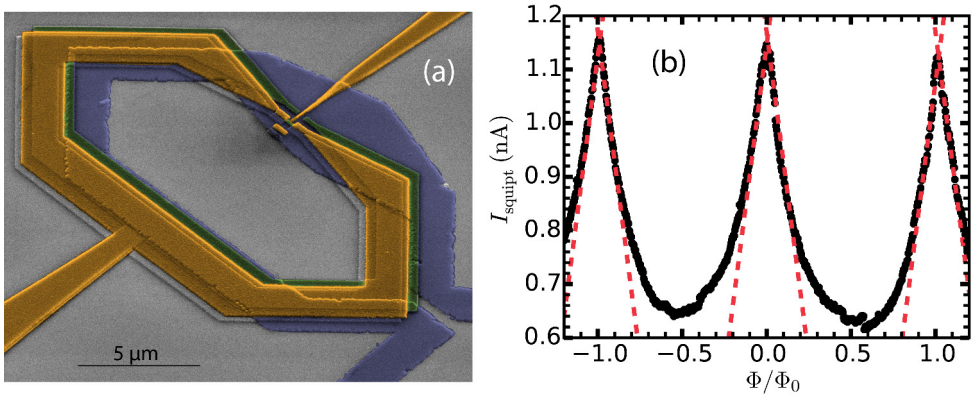

Figure 5.5. SQUIPT amplifier. (a) False color SEM of a SQUIPT device (in orange), on top of an aluminium input coil (in blue) protected by a 50 nm thick aluminium oxide layer. The coil and the SQUIPT are overlapping to concentrate the flux generated by the coil into the pick-up area of the SQUIPT. (b) Measured current response of a SQUIPT as a function of the applied magnetic flux. Dashed lines are guides to the eye, representing the linear response of the SQUIPT transducer with responsivity of 2.42 nA/Φ_0.

The SQUIPT responsivity is extracted from the measurement of its

response to an external magnetic field [Fig. 5.5 (b)], and reads 2.42 nA/Φ_0 at maximum, where $\Phi_0 = h/2e$ is the flux quantum. The input coil is calibrated and its transfer function is $6.25 \times 10^{-6}\ \Phi_0/\mathrm{nA}$. The total "gain" of the transducer, $I_{\mathrm{in}}/I_{\mathrm{out}}$ is approximately 2.0×10^{-5}. Thus, one can calculate the expected noise of the SQUIPT + amplifier chain, expressed as an equivalent input noise $i_{\mathrm{n}} \sim 0.5\ \mathrm{nA}/\sqrt{\mathrm{Hz}}$, assuming the current amplifier spectral noise density to be around $10\ \mathrm{fA}/\sqrt{\mathrm{Hz}}$.

A 0.3 Ω shunt resistor R_{sh} made out of 0.5 cm of $\varnothing 100\ \mu\mathrm{m}$ manganin wire is shunting the junction at base temperature [see Fig. 5.6 (b)]. The value is chosen as a trade-off between the expected sample impedance of a few Ω and the voltage bias range which is limited so that the dissipation $\frac{R_{\mathrm{lines}}}{R_{\mathrm{sh}}^2} V_{\mathrm{max}}^2$ is much smaller than the cooling power of the dilution refrigerator. By recording the bath temperature while biasing the sample we estimated $V_{\mathrm{max}} \simeq 10\mu\mathrm{V}$.

The circuit schematic is depicted in Fig. 5.6 (b). The device and the shunt resistor can be seen as two parallel resistances [Fig. 5.6 (c)], and the various terminals allow one to choose in which branch the current is measured. Terminal B is used to bias the sample using a current I_{bias}. Depending on which terminal is used as a return path for the biasing current, the SQUIPT measures either the current flowing in the sample branch (A and G grounded) or in the shunt resistor branch (D grounded). The device is effectively current biased if its impedance is larger than the shunt resistor, and the biasing voltage is then measured with a voltage amplifier connected to the terminals C and D. D can also be used in combination with G to measure the transfer function of the input coil. The extra terminals H and I, left open for most of the measurements, allow to locally tune the electronic temperature of the island without affecting the SQUIPT, measured trough terminals E and F. An external coil allows one to apply a constant flux bias across the SQUIPT to tune it to its most sensitive point.

A slowly varying AC signal has been superimposed to the DC bias current I_{bias} to increase the readout sensitivity. The measured voltage is the phase-locked signal, from which the resistance of R_{sh} in parallel with $R_{\mathrm{SIS'IS}}$ is extracted. The DC bias voltage is then computed from the measured parallel resistance and the known DC biasing current. The result [depicted in Fig. 5.6 (a)] indicates that $R_{\mathrm{sh}} > R_{\mathrm{SIS'IS}}$. Nevertheless, one can extract $R_{\mathrm{SIS'IS}}$, the setup working then as a Wheatstone bridge, de-

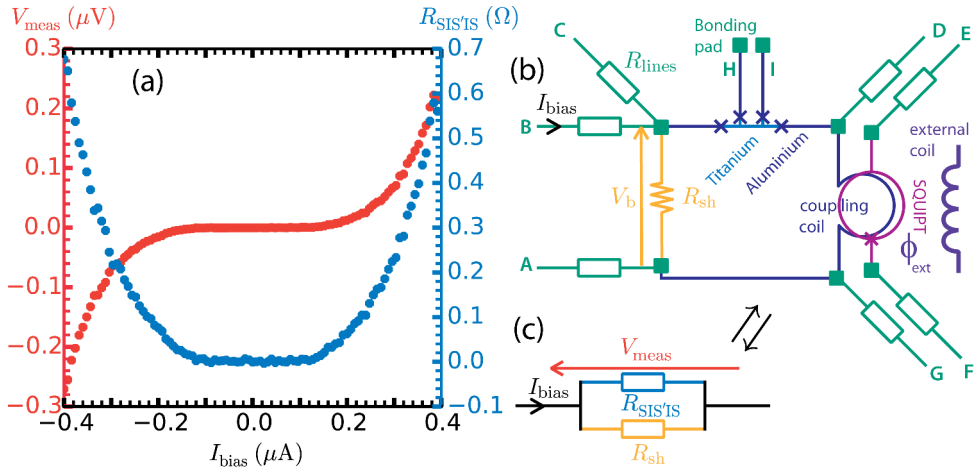

Figure 5.6. Low impedance measurement. (a) Measured voltage across the device (in red) and the corresponding extracted $R_{\mathrm{SIS'IS}}$ (in blue). (b) Scheme of the measurement wiring involving a SQUIPT transducer, detailed in the text. (c) Equivalent circuit at low frequencies.

picted in Fig 5.6 (c). This allowed us to set the upper bound for $R_{\mathrm{SIS'IS}}$ to be around 0.3 mΩ at the lowest temperature. Note that the regular TES is biased using a few tens of μV, above the supercurrent peak. The impedance is then of the order of a few Ω, thus this scheme allows one to measure the impedance of TES but it is not suitable for zero bias thermometry using the supercurrent slope.

In the process, we noticed that having the input coil immediately below the SQUIPT leads to a visible capacitive coupling between the coil and the loop of the SQUIPT. In other words, the sinusoidal coil current is affecting the bias voltage in such a way that the phase of the signal is modified. This could be avoided easily with a better design of the input coil. The main disadvantage of a SQUIPT readout in this present measurement is the temperature dependence of the SQUIPT responsivity, which needs to be measured for all bath temperatures. Thus a SQUID –or SQUIPT– based measurement allows one to extend the zero bias slope measurements toward lower resistances, when $E_{\mathrm{J}} \gg k_{\mathrm{B}}T_{\mathrm{C}}$. We determined an upper bound for the zero bias resistance in that case, 0.3 mΩ, three orders of magnitude improvement in comparison to the direct measurement described in chapter 5.4.2.

5.4.4 Noise measurement

Here we will describe in details the Signal-to-Noise Ratio (SNR) measurement. The signal we are considering is the temperature fluctuation,

corresponding to the thermodynamic limit of a thermometer (described Ch. 2.7). The noise $\mathrm{NET}_{\mathrm{amp}}$ is due to the readout electronics (derived in Ch. 4.3.3). In the case where the total heat conductance is limited by the electron phonon coupling (i.e. $G_{\mathrm{th},\Sigma} \approx 5\Sigma\mathcal{V}T^4$), the SNR takes the simple form

$$\mathrm{SNR} = \sqrt{S_{\mathrm{T}}(0)}/\mathrm{NET}_{\mathrm{amp}} \approx \sqrt{\frac{2k_{\mathrm{B}}}{5\Sigma\mathcal{V}T^2}}\frac{I_{\mathrm{bias}}\partial R_0/\partial T}{n_{\mathrm{f}}} \,. \tag{5.5}$$

The first step is to measure precisely the responsivity $\partial R_0/\partial T$, by modulating the bath temperature near the transition point with a frequency of 10 mHz and with a typical amplitude of 1 mK [red dots in Fig. 5.7 (a)]. The response of the thermometer is recorded at the same time [blue dots in Fig. 5.7 (a)]. Responsivity values as high as 10 MΩ/K have been measured in various samples.

The second step is to extract the noise floor n_{f} of the setup. The FFT of the thermometer signal is computed [blue line in Fig. 5.7 (b)], and exhibits a peak at 10 mHz, which is scaled to correspond to the bath modulation amplitude. This way the FFT is properly scaled, and can be fitted with the model described by Eq. (4.2). Here n_{f} is the value of the fit at 10 mHz, and the error bars are given by the standard deviation of the FFT around n_{f} in the range [5 - 50] mHz. The process is repeated varying the drive amplitude. The measured noise is plotted in Fig. 4 of Publication II, and the best SNR in this study reads $\mathrm{SNR} \approx 0.2$. In Fig. 5.7 (c), we plotted the SNR for a device with volume $\mathcal{V} = 9.7 \times 10^{-3}\ \mu\mathrm{m}^3$. The expected zero frequency temperature fluctuation magnitude is $\sqrt{S_{\mathrm{T}}(0)} = 5.5\ \mu\mathrm{K}/\sqrt{\mathrm{Hz}}$. The responsivity has been measured to be $\partial R_0/\partial T = 0.65\ \mathrm{M\Omega/K}$. Hence the improvement of the SNR in this device is mainly due to the lower working temperature and the smaller island volume. This result is plotted as a yellow diamond in Fig. 6.1.

The maximal SNR of a TES near T_{C} described by Eq. (5.2) can also be calculated. One usually introduces the parameter $\alpha = d\ \ln R\ /\ d\ \ln T$ as a figure of merit of a transition edge sensor: α is of the order of 100 in a high quality transition edge sensor. The SNR of a SIS'-TES is given by

$$\mathrm{SNR}_{\mathrm{max}} \sim \alpha\frac{I_{\mathrm{C}}R_{\mathrm{T}}}{n_{\mathrm{f}}}\sqrt{\frac{k_{\mathrm{B}}^2}{5\pi\Delta_{\mathrm{S}}\Sigma\mathcal{V}T^3}}\ \mathrm{e}^{\Delta_{\mathrm{S}}/k_{\mathrm{B}}T} \,, \tag{5.6}$$

assuming that the conductance is dominated by the quasiparticles when the superconducting transition of the weaker superconductor S' occurs at

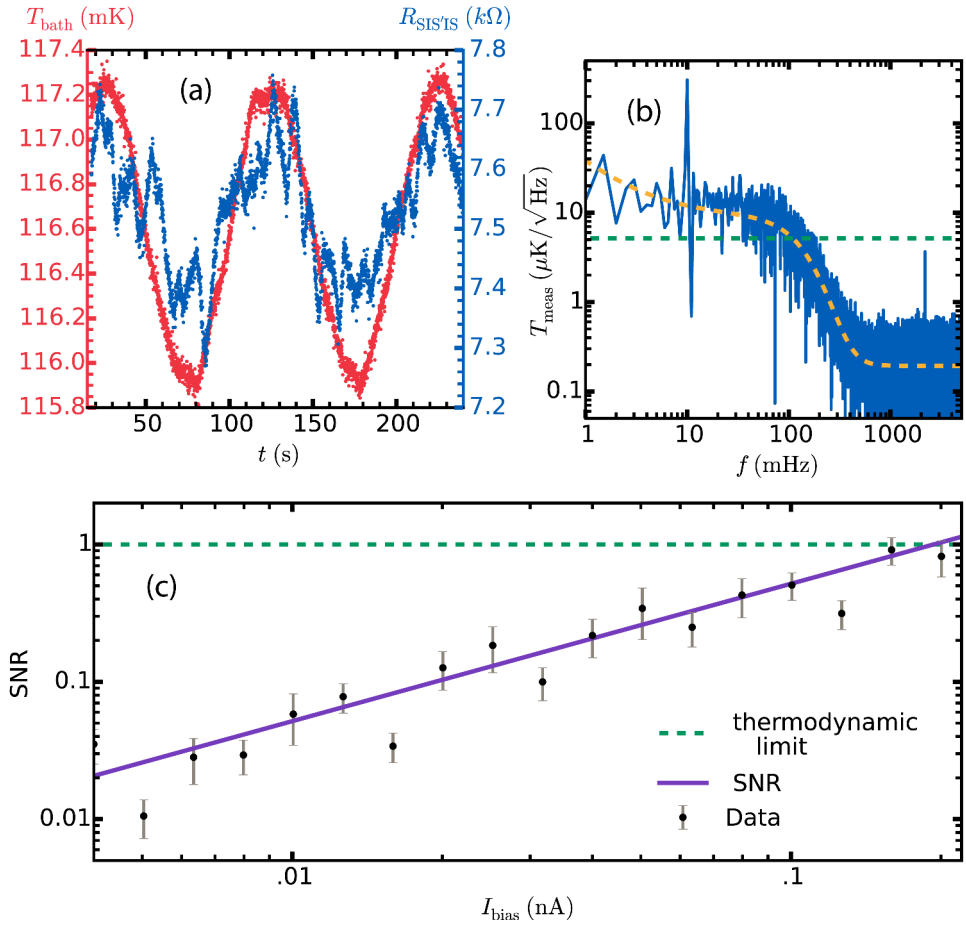

Figure 5.7. Extraction of the SNR from real time signals. (a) Time domain signals. In red the calibrated RuOx thermometer and in blue the zero bias slopes of the SIS'IS device ($R_{\mathrm{SIS'IS}}$), at an amplitude of the bias current of 200 pA . (b) The same signals after FFT. The yellow dashed line represents the model described by Eq. (4.2). The green dashed line is the expected temperature fluctuation limit. (c) SNR. The measured SNR, extracted from (b) is plotted for few bias currents (i.e. the amplitude of the sine wave) as black dots. The violet solid line is the SNR given by Eq. (5.5), with $\sqrt{S_{\mathrm{T}}(0)} = 5.5\ \mu\mathrm{K}/\sqrt{\mathrm{Hz}}$, $\partial R_0/\partial T = 0.65\ \mathrm{M\Omega/K}$. The extracted amplifier noise is $n_{\mathrm{f}} \sim 0.1\ \mathrm{nV}/\sqrt{\mathrm{Hz}}$. Here again the green dashed line represents the thermodynamic limit with SNR = 1. The error bars are depicting the scattering of the FFT around the 10 mHz drive, introducing some uncertainty in the measurement of the NET.

the temperature $T_{\mathrm{C_{S'}}}$. We also accounted for the fact that the bias current is intrinsically limited to values smaller than I_{C}. The product $I_{\mathrm{C}}R_{\mathrm{T}}$ appears in the numerator. This quantity can be replaced by its epression valid near T_{C}: $I_{\mathrm{C}}(T)R_{\mathrm{T}} \approx \Delta_{\mathrm{S}}/e\sqrt{1-T/T_{\mathrm{C_{S'}}}}$.

In order to increase the SNR, the first possibility is to decrease the amplifier noise n_{f}, changing the amplifier itself or using the cross-correlation of two amplifiers to reduce the noise floor [185, 186]. This approach is limited by the cross-talk of the line or the imperfection of even the best low noise amplifiers [187].

Another means to increase the SNR is to reduce the volume $\mathcal{V}$ of the metallic island. It is fairly easy to reach a volume as low as $1 \times 10^{-3}\ \mu\mathrm{m}^3$. The main trouble is the consequent reduction of the junction size which leads to Coulomb blockade. We experienced this trouble when the junction size is reduced below $\mathcal{A} \approx 100 \times 100\ \mathrm{nm}^2$, which corresponds to a volume $\mathcal{V} \sim 2 \times 10^{-3}\ \mu\mathrm{m}^3$. Thus one can expect at most an improvement by a factor 50 of the SNR by reducing the volume of the island. We present the SNR for a SIS'IS sample where the volume has been decreased to $\mathcal{V} \sim 3 \times 10^{-2}\ \mu\mathrm{m}^3$ in Fig. 5.7. In this particular geometry, the junction area is maximized to decrease as much as possible the charging energy ($\mathcal{A} \approx 1200 \times 230\ \mathrm{nm}^2$). The SNR is plotted against the amplitude of the bias current [Fig. 5.7 (c)], for a fixed bath temperature $T_{\mathrm{bath}} \approx 120$ mK. The bias current is limited by the measured switching current $I_{\mathrm{s}} \approx 260$ pA at this temperature. The only free parameter in the fit is $n_{\mathrm{f}} = 0.1\,\mathrm{nV}/\sqrt{\mathrm{Hz}}$. This is the best SNR measured so far, thanks to the low working temperature and the small volume. The bandwidth of this measurement was limited to 100 Hz by the drive frequency set to 177 Hz. Ultimately, the bandwidth of the measurement of SIS' TES is limited to kHz range by the line impedance. Nevertheless, the fact that the zero bias resistance is covering the full range from R_{qp} down to zero is promising. Such a device might be included in a RF-readout setup without the need of an impedance matching circuit.

Few devices in literature have made use of low T_{C} superconducting titanium films to see their properties greatly enhanced [18]. Unfortunately, this method suffers from low reproducibility of the Ti films [188]. To tune the transition temperature, bulk superconductors have been substituted by bi-layers (Mo-Cu [189], Au-Ti [190], etc.) or alloys (Al-Mn [191]). Using SQUID arrays to multiplex different devices allows one to construct

a large number of pixels needed for constructing a detector [192]. Few of these devices are operating in the thermodynamic regime [46–50, 54] with a non-trivial thermal model. Our implementation of a SIS'-TES proved to be sensitive, and after some improvement, able to reach a SNR around unity, hence approaching the thermodynamic limit.

Our attempt to produce titanium-gold bilayers lead to devices with T_{C} in the range 100-300 mK, with large variation from sample to sample. In addition, strong disorder-enhanced Andreev current was observed, with I_{N}^{A} as high as 300 pA and $\gamma \approx 2 \times 10^{-3}$.

6. Summary and outlook

In conclusion, the detectors investigated in this thesis present preliminary steps in studies of temperature fluctuations to be performed. The figures of merit of these detectors can be summarized in a single plot (Fig. 6.1) picturing the achieved NET (filled symbols) together with the corresponding thermodynamic limit (open symbols). The few thermometer technologies studied are depicted with different symbols: stars for the RF-NIS, diamonds for SIS' thermometers, and circles for the thermometer based on Andreev current. The gray grid depicts the expected magnitude of zero frequency temperature fluctuations, for few different volumes. As seen in chapter 2.6, the zero frequency fluctuation amplitude $S_{\mathrm{T}}(0)$ is increasing with decreasing bath temperature.

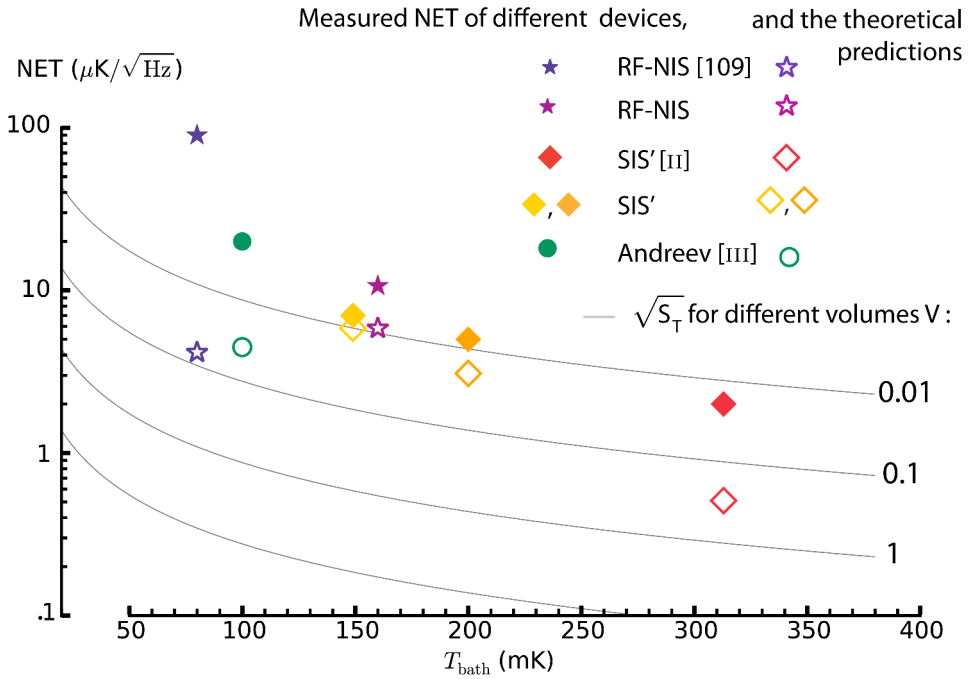

Figure 6.1. Comparison of the different thermometers studied in this thesis (full markers), and the theoretical limit set by the fluctuations of temperature at low frequency (open markers).

The ratio between the measured noise and the low frenquency limit of the temperature fluctuation spectrum $\sqrt{S_{\mathrm{T}}(0)}$ is defining the SNR. It has been decreased to reach a value around 2 in a SIS'-TES devices. Figure 6.1 is not a completely fair comparison though. Only the RF-NIS thermometers have a large enough bandwidth to measure the full temperature fluctuation spectrum. In order to merge constraints of senitivity and bandwidth, the RF readout of either SIS'-TES or an Andreev thermometer should be implemented. Furthermore, embedding these latter two detectors into a resonator (lumped or not) is made easier by the fact that no DC-bias is required.

The SIS'-TES bolometer optimization will require lower T_{C} of the superconducting film S'. Several options might be considered, like engineering a gold-titanium bilayer or using an aluminium-manganese alloy. The main difficulty of these approaches is to create a reproducible fabrication process providing good junction quality.

The Andreev thermometer is a promising tool for low temperature thermometry. On the existing samples, a study of the low temperature saturation would be interesting in order to demonstrate the reentrance effect [176, 193]. For this purpose, one has to limit the external heat load to less than 100 aW in the measurement setup. It would be interesting to see wheter the junction quality or the normal island is limiting the ratio $I_{\mathrm{N}}^{A}/I_{\mathrm{S}}^{A}$, as this should be large in order to use Andreev reflection for thermometry. This study would also give indications on the nature of the excess Andreev current I_{S}^{A} observed previously in other devices [194].

Bibliography

[1] T. Quinn, *Temperature* (Academic Press, 1983). (cit. on pp. v, 7, 9, 14)

[2] D. Twerenbold, *Rep. Prog. Phys.* **59**, 349 (1996). (cit. on p. 1)

[3] D. R. Artusa *et al.*, *Adv. High Energy Phys.* **2015**, 879871 (2015). (cit. on p. 1)

[4] B. Alpert *et al.*, *Eur. Phys. J. C* **75**, 112 (2015). (cit. on p. 1)

[5] C. Hollerith *et al.*, *Nucl. Instr. Meth. Phys. Res.* **520**, 606 (2004). (cit. on p. 1)

[6] M. D. Eisaman, J. Fan, A. Migdall, and S. V. Polyakov, *Rev. Sci. Ins.* **82**, 071101 (2011). (cit. on pp. 1–3)

[7] S. Mahieu, D. Maier, B. Lazareff, A. Navarrini, G. Celestin, J. Chalain, D. Geoffroy, F. Laslaz, and G. Perrin, *IEEE Trans. THz Sci. Technol.* **2**, 29 (2012). (cit. on p. 1)

[8] P. Pütz, C. E. Honingh, K. Jacobs, M. Justen, M. Schultz, and J. Stutzki, *A&A* **542**, L2 (2012). (cit. on p. 1)

[9] J. A. Brevik *et al.*, *Proc. SPIE* **7741**, 77411H (2010). (cit. on p. 1)

[10] T. de Graauw *et al.*, *A&A* **518**, L6 (2010). (cit. on p. 1)

[11] J.-M. Lamarre *et al.*, *A&A* **520**, A9 (2010). (cit. on p. 1)

[12] J. Zmuidzinas and P. Richards, *Proc. IEEE* **92**, 1597 (2004). (cit. on pp. 1, 15, 67, 69)

[13] P. Verhoeve, *J. Low Temp. Phys.* **151**, 675 (2008). (cit. on p. 1)

[14] N. E. Booth, B. Cabrera, and E. Fiorini, *Annu. Rev. Nucl. Part. Sci.* **46**, 471 (1996). (cit. on p. 1)

[15] C. Enss and D. McCammon, *J. Low Temp. Phys.* **151**, 5 (2008). (cit. on p. 1)

[16] A. Luukanen, A. Miller, and E. Grossman, *Proc. SPIE* **5789**, 127 (2005). (cit. on p. 1)

[17] K. D. Irwin, *Appl. Phys. Lett.* **66**, 1998 (1995). (cit. on pp. 2, 13)

[18] J. Wei, B. S. Karasik, S. V. Pereverzev, A. V. Sergeev, and M. S. Gershenson, *Nature Nano.* **8**, 496 (2008). (cit. on pp. 2, 74)

[19] K. Irwin, M. Niemack, J. Beyer, H. Cho, W. Doriese, G. Hilton, C. Reintsema, S. D.R., J. Ullom, and L. Vale, *Supercond. Sci. Tech.* **23**, 034004 (2010). (cit. on p. 2)

[20] F. Pajot *et al.*, *IEEE Trans. Appl. Supercond.* **21**, 192 (2011). (cit. on p. 2)

[21] G. N. Gol'tsman, O. Okunev, G. Chulkova, A. Lipatov, A. Semenov, K. Smirnov, B. Voronov, A. Dzardanov, C. Williams, and R. Sobolewski, *Appl. Phys. Lett.* **79**, 705 (2001). (cit. on p. 2)

[22] M. Nahum and J. M. Martinis, *Appl. Phys. Lett.* **63**, 3075 (1993). (cit. on pp. 2, 62)

[23] D. Golubev and L. Kuzmin, *J. Appl. Phys.* **89**, 6464 (2001). (cit. on pp. 2, 62)

[24] G. Brammertz, A. Peacock, P. Verhoeve, D. Martin, and R. Venn, *Nucl. Instr. and Meth. A* **520**, 508 (2004). (cit. on p. 3)

[25] R. J. Schoelkopf, S. H. Moseley, C. M. Stahle, P. Wahlgren, and P. Delsing, *IEEE Trans. Appl. Supercond.* **9**, 2935 (1999). (cit. on p. 3)

[26] Y. Hibi, H. Matsuo, S. Sekiguchi, H. Ikeda, and M. Fujiwara, *IEEE Trans. THz Sci. Technol.* **3**, 422 (2013). (cit. on p. 3)

[27] S. Ariyoshi, H. Matsuo, C. Otani, H. Sato, H. Shimizu, K. Kawase, and T. Noguchi, *IEEE Trans. Appl. Supercond.* **15**, 920 (2005). (cit. on p. 3)

[28] J. Zmuidzinas, presented at the Microwave Symposium (IMS), 2015 IEEE MTT-S International, p. 1, DOI: 10.1109/MWSYM.2015.7167149, http://doi.org/10.1109/MWSYM.2015.7167149. (cit. on p. 3)

[29] A. Semenov, G. N. Gol'tsman, and R. Sobolewski, *Superconductor Science and Technology* **15**, R1 (2002). (cit. on p. 3)

[30] B. Karasik, A. Sergeev, and D. Prober, *IEEE Trans. THz Sci. Technol.* **1**, 97 (2011). (cit. on pp. 3, 15, 16)

[31] B. S. Karasik, D. Olaya, J. Wei, S. Pereverzev, M. E. Gershenson, J. H. Kawamura, W. R. McGrath, and A. Sergeev, *IEEE Trans. Appl. Supercond.* **17**, 293 (2007). (cit. on p. 3)

[32] J. Yan, M.-H. Kim, J. A. Elle, A. B. Sushkov, G. S. Jenkins, H. M. Milchberg, M. S. Fuhrer, and H. D. Drew, *Nature Nano.* **7**, 472 (2012). (cit. on p. 3)

[33] Q. Han, T. Gao, R. Zhang, Y. Chen, J. Chen, G. Liu, Y. Zhang, Z. Liu, X. Wu, and D. Yu, *Sci. Rep.* **3**, 3533 (2013). (cit. on p. 3)

[34] D. Xu, D. E. Prober, H. Vora, and C. B. Mckitterick, *Graphene and 2D Materials* **1**, 1 (2014). (cit. on p. 3)

[35] B. A. Mazin, *AIP Conf. Proc.* **1185**, 135 (2009). (cit. on p. 3)

[36] P. Day, H. Leduc, B. Mazin, A. Vayonakis, and J. Zmuidzinas, *Nature* **425**, 817 (2003). (cit. on p. 3)

[37] J. Zmuidzinas, *Ann. Rev. Cond. Mat. Phys.* **3**, 169 (2012). (cit. on p. 3)

[38] S. Doyle, P. Mauskopf, J. Naylon, A. Porch, and C. Duncombe, *J.of Low Temp. Phys.* **151**, 530 (2008). (cit. on p. 3)

[39] J. Baselmans, S. Yates, R. Barends, Y. Lankwarden, J. Gao, H. Hoevers, and T. Klapwijk, *J. Low Temp. Phys.* **151**, 524 (2008). (cit. on p. 3)

[40] B. Mazin, K. O'Brien, S. McHugh, B. Bumble, D. Moore, S. Golwala, and J. Zmuidzinas, *Proc. SPIE* **7735**, 773518 (2010). (cit. on p. 3)

[41] P. Mauskopf *et al.*, *J. Low Temp. Phys.* **176**, 545, ISSN: 0022-2291 (2014). (cit. on p. 3)

[42] A. Fleischmann, C. Enss, and G. Seidel, in *Cryogenic Particle Detection* (Springer Berlin Heidelberg, 2005), vol. 99, p. 151. (cit. on p. 3)

[43] S. Bandler, K. Irwin, D. Kelly, P. Nagler, J.-P. Porst, H. Rotzinger, J. Sadleir, G. Seidel, S. Smith, and T. Stevenson, *J. Low Temp. Phys.* **167**, 254 (2012). (cit. on p. 3)

[44] C. Pies *et al.*, *J. Low Temp. Phys.* **167**, 269 (2012). (cit. on p. 4)

[45] J. Porst, S. R. Bandler, J. S. Adams, W. Hsieh, H. Rotzinger, G. M. Seidel, S. J. Smith, and T. R. Stevenson, *AIP Conf. Proc.* **1185**, 599 (2009). (cit. on p. 4)

[46] J. M. Gildemeister, A. T. Lee, and P. L. Richards, *Appl. Opt.* **40**, 6229 (2001). (cit. on pp. 4, 13, 16, 75)

[47] J. N. Ullom, J. A. Beall, W. B. Doriese, W. D. Duncan, L. Ferreira, G. C. Hilton, K. D. Irwin, C. D. Reintsema, and L. R. Vale, *Appl. Phys. Lett.* **87**, 194103 (2005). (cit. on pp. 4, 75)

[48] Y. Takei, L. Gottardi, H. Hoevers, P.A.J. de Korte, J. van der Kuur, M. Ridder, and M. Bruijn, *Journal of Low Temperature Physics* **151**, 161 (2008). (cit. on pp. 4, 75)

[49] M. Lindeman, P. Khosropanah, R. Hijmering, M. Ridder, L. Gottardi, M. Bruijn, J. van der Kuur, P.A.J. de Korte, J. Gao, and H. Hoevers, *J. Low Temp. Phys.* **167**, 96 (2012). (cit. on pp. 4, 16, 75)

[50] D. Goldie, A. Velichko, D. Glowacka, and S. Withington, *J. Low Temp. Phys.* **167**, 248 (2012). (cit. on pp. 4, 75)

[51] D. Rothfuß, A. Reiser, A. Fleischmann, and C. Enss, *Appl. Phys. Lett.* **103**, 052605 (2013). (cit. on p. 4)

[52] J. Beyer, D. Drung, A. Kirste, J. Engert, A. Netsch, A. Fleischmann, and C. Enss, *IEEE Trans. Appl. Supercond.* **17**, 760 (2007). (cit. on p. 4)

[53] K. Kinnunen, A. Nuottajärvi, J. Leppäniemi, and I. Maasilta, *J. Low Temp. Phys.* **151**, 119 (2008). (cit. on p. 4)

[54] M. Palosaari, K. Kinnunen, M. Ridder, J. van der Kuur, H. Hoevers, and I. Maasilta, *J. Low Temp. Phys.* **167**, 129 (2012). (cit. on pp. 4, 75)

[55] W. Middleton, *A history of the thermometer and its use in meteorology* (Johns Hopkins Press, 1966). (cit. on pp. 7, 14)

[56] S. Silbernagl and A. Despopoulos, *Color Atlas of Physiology* (Thieme, 2009). (cit. on p. 7)

[57] O. E. Dictionary, *Heat* (Oxford University Press, 2013). (cit. on p. 7)

[58] L. Landau and E. Lifshitz, *Statistical Physics* (Elsevier Science, 2013). (cit. on pp. 8, 10)

[59] N. Ashcroft and N. Mermin, *Physique des solides* (EDP Sciences, 2012). (cit. on pp. 10, 40, 41)

[60] M. Laakso, Doctoral Dissertation, Aalto University, School of Science, Apr. 2012. (cit. on p. 10)

[61] H. Pothier, S. Guéron, N. O. Birge, D. Esteve, and M. H. Devoret, *Phys. Rev. Lett.* **79**, 3490 (1997). (cit. on p. 10)

[62] F. Pierre and N. O. Birge, *Phys. Rev. Lett.* **89**, 206804 (2002). (cit. on p. 10)

[63] H. J. Schulz, *Fermi liquids and non-Fermi liquids*, ed. by E. A. Mesoscopic Quantum Physics Les Houches Session LXI. (cit. on p. 10)

[64] L. M. A. Pascal, A. Fay, C. B. Winkelmann, and H. Courtois, *Phys. Rev. B* **88**, 100502 (2013). (cit. on p. 11)

[65] R. Kubo, *Rep. Prog. Phys.* **29**, 255 (1966). (cit. on p. 12)

[66] T. T. Heikkilä and Y. V. Nazarov, *Phys. Rev. Lett.* **102**, 130605 (2009). (cit. on p. 12)

[67] C. Kittel, *Phys. Today* **41**, 93 (1988). (cit. on p. 13)

[68] B. Mandelbrot, *Phys. Today* **42**, 71 (1989). (cit. on p. 13)

[69] Planck Collaboration, *Astron. Astrophys.* **571**, A1 (2014). (cit. on p. 14)

[70] F. Pobell, *Matter and Methods at Low Temperatures* (Springer, 2007). (cit. on pp. 14, 41, 46, 47)

[71] H. Preston-Thomas, *Metrologia* **27**, 3 (1990). (cit. on p. 14)

[72] R. L. Rusby, M. Durieux, A. L. Reesink, R. P. Hudson, G. Schuster, M. Kühne, W. E. Fogle, R. J. Soulen, and E. D. Adams, *J. Low Temp. Phys.* **126**, 633 (2002). (cit. on p. 14)

[73] J. P. Pekola, K. P. Hirvi, J. P. Kauppinen, and M. A. Paalanen, *Phys. Rev. Lett.* **73**, 2903 (1994). (cit. on p. 14)

[74] J. P. Kauppinen, K. T. Loberg, A. J. Manninen, J. P. Pekola, and R. A. Voutilainen, *Rev. Sci. Ins.* **69**, 4166 (1998). (cit. on p. 14)

[75] H. Kraus, *Supercond. Sci. Technol.* **9**, 827 (1996). (cit. on p. 15)

[76] F. Sizov, *Opto-Electron. Rev.* **18**, 10 (2010). (cit. on p. 15)

[77] K. Irwin, G. Hilton, D. Wollman, and J. Martinis, *Appl. Phys. Lett.* **69**, 1945 (1996). (cit. on p. 15)

[78] B. Cabrera, *J. Low Temp. Phys.* **151**, 82 (2008). (cit. on p. 15)

[79] N. Downie, *Ink Sandwiches, Electric Worms, and 37 Other Experiments for Saturday Science* (Johns Hopkins University Press, 2003). (cit. on p. 16)

[80] S. P. Langley, *Proc. Am. Acad. Arts Sci.* **16**, 342 (1880-1881). (cit. on p. 16)

[81] S.-F. Lee, J. M. Gildemeister, W. Holmes, A. T. Lee, and P. L. Richards, *Appl. Opt.* **37**, 3391 (1998). (cit. on p. 15)

[82] J. C. Mather, *Appl. Opt.* **21**, 1125 (1982). (cit. on p. 16)

[83] D. J. Benford, *Transition edge sensor bolometers for CMB polarimetry*, ed. by w CMBPol technology whitepaper, 2008. (cit. on p. 16)

[84] G. E. Blonder, M. Tinkham, and T. M. Klapwijk, *Phys. Rev. B* **25**, 4515 (1982). (cit. on pp. 19, 20, 25)

[85] O. Saira, Doctoral Dissertation, Aalto University, School of Science, 2013. (cit. on pp. 20, 26)

[86] J. G. Simmons, *J. Appl. Phys.* **34**, 1793 (1963). (cit. on p. 20)

[87] W. F. Brinkman, R. C. Dynes, and J. M. Rowell, *Journal of Applied Physics* **41**, 1915 (1970). (cit. on p. 20)

[88] C. Kittel, *Introduction to Solid State Physics* (Wiley, 2004). (cit. on pp. 20–23)

[89] Y. V. Sharvin, *JETP Lett.* **21**, 655 [Zh. Eksp. Teor. Fiz. **48**, 984 (1965)] (1965). (cit. on p. 20)

[90] L. D. Bell and W. J. Kaiser, *Phys. Rev. Lett.* **61**, 2368 (1988). (cit. on p. 20)

[91] H. De Raedt, N. Garca, and J. J. Sáenz, *Phys. Rev. Lett.* **63**, 2260 (1989). (cit. on p. 20)

[92] T. Aref, A. Averin, S. van Dijken, A. Ferring, M. Koberidze, V. F. Maisi, H. Q. Nguyen, R. M. Nieminen, J. P. Pekola, and L. D. Yao, *J. Appl. Phys.* **116**, – (2014). (cit. on pp. 20, 26, 45, 60)

[93] R. Landauer, *IBM J. Res. Dev.* **1**, 223 (1957). (cit. on p. 21)

[94] Y. Nazarov and Y. Blanter, *Quantum Transport: Introduction to Nanoscience* (Cambridge University Press, 2009). (cit. on p. 21)

[95] A. Brinkman, A. A. Golubov, H. Rogalla, F. K. Wilhelm, and M. Y. Kupriyanov, *Phys. Rev. B* **68**, 224513 (2003). (cit. on p. 21)

[96] J. Voutilainen, T. T. Heikkilä, and N. B. Kopnin, *Phys. Rev. B* **72**, 054505 (2005). (cit. on p. 21)

[97] M. A. Laakso, P. Virtanen, F. Giazotto, and T. T. Heikkilä, *Phys. Rev. B* **75**, 094507 (2007). (cit. on p. 21)

[98] K. Flensberg, S. Girvin, M. Jonson, D. Penn, and M. Stiles, *Z. Phys. B Con. Mat.* **85**, 395–403, ISSN: 0722-3277 (1991). (cit. on p. 21)

[99] P. Joyez, D. Esteve, and M. H. Devoret, *Phys. Rev. Lett.* **80**, 1956 (1998). (cit. on p. 21)

[100] G.-L. Ingold and Y. Nazarov, in *Single Charge Tunneling*, ed. by H. Grabert and M. Devoret (Springer US, 1992), vol. 294, p. 21. (cit. on pp. 21, 25)

[101] R. de Bruyn Ouboter, *Sci. Am.* **276**, 98 (1997). (cit. on p. 21)

[102] F. London and H. London, *Proc. Roy. Soc. A (London)* **149**, 71 (1935). (cit. on p. 21)

[103] J. Bardeen, L. N. Cooper, and J. R. Schrieffer, *Phys. Rev.* **106**, 162 (1957). (cit. on p. 22)

[104] M. Tinkham, *Introduction to Superconductivity* (Dover Publications, Inc., 1996). (cit. on p. 22)

[105] P. Virtanen, *Private notes on NSN heat conduction*. (cit. on p. 22)

[106] N. Kopnin, *Lectures notes on the theory of superconductivity*, 2008. (cit. on p. 22)

[107] A. Andreev, *JETP Lett.* **19**, 1228 [Zh. Eksp. Teor. Fiz. **46**, 1823 (1964)] (1964). (cit. on p. 25)

[108] R. C. Dynes, V. Narayanamurti, and J. P. Garno, *Phys. Rev. Lett.* **41**, 1509 (1978). (cit. on p. 25)

[109] J. P. Pekola, V. F. Maisi, S. Kafanov, N. Chekurov, A. Kemppinen, Y. A. Pashkin, O. Saira, M. Möttönen, and J. S. Tsai, *Phys. Rev. Lett.* **105**, 026803 (2010). (cit. on p. 25)

[110] V. F. Maisi, O. Saira, Y. A. Pashkin, J. S. Tsai, D. V. Averin, and J. P. Pekola, *Phys. Rev. Lett.* **106**, 217003 (2011). (cit. on pp. 26, 60)

[111] K. Gloos, P. J. Koppinen, and J. P. Pekola, *J. Phys.: Condens. Matter* **15**, 1733 (2003). (cit. on p. 26)

[112] F. W. J. Hekking and Y. V. Nazarov, *Phys. Rev. Lett.* **71**, 1625 (1993). (cit. on p. 27)

[113] F. W. J. Hekking and Y. V. Nazarov, *Phys. Rev. B* **49**, 6847 (1994). (cit. on pp. 27, 29)

[114] H. Pothier, S. Guéron, D. Esteve, and M. H. Devoret, *Phys. Rev. Lett.* **73**, 2488 (1994). (cit. on pp. 27, 60)

[115] D. S. Golubev, M. S. Kalenkov, and A. D. Zaikin, *Phys. Rev. Lett.* **103**, 067006 (2009). (cit. on p. 27)

[116] H. Courtois, M. Meschke, J. T. Peltonen, and J. P. Pekola, *Phys. Rev. Lett.* **101**, 067002 (2008). (cit. on p. 27)

[117] B. Josephson, *Phys. Lett.* **1**, 251 (1962). (cit. on pp. 29, 30)

[118] R. E. Harris, *Phys. Rev. B* **10**, 84 (1974). (cit. on pp. 29, 32)

[119] J. Nicol, S. Shapiro, and P. H. Smith, *Phys. Rev. Lett.* **5**, 461 (1960). (cit. on p. 29)

[120] I. Giaever, *Phys. Rev. Lett.* **5**, 464 (1960). (cit. on p. 29)

[121] S. Tirelli, A. M. Savin, C. P. Garcia, J. P. Pekola, F. Beltram, and F. Giazotto, *Phys. Rev. Lett.* **101**, 077004 (2008). (cit. on pp. 29, 45, 66)

[122] F. Giazotto, T. T. Heikkilä, A. Luukanen, A. M. Savin, and J. P. Pekola, *Rev. Mod. Phys.* **78**, 217 (2006). (cit. on pp. 29, 36, 41, 57, 60)

[123] R. G. Melton, J. L. Paterson, and S. B. Kaplan, *Phys. Rev. B* **21**, 1858 (1980). (cit. on p. 29)

[124] A. J. Manninen, J. K. Suoknuuti, M. M. Leivo, and J. P. Pekola, *Appl. Phys. Lett.* **74**, 3020 (1999). (cit. on pp. 29, 67)

[125] M. Camarasa-Gómez, A. Di Marco, F. W. J. Hekking, C. B. Winkelmann, H. Courtois, and F. Giazotto, *Appl. Phys. Lett.* **104**, 192601 (2014). (cit. on p. 29)

[126] V. Ambegaokar and A. Baratoff, *Phys. Rev. Lett.* **10**, 486 (1963). (cit. on p. 30)

[127] V. Ambegaokar and A. Baratoff, *Phys. Rev. Lett.* **11**, 104 (1963). (cit. on p. 30)

[128] A. A. Golubov, M. Y. Kupriyanov, and E. Il'ichev, *Rev. Mod. Phys.* **76**, 411 (2004). (cit. on p. 30)

[129] D. E. McCumber, *J. Appl. Phys.* **39**, 3113 (1968). (cit. on p. 31)

[130] W. C. Stewart, *Appl. Phys. Lett.* **12**, 277 (1968). (cit. on p. 31)

[131] R. L. Kautz and J. M. Martinis, *Phys. Rev. B* **42**, 9903 (1990). (cit. on pp. 31, 32, 66)

[132] V. Ambegaokar and B. I. Halperin, *Phys. Rev. Lett.* **22**, 1364 (1969). (cit. on p. 31)

[133] W. A. Little, *Can. J. Phys.* **37**, 334 (1959). (cit. on p. 34)

[134] A. M. van den Brink and H. Dekker, *Phys. Rev. B* **51**, 17842. (cit. on p. 34)

[135] M. L. Roukes, M. R. Freeman, R. S. Germain, R. C. Richardson, and M. B. Ketchen, *Phys. Rev. Lett.* **55**, 422 (1985). (cit. on p. 35)

[136] F. C. Wellstood, C. Urbina, and J. Clarke, *Phys. Rev. B* **49**, 5942 (1994). (cit. on p. 35)

[137] V. F. Maisi, S. V. Lotkhov, A. Kemppinen, A. Heimes, J. T. Muhonen, and J. P. Pekola, *Phys. Rev. Lett.* **111**, 147001 (2013). (cit. on pp. 35, 47)

[138] A. V. Timofeev, C. P. Garcia, N. B. Kopnin, A. M. Savin, M. Meschke, F. Giazotto, and J. P. Pekola, *Phys. Rev. Lett.* **102**, 017003 (2009). (cit. on p. 35)

[139] G. D. Guttman, B. Nathanson, E. Ben-Jacob, and D. J. Bergman, *Phys. Rev. B* **55**, 3849 (1997). (cit. on p. 36)

[140] E. Zhao, T. Löfwander, and J. A. Sauls, *Phys. Rev. Lett.* **91**, 077003 (2003). (cit. on p. 36)

[141] E. Zhao, T. Löfwander, and J. A. Sauls, *Phys. Rev. B* **69**, 134503 (2004). (cit. on p. 36)

[142] J. B. Pendry, *J. Phys. A* **16**, 2161 (1983). (cit. on p. 38)

[143] D. R. Schmidt, R. J. Schoelkopf, and A. N. Cleland, *Phys. Rev. Lett.* **93**, 045901 (2004). (cit. on p. 38)

[144] M. Meschke, W. Guichard, and J. P. Pekola, *Nature* **444**, 187 (2006). (cit. on p. 39)

[145] J. Govenius, R. E. Lake, K. Y. Tan, V. Pietilä, J. K. Julin, I. J. Maasilta, P. Virtanen, and M. Möttönen, *Phys. Rev. B* **90**, 064505 (2014). (cit. on p. 39)

[146] A. V. Timofeev, M. Helle, M. Meschke, M. Möttönen, and J. P. Pekola, *Phys. Rev. Lett.* **102**, 200801 (2009). (cit. on p. 39)

[147] M. E. Gershenson, D. Gong, T. Sato, B. S. Karasik, and A. V. Sergeev, *Appl. Phys. Lett.* **79**, 2049 (2001). (cit. on p. 41)

[148] S. Wind, M. J. Rooks, V. Chandrasekhar, and D. E. Prober, *Phys. Rev. Lett.* **57**, 633 (1986). (cit. on p. 41)

[149] F. Pierre, A. B. Gougam, A. Anthore, H. Pothier, D. Esteve, and N. O. Birge, *Phys. Rev. B* **68**, 085413 (2003). (cit. on p. 41)

[150] P. Mohanty, E. M. Q. Jariwala, and R. A. Webb, *Phys. Rev. Lett.* **78**, 3366 (1997). (cit. on p. 41)

[151] G. J. Dolan, *Appl. Phys. Lett.* **31**, 337 (1977). (cit. on p. 43)

[152] J. Niemeyer and V. Kose, *Appl. Phys. Lett.* **29**, 380 (1976). (cit. on p. 43)

[153] Y. Nakamura, C. Chen, and J. Tsai, *Jpn. J. Appl. Phys.* **35**, L1465 (1996). (cit. on p. 44)

[154] *An Introduction to Electron Microscopy* (2015). (cit. on p. 46)

[155] F. J. Giessibl, *Rev. Mod. Phys.* **75**, 949 (2003). (cit. on p. 46)

[156] J. Pekola, *Dilution refrigerator equipment*, US Patent EP0828119 B1, 1998. (cit. on p. 47)

[157] S. Gasparinetti, K. L. Viisanen, O. Saira, T. Faivre, M. Arzeo, M. Meschke, and J. P. Pekola, *Phys. Rev. Appl.* **3**, 014007 (2015). (cit. on pp. 47, 62)

[158] K. L. Viisanen, S. Suomela, S. Gasparinetti, O. P. Saira, J. Ankerhold, and J. P. Pekola, *New J. Phys.* **17**, 055014 (2015). (cit. on pp. 47, 63)

[159] K. Bladh, D. Gunnarsson, E. Hürfeld, S. Devi, C. Kristoffersson, B. Smålander, S. Pehrson, T. Claeson, P. Delsing, and M. Taslakov, *Rev. Sci. Ins.* **74**, 1323 (2003). (cit. on p. 47)

[160] L. Spietz, J. Teufel, and R. Schoelkopf, *ArXiv:cond-mat/0601316* (2006). (cit. on p. 47)

[161] A. B. Zorin, *Rev. Sci. Ins.* **66**, 4296 (1995). (cit. on p. 48)

[162] O. Saira, A. Kemppinen, V. F. Maisi, and J. P. Pekola, *Phys. Rev. B* **85**, 012504 (2012). (cit. on pp. 48, 59, 61)

[163] P. Horowitz and W. Hill, *The Art of Electronics* (Cambridge University Press, 2006). (cit. on p. 54)

[164] S. K. Mitra and Y. Kuo, *Digital signal processing: a computer-based approach* (McGraw-Hill New York, 2006). (cit. on p. 54)

[165] C. Shannon, *Proc. IRE* **37**, 10 (1949). (cit. on p. 54)

[166] M. S. Babtlett, *Nature* **161**, 686 (1948). (cit. on p. 55)

[167] C. Enss, A. Fleischmann, K. Horst, J. Schönefeld, J. Sollner, J. Adams, Y. Huang, Y. Kim, and G. Seidel, *J. Low Temp. Phys.* **121**, 137 (2000). (cit. on p. 58)

[168] J. P. Pekola, O. Saira, V. F. Maisi, A. Kemppinen, M. Möttönen, Y. A. Pashkin, and D. V. Averin, *Rev. Mod. Phys.* **85**, 1421 (2013). (cit. on p. 59)

[169] G. O'Neil, P. Lowell, J. M. Underwood, and J. Ullom, *Phys. Rev. B* **85**, 134504 (2012). (cit. on p. 60)

[170] K. K. Likharev, *Rev. Mod. Phys.* **51**, 100 (1979). (cit. on p. 60)

[171] H. Nguyen, M. Meschke, H. Courtois, and J. Pekola, *Phys. Rev. Appl.* **2**, 054001 (2014). (cit. on p. 60)

[172] T. Greibe, M. P. V. Stenberg, C. M. Wilson, T. Bauch, V. S. Shumeiko, and P. Delsing, *Phys. Rev. Lett.* **106**, 097001 (2011). (cit. on p. 60)

[173] A. Feshchenko, L. Casparis, I. Khaymovich, D. Maradan, O. Saira, M. Palma, M. Meschke, J. Pekola, and D. Zumbühl, *ArXiv:1504.03841* (2015). (cit. on p. 62)

[174] D. R. Schmidt, C. S. Yung, and A. N. Cleland, *Appl. Phys. Lett.* **83**, 1002 (2003). (cit. on p. 62)

[175] K. Viisanen and O. Saira, *private communication* (2015). (cit. on p. 62)

[176] Y. Tanaka, A. A. Golubov, and S. Kashiwaya, *Phys. Rev. B* **68**, 054513 (2003). (cit. on pp. 63, 78)

[177] H. Courtois, P. Charlat, P. Gandit, D. Mailly, and B. Pannetier, *J. Low Temp.Phys.* **116**, 187 (1999). (cit. on p. 63)

[178] J. Kivioja, Doctoral Dissertation, Helsinki University of Technology, 2005. (cit. on p. 66)

[179] J. M. Martinis and R. L. Kautz, *Phys. Rev. Lett.* **63**, 1507 (1989). (cit. on p. 66)

[180] A. Steinbach, P. Joyez, A. Cottet, D. Esteve, M. H. Devoret, M. E. Huber, and J. M. Martinis, *Phys. Rev. Lett.* **87**, 137003 (2001). (cit. on p. 68)

[181] F. Giazotto, J. T. Peltonen, M. Meschke, and J. P. Pekola, *Nature Phys.* **6**, 254 (2010). (cit. on p. 69)

[182] M. Meschke, J. T. Peltonen, J. P. Pekola, and F. Giazotto, *Phys. Rev. B* **84**, 214514 (2011). (cit. on p. 69)

[183] R. N. Jabdaraghi, M. Meschke, and J. P. Pekola, *Appl. Phys. Lett.* **104**, 082601 (2014). (cit. on p. 69)

[184] A. Ronzani, C. Altimiras, and F. Giazotto, *Phys. Rev. Appl.* **2**, 024005 (2014). (cit. on p. 69)

[185] A. Van der Ziel, *Noise; sources, characterization, measurement* (Prentice-Hall, 1970). (cit. on p. 74)

[186] H. Klein, G. Klempt, and L. Storm, *Metrologia* **15**, 143 (1979). (cit. on p. 74)

[187] D. R. White and E. Zimmermann, *Metrologia* **37**, 11 (2000). (cit. on p. 74)

[188] J. Wei, Doctoral dissertation, New Brunswick Rutgers, 2007. (cit. on p. 74)

[189] B. L. Zink *et al.*, *Appl. Phys. Lett.* **89**, 124101 (2006). (cit. on p. 74)

[190] A. Luukanen, H. Sipilä, K. Kinnunen, A. Nuottajärvi, and J. P. Pekola, *Physica B* **284-288**, 2133 (2000). (cit. on p. 74)

[191] S. W. Deiker, W. Doriese, G. C. Hilton, K. D. Irwin, W. H. Rippard, J. N. Ullom, L. R. Vale, S. T. Ruggiero, A. Williams, and B. A. Young, *Appl. Phys. Lett.* **85**, 2137 (2004). (cit. on p. 74)

[192] W. B. Doriese *et al.*, *Appl. Phys. Lett.* **90**, 193508 (2007). (cit. on p. 75)

[193] D. Quirion, C. Hoffmann, F. Lefloch, and M. Sanquer, *Phys. Rev. B* **65**, 100508 (2002). (cit. on p. 78)

[194] V. F. Maisi, Doctoral Dissertation, Aalto University, School of Science, 2014. (cit. on p. 78)

Aalto-DD 169/2015

ISBN 978-952-60-6452-9 (printed)
ISBN 978-952-60-6453-6 (pdf)
ISSN-L 1799-4934
ISSN 1799-4934 (printed)
ISSN 1799-4942 (pdf)

Aalto University
School of Science
Low Temperature Laboratory
www.aalto.fi

BUSINESS + ECONOMY

ART + DESIGN + ARCHITECTURE

SCIENCE + TECHNOLOGY

CROSSOVER

DOCTORAL DISSERTATIONS